UNITED NATIONS EDUCATIONAL, SCIENTIFIC AND CULTURAL ORGANIZATION
INTERNATIONAL CENTRE FOR THEORETICAL PHYSICS
I.C.T.P., P.O. BOX 586, 34100 TRIESTE, ITALY, CABLE: CENTRATOM TRIESTE

SMR.703 - 13

WORKING PARTY ON
MECHANICAL PROPERTIES OF INTERFACES

23 AUGUST - 3 SEPTEMBER 1993

"Interfaces: Structure and Properties" (Part I)

"Atomic-Level Geometry of Crystalline Interfaces"

Dieter WOLF
Materials Science Division
Argonne National Laboratory
9700 S. Cass. Avenue
Building 233
Argonne, IL 60439
U.S.A.

These are preliminary lecture notes, intended only for distribution to participants.

CHAPTER ONE

Atomic-level geometry of crystalline interfaces

D. Wolf

Introduction · Basic terminology · Microstructure · Coherency, epitaxy and topotaxy · Commensurability · Degrees of freedom of crystalline interfaces · Atomic-level geometry of planar stacking · Grain boundaries · Characterization of the atomic structure of interfaces

1.1 INTRODUCTION

Any attempt to systematically investigate physical properties of solid interfaces, structure–property correlations in particular, should from the outset be based on a thorough understanding of their basic geometry. Moreover, a prerequisite for the atomic-level investigation of solid interfaces is a description of their basic structure and geometry not only in macroscopic terms but also at the atomic level.

The terms 'geometry' and 'structure' are often used interchangeably. However, when referring to the **geometry** of an interface, one usually thinks of the more **macroscopic** and purely crystallographic aspects of the structure, while by the **structure** one usually implies the **atomic** or **electronic** structure, including the chemical composition locally at the interface. The distinctions between, for example, coherent and incoherent interfaces, commensurate and incommensurate systems, homophase and heterophase interfaces, between 'special' and 'vicinal' surfaces, and between low-angle and high-angle (tilt or twist, symmetrical or asymmetrical, 'special' or general, twinned or non-twinned, coherent or incoherent) grain boundaries add to the terminology used to describe the geometry, structure, and chemistry of solid interfaces. This introductory chapter represents an attempt to clarify (or at least to collect) some of the terminology used in this diverse area of materials research and to formulate a unified atomic-level geometrical description applicable to all crystalline interfaces, including internal (homophase or heterophase) interfaces and external surfaces (i.e. solid-vacuum interfaces). It is our hope that such an undertaking will facilitate and clarify the communication among the different groups of the materials research community, broadly known as the interface community.

By close analogy to the distinction between crystallography and physics, throughout this chapter a sharp distinction will be made between the 'geometry' and the 'structure' of an interface. The latter term will therefore be reserved for the atomic and/or electronic structure (including the local distribution of chemical species), which includes the fully relaxed positions of all the atoms in the system and contains all the detailed information on phenomena such as reconstruction, misfit localization or delocalization, elastic strains and interfacial dislocations, impurity segregation, interface reactions, etc. at the interface. In common to all these phenomena is their origin in the **physics** of the system (by contrast with its crystallography), as prescribed by the nature of the electronic and atomic bonding near the interface.

In our discussion of the 'geometry' of crystalline interfaces, the macroscopic crystallographic aspects will be distinguished from the atomic-level charac-

terization of the basic interface geometry. The macroscopic geometry, to be discussed in section 1.6, includes all aspects of the geometry and crystallography determined by (i) the crystal structure(s) forming the interface and (ii) the degrees of freedom (DOFs) of the interfacial system, including the five macroscopic and three translational (or 'microscopic') degrees of freedom (sections 1.6.1 and 1.6.2). Taking the geometrical characterization further, down to the level of the atoms (albeit in their unrelaxed positions), naturally leads to the concept of the **atomic-level geometry** (section 1.7). Based on **unrelaxed** atom positions, i.e. strictly crystallographic concepts, this description provides information on the plane-by-plane arrangement of the atoms near the unrelaxed interface, most importantly on the size and shape of the planar unit cell (if the atomic structure is, indeed, periodic).

To illustrate these concepts by a simple example, we briefly consider a stacking fault (for details see sections 1.6.3 and 1.7.3). As illustrated in Figs. 1.1(a) and (b), the **macroscopic geometry** of a stacking fault is fully characterized by the two macroscopic DOFs associated with the fault (x–y) plane (here characterized in terms of Miller indices, $\langle hkl \rangle$, associated with the interface-plane normal) and the two translational DOFs in the translation vector, $\boldsymbol{T} = (T_x, T_y)$, which characterizes the stacking discontinuity in the fault plane. Based on this information, it is apparent that the interface may be generated by first choosing a particular crystallographic plane in a perfect crystal (Fig. 1.1(a)) and subsequently translating one half of that crystal relative to the other half, parallel to the intended fault plane by the vector $\boldsymbol{T}$ (Fig. 1.1(b)). Generation of its **atomic-level geometry**, illustrated in Figs. 1.1(c) and (d), provides information on the unrelaxed atom arrangement in the defect, including information on (i) the size and shape of its planar unit cell (which are obviously identical to those of the perfect crystal in Fig. 1.1(c)), (ii) the spacing of atom planes, $d(hkl)$, parallel to the fault plane, and (iii) the number of lattice planes in the repeat stacking sequence, $P(hkl)$, in the direction of the fault normal. In some cases this strictly geometrical atomic-level information on the defect may be very useful in predicting some of its basic physical properties, but without a knowledge of the detailed (i.e. relaxed) atomic structure of the interface and its chemical composition, both of which are governed by the electronic-structure-based physics of the interactions between the atoms.

Because of the complexity of the basic geometry of grain boundaries (GBs), involving both macroscopic concepts (such as the distinction between tilt, twist and general boundaries, and between low- and high-angle, symmetrical and asymmetrical boundaries, to name only a few) and atomic-level concepts (based on the geometry of Bravais lattices), a consistent atomic-level characterization of their basic geometry is particularly desirable and useful. In section 1.8 we will make an attempt to clarify the GB terminology by defining the atomic-level geometry of GBs within the framework, applicable to all interfacial systems, of the macroscopic and atomic-level concepts developed earlier in sections 1.6 and 1.7, respectively. Such a characterization of GBs, although not commonly used in the GB community, naturally exposes their close geometrical relationship to other planar defects and interface systems. In particular, the similarity between GBs and free surfaces has not been fully appreciated in the past, a fact which might be one of the reasons why only relatively little is known about the ideal-cleavage energy (or work of adhesion) of even the simplest GBs. Efforts based on the recognition of the considerable similarities in the atomic-level geometries of GBs and free surfaces therefore appear particularly promising to better elucidate the basic physics of interfacial decohesion.

The chapter is organized as follows. Section 1.2 contains a collection of terms and concepts, some macroscopic and some atomistic, the clarification of which at the outset might be helpful. The concepts of macroscopic and atomic-level geometry are developed and illustrated in sections 1.6 and 1.7, respectively. The goal of these two sections is to formulate a unified geometrical framework applicable to all types of interface systems. Then, in section 1.8, the geometry of GBs is reviewed within this general framework; a good understanding of sections 1.6 and 1.7 is therefore

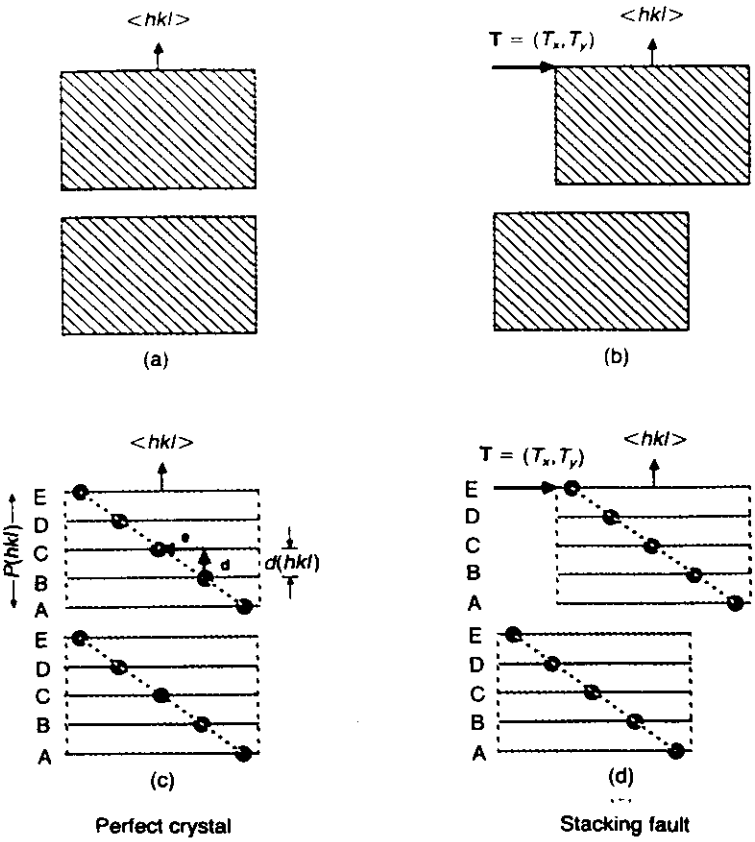

Fig. 1.1 'Macroscopic geometry' (top half) and 'atomic-level geometry' (bottom half) of a perfect crystal ((a) and (c)) and a stacking fault ((b) and (d)) on some crystal plane with normal $\langle hkl \rangle$. The concept of the stacking period, $P(hkl)$, the interplanar lattice spacing, $d(hkl)$, and the planar unit cell are discussed in detail in section 1.7.1.

required. It is our hope that this atomic-level view of the geometry of GBs, and the definition within this framework of much of the 'jargon' used to describe this geometry, will bring out the parallels that clearly exist with other types of crystalline interfaces. Finally, to emphasize and clarify the distinction between the **geometry** and **atomic structure** of solid interfaces, the chapter concludes with a brief review of the concepts and methods used to characterize the atomic structure of crystalline interfaces.

1.2 BASIC TERMINOLOGY

As discussed in the Editors' Introduction [1], three types of interfacial systems (labeled 'bulk', 'semi-bulk', and 'thin-film' interfaces) may be distinguished. This admittedly somewhat arbitrary classification is based on the fundamentally different effects of interfacial stresses and strains in the three types. Within the framework of this or any other classification, a variety of terms is used to describe the microstructure of polycrystalline materials as well as the macroscopic and atomic-level geometries and the atomic structure of individual interfaces. Although a common terminology to describe all structural aspects of crystalline interfaces has not evolved to date, in the following we will collect and define some of the more commonly used interface vocabulary.

1.2.1 Three basic types of interfaces

Depending on whether an interface is embedded in bulk material on both sides, on only one side, or not at all, we distinguish three basic types of interfaces, namely 'bulk', 'semi-bulk' and 'thin-film'

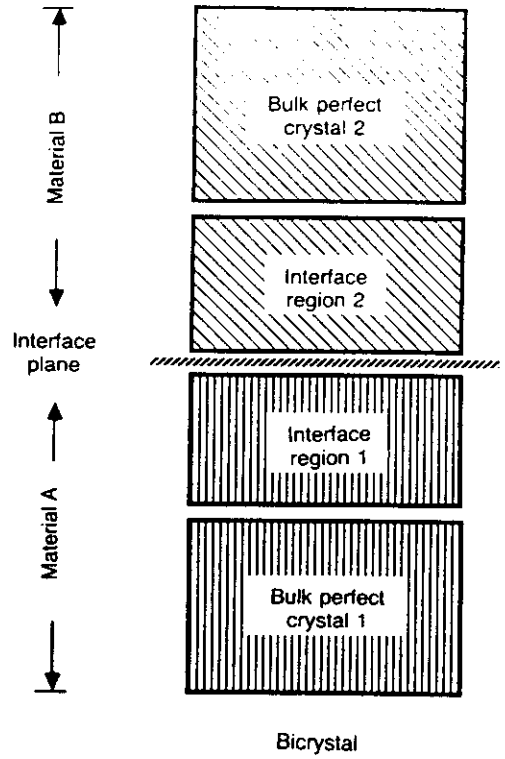

Fig. 1.2 Distinction of three types of interfacial systems. Depending on whether the system is embedded in bulk material on both sides of the interface, on only one side, or not at all, we distinguish 'bulk' (or 'buried' or 'internal'), 'semi-bulk', and 'thin-film' interfaces. A and B are generally different materials [1].

interfaces (Fig 1.2). This (highly idealized and somewhat subjective) distinction is based on the observation that (i) lattice-parameter changes in the interfacial region, induced by interfacial stresses, may have a pronounced effect on the physical properties and chemical composition at or near an interface and (ii) these stress-induced effects are fundamentally different in these three types of systems.

1.2.2 Bulk interfaces

The first type, a bulk interface (sometimes also called a **buried** or **internal** interface; see Fig. 1.1) represents the greatest experimental challenge because (i) an extremely small fraction of the atoms (typically about one in 10^{10}) actually experience the presence of the interface, and (ii) by contrast with a free surface, the disturbed atoms are sandwiched between (or buried in) bulk material. (For a review of the related experimental methods, see the following chapter in this volume [2].)

In the **bicrystal** shown in Fig. 1.2, the interface is conceptualized as being embedded between two well-oriented single crystals, and is hence characterized geometrically by five macroscopic and three translational ('microscopic') geometrical degrees of freedom (see section 1.6 below). Since crystallinity is only a necessary – but not a sufficient – condition for commensurability (section 1.4), a bicrystal may thus contain either a **commensurate** or an **incommensurate** interface in its center. If the two materials A and B forming the bicrystal are not the same (or at least represent different phases of the same material), the interface is usually referred to as an **interphase**, a **dissimilar-material** or a **bimaterial** interface, or as a **phase** or **heterophase** boundary, while the bicrystal contains a **grain boundary** (or **homophase** interface) or a **stacking fault** if A and B are identical materials and phases.

1.2.3 Semi-bulk interfaces

The second type, a semi-bulk interface (Fig. 1.3), is obtained by removing one of the two bulk semi-infinite crystals from Fig. 1.2. Containing both an external free surface and an internal interface, this type of interface may be viewed as consisting of a thin film of material B attached to a bulk substrate of material A. The term 'thin-film overlayer' therefore provides an alternate, equally descriptive characterization of this type of interface. A free surface is obviously included here as the case in which materials A and B are the same. According to Fig. 1.3, a 'bulk free surface' may be viewed conceptually as a homophase interface consisting of a strained (because of surface stresses) thin film which is attached to a bulk substrate.

We mention that the semi-bulk interface defined here is sometimes also referred to as an 'epitaxial' interface, or simply 'epitaxy'. As discussed further in section 1.4, this terminology arises from the manner in which a thin-film overlayer with a

Free surfac

Interface plane

Fig. 1.3 'Sen surface and a viewed as con film of mate material A. T from Fig. 1.2

mostly coh substrate i instances t 'epitaxial-g to some ci in the crys tained. To of a semi-l face consis rigid subst atomic-lev While the enable for 1.4), this and a poss thin-film

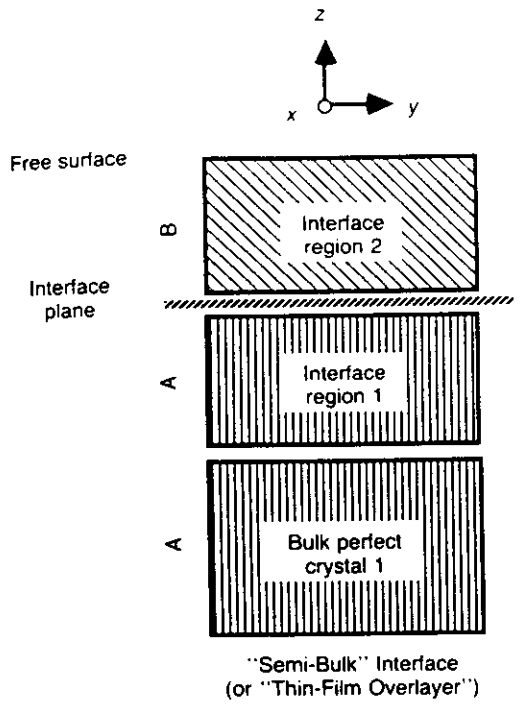

Fig. 1.3 'Semi-bulk' interface, containing both an external free surface and an internal interface. This type of interface may be viewed as consisting of a strained (because of surface stress) thin film of material B attached to a bulk (i.e. rigid) substrate of material A. This type of interface may conceptually be obtained from Fig. 1.2 by the removal of one of the two bulk regions.

mostly coherent epitaxial alignment relative to the substrate is usually produced. However, in many instances the interfaces ('epitaxy') obtained from 'epitaxial-growth' processes are coherent only up to some critical thickness, i.e. a 'perfect epitaxy' in the crystallographic sense [3] is not always obtained. To avoid confusion, in the above definition of a **semi-bulk** interface we mean simply an interface consisting of a thin film attached to a bulk, rigid substrate, thus avoiding any reference to the atomic-level quality of the thin-film overlayer. While the overlayer may stretch or contract to enable formation of a coherent interface (section 1.4), this definition includes incoherent interfaces and a possibly rotated (and even incommensurate) thin-film overlayer as well (section 1.5). Consequently, while the term semi-bulk interface will be used to emphasize its distinction from a bulk or thin-film interface, the atomic-level geometry and structure of such interfaces will be characterized in terms of the concepts of coherency (and the related concepts of epitaxy and topotaxy) and commensurability, discussed in detail in sections 1.4 and 1.5.

1.2.4 Thin-film interfaces

Finally the third type, a thin-film interface (Fig. 1.4), is obtained from Fig. 1.3 by replacing the bulk substrate by a thin film itself (i.e. by removing both bulk regions from Fig. 1.1), thus creating a second free surface and, hence, an unsupported, free-standing thin film (or a **thin slab**).

The two free surfaces in Fig. 1.4(a) may be eliminated conceptually by periodically extending the geometry in Fig. 1.4(a) in the z-direction, thus creating the thin-film superlattice sketched in Fig. 1.4(b) in which – ideally – all interfaces are identical. Such a material is also known as a **composition-modulated** or a **dissimilar-material** superlattice. If, in spite of a lattice-parameter mismatch, coherent interfaces can be sustained in the superlattice, it is also called a **strained-layer** superlattice.

If materials A and B are identical, the system in Fig. 1.4(a) degenerates into a thin slab with a grain boundary or stacking fault (or no interface at all) in its center, while the system in Fig. 1.4(b) becomes a superlattice of homophase interfaces (or a **grain-boundary superlattice** [7]). Although such superlattices have not actually been investigated experimentally, by the elimination of interfacial chemistry as a factor, they represent ideal model systems for investigating, by means of computer simulations, the strictly structural aspects of the physical properties of superlattice materials, against which any effects due to interface chemistry can be probed.

1.2.5 Effects of interfacial stresses

As already mentioned, the above distinction between bulk, semi-bulk and thin-film interfaces is

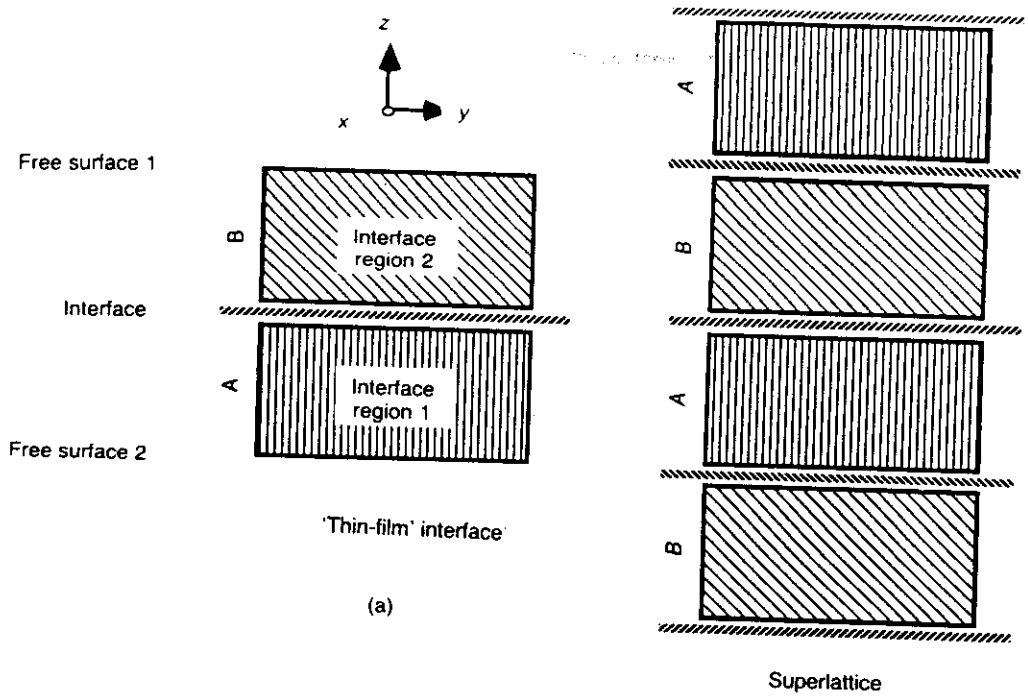

Fig. 1.4 'Thin-film' interface, generally consisting of two external and one internal surface (a). The geometry of this interface may be obtained from Fig. 1.3 by removing the remaining bulk region (Fig. 1.2). By periodically extending the geometry in (a) in the z direction, a 'thin-film superlattice' may be generated, thus replacing the external surfaces by internal interfaces. The latter may be coherent or incoherent, commensurate or incommensurate, homo- or heterophase interfaces. If all interfaces are coherent, the system is called a 'strained-layer' composition-modulated superlattice.

based on the observation that (i) lattice-parameter changes in the interfacial region, induced by interfacial stresses, may have a pronounced effect on the physical properties and chemical composition at or near an interface and (ii) these stress-induced effects are fundamentally different in these three types of systems.

It has been widely recognized in recent years that the surface-stress tensor, $\sigma_{\alpha\beta}$ ($\alpha, \beta = x, y, z$), may play an important role not only in surface reconstruction [4] but also, for example, in the elastic response of thin films [5, 8, 9] and thin-film superlattices [6, 7, 9]. To illustrate the concept of interfacial stress, here we briefly consider a free surface. $\sigma_{\alpha\beta}$ is then defined as the variation of the specific surface energy, γ, as a function of the strain, $\varepsilon_{\alpha\beta}$, i.e. $\sigma_{\alpha\beta} = \delta\gamma/\delta\varepsilon_{\alpha\beta}$. In a fully relaxed 'bulk' free surface (i.e. one attached to a bulk substrate; Fig. 1.3), $\sigma_{\alpha\beta}$ is usually diagonal, with a vanishing component, σ_{zz}, in the direction of the surface normal (z direction). Its only non-zero elements, σ_{xx} and σ_{yy}, are usually tensile and of significant magnitude, favoring contraction in the $(x-y)$ plane of the surface. However, in a bulk free surface this stress can only be relaxed by reconstruction; by contrast, a thin film may in addition contract, giving rise to a uniform reduction in the average lattice parameter(s) in the film plane, with a consequent Poisson expansion in the z direction (Fig. 1.5).

In the thin-film system sketched in Fig. 1.4(a), interfacial stresses arise not only from the two film surfaces but also from the interface between the films. By contrast, in the superlattice sketched in

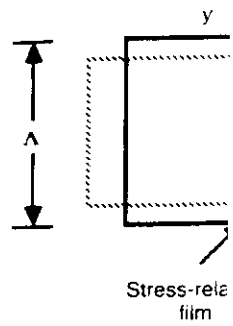

Fig. 1.5 Effect of the
average lattice paramet
slab') parallel and perp
contractions of the film
by a Poisson expansion
normal (z direction). N
in the bulk free surface

Fig. 1.3(b) all stre
of the interfaces b
entirely unconstra
the thin slab and
adjust their lattice
by the relaxing su
[7–9], hence crea
formation of a col
responding bulk la

To illustrate th
bulk interface (Fig
of the interface ar
interface is embec
lattice parameter(s
governed complet
bulk material. In
the atomic-level st
can therefore not
change in the a
the interface. By
this constraint re
and/or a redistri
segregation) as th
mechanisms.

The effects of

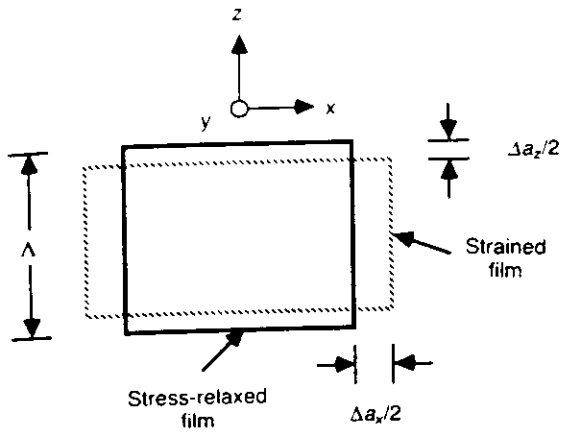

Fig. 1.5 Effect of the surface stresses, σ_{xx} and σ_{yy}, on the average lattice parameters of an unsupported thin film ('thin slab') parallel and perpendicular to the film plane. The in-plane contractions of the film, Δa_x and Δa_y (<0), are accompanied by a Poisson expansion, Δa_z (>0), in the direction of the film normal (z direction). Notice that σ_{zz} vanishes identically both in the bulk free surface and in the fully stress-relaxed film [8].

Fig. 1.3(b) all stresses originate from the presence of the interfaces between the two materials. Being entirely unconstrained by any bulk material, both the thin slab and the thin-film superlattice will adjust their lattice parameters to values governed by the relaxing surface and the interfacial stresses [7–9], hence creating favorable conditions for the formation of a coherent interface even if the corresponding bulk lattice parameters are mismatched.

To illustrate the role of interfacial stresses in a bulk interface (Fig. 1.2), we assume that both sides of the interface are indeed crystalline. Because the interface is embedded between bulk material, the lattice parameter(s) at or near the interface is (are) governed completely by that of the surrounding bulk material. Interfacial stresses associated with the atomic-level structural disorder at the interface can therefore not be relaxed, thus preventing any change in the average lattice parameter(s) near the interface. By contrast with a thin-film system, this constraint renders atomic-level reconstruction and/or a redistribution of chemical species (i.e. segregation) as the only possible stress-relaxation mechanisms.

The effects of interfacial stresses in the semi-bulk system sketched in Fig. 1.3 differ qualitatively from those of the thin-film and the bulk interface systems. Because the substrate consists of bulk material, its lattice parameter is undisturbed by the presence of the thin overlayer. However, the thin overlayer may, in principle, be strained relative to its 'intrinsic' lattice parameter when not attached to a substrate (i.e. relative to the lattice parameter of the surface-stress relaxed thin slab in Fig. 1.5). This straining of the film as it is attached to the substrate usually enables the film to be in more or less perfect registry ('coherency' or 'commensurability'; sections 1.4 and 1.5 below) with the substrate. It therefore appears that the physical properties of this type of interface should lie somewhere between those of a bulk interface and those of a thin film, the latter usually being strained, however.

1.3 MICROSTRUCTURE

The above classification, leading to the distinction between three basic types of interfaces, is highly idealized for two reasons. First, a 'real' material may contain a multitude and variety of interfaces; and second, in many instances the interfaces are not atomically flat but contain steps, ledges, dislocations and/or voids, and may be roughened, amorphous, etc. Hence, before discussing the atomic-level concepts of 'coherency' and 'commensurability', we briefly clarify several terms commonly used to describe the microstructure of 'real' interface materials.

By contrast with the bicrystal sketched in Fig. 1.2, a **polycrystal** contains many interfaces separated by crystallites of various orientations. For a 'large' grain size (typically of the order of microns or larger), one can expect the structure, chemistry, and properties of individual interfaces in the polycrystal to be similar to those of a bulk interface. In addition, however, the poorly understood **triple junctions** (i.e. line defects along which three interfaces meet) play an important role as well.

If the grain size is very small, typically of atomic or nanometer dimensions, the polycrystal

is referred to as a **nanocrystal** or a **nanophase** material. The interfaces may be either of a homophase or heterophase type; in the latter case the material is also called a **nanocomposite**.

The interfaces in these small-grained materials are not usually embedded between bulk material, thus permitting interfacial stresses to be relaxed. One would therefore expect their physical properties to be governed by both the presence of the interfaces and the deviation in their average lattice-parameter(s) from that of bulk material. Presumably their properties are therefore more similar to those of thin-film interface materials (section 1.2.4) than to those of bulk polycrystalline interface systems (section 1.2.2).

1.4 COHERENCY, EPITAXY AND TOPOTAXY

The epitaxial growth of one crystal on another is of considerable practical interest in the semiconductor industry which requires crystals free from dislocations and other defects. With the size of components in electronic devices rapidly approaching atomic-level dimensions, the need for atomic-level perfection of the crystals comprising such devices is ever increasing.

Central to the growth of nearly perfect epitaxial devices is the concept of a coherent (or dislocation-free) interface. Following Christian [10], a **coherent** interface between two crystals is defined as one for which corresponding atom planes and lines are continuous across the interface, i.e. one whose atomic structure is characterized by an atom-by-atom matching across the interface. Conversely, if there is no continuity of planes and lines across the interface, i.e. if a one-on-one atomic matching does not exist even locally, the interface is referred to as **incoherent**.

The terms epitaxial and coherent are sometimes used interchangeably to describe a planar defect with an atom-by-atom match across the interface. To illustrate the widespread confusion in the use of the term 'epitaxy', we here give two commonly used definitions. Webster's Dictionary, focusing on the growth process, defines epitaxy as 'the growth on a crystalline substrate of a crystalline substance that mimics the orientation of the substrate'. By contrast, the International Union of Crystallography [3] focuses on strictly crystallographic factors, by defining epitaxy as 'the phenomenon of mutual orientation of two crystals of different species, with two-dimensional lattice control (mesh in common)'. While Webster's definition clearly includes the usual distinction between homo- and hetero-epitaxy and between a thin-film overlayer and a bulk interface, the second definition is limited to hetero-interfaces with bulk material on both sides; it is hence much more restrictive than Webster's definition. Also, the purely crystallographic definition does not seem to require the continuity of lines in Christian's definition of 'coherency'. The concept of epitaxy is therefore less restrictive than the concept of coherency, as evidenced for example by the distinction between 'perfect epitaxy' (i.e. presumably coherent) and 'rotated epitaxy' (such as Au on Cr) in which a one-on-one correspondence of atoms across the interface may not exist. To avoid confusion, we will use the term 'epitaxy' when referring to the growth process, while the atomic structure at the interface will be characterized in terms of the concepts of coherency and commensurability (section 1.5).

(We also mention that the International Union of Crystallography has recommended avoidance of the term 'epitaxial' in favor of the terms 'epitaxic' or 'epitactic', with preference given to the term 'epitaxic' [3]. Webster's Dictionary, by contrast, finds the term 'epitaxial' perfectly in order; because of its wide and common use, throughout this chapter we will therefore use the latter.)

Another concept sometimes used in this context is that of **topotaxy**, which is defined as 'the phenomenon of mutual orientation of two crystals of different species resulting from a solid-state transformation or chemical reaction' [3]. This is in contrast with epitaxy, where we imply a layer-by-layer growth.

In both the coherent and the incoherent semi-bulk interfaces illustrated in Figs. 1.6(a) and (b), respectively, the lattice parameter of the substrate (open circles) is that of the bulk material, a_A. In the epitaxy shown in Fig. 1.6(a), the thin overlayer, of thickness Λ, is strained relative to its bulk lattice parameter, a_B, to match that of the substrate. In the incoherent case sketched in Fig. 1.6(b), by

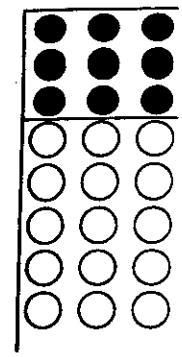

Cohe

(a

contrast, the l
more similar t
thin film.

To illustrat
topotaxy, exp
shown in Figs.
1.8 (courtesy
presents a hi
microscopy (T
epitaxial inter
thin film of T
Figure 1.8 sho
grown topotact
of internal oxic

Because of
herent interfac
for a relatively

$$f = (a_B - a_A$$

where A and B
overlayer, resp
achievable for
(involving, for
is obviously nc
geometry but
havior at the in

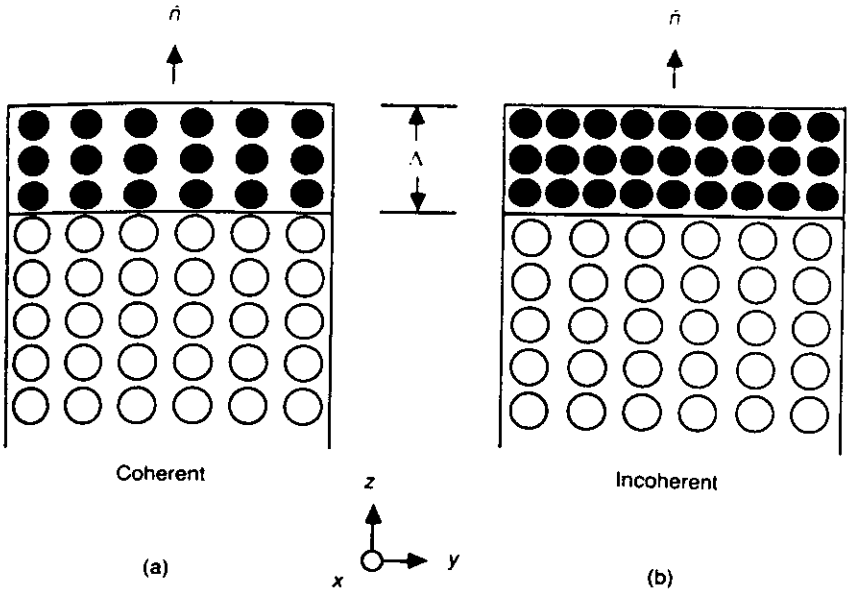

Fig. 1.6 (a) Coherent and (b) incoherent dissimilar-material interfaces, consisting of a thin-film overlayer attached to a bulk substrate. The coherent system represents an **epitaxy** in the crystallographic sense [3].

contrast, the lattice parameter of the overlayer is more similar to that of a fully relaxed, unstrained thin film.

To illustrate the concepts of epitaxy and topotaxy, experimental examples for both are shown in Figs. 1.7 (courtesy of K. L. Merkle) and 1.8 (courtesy of C. B. Carter). Figure 1.7 represents a high-resolution transmission-electron microscopy (TEM) image of a perfectly coherent epitaxial interface (dashed line) formed between a thin film of TiO_2 and an Al_2O_3 substrate [11]. Figure 1.8 shows a TEM image of spinel which has grown topotactically in an olivine matrix as a result of internal oxidation [12].

Because of the elastic energy involved, a coherent interface (i.e. 'epitaxy') can be formed only for a relatively small lattice-parameter mismatch,

$$f = (a_B - a_A)/a_A \tag{1.1}$$

where A and B denote the substrate and thin-film overlayer, respectively. The 'critical mismatch', f_c, achievable for particular combinations of materials (involving, for example, the fcc and bcc lattices) is obviously not only a function of the interfacial geometry but also of the local thermo-elastic behavior at the interface which, in turn, is a function

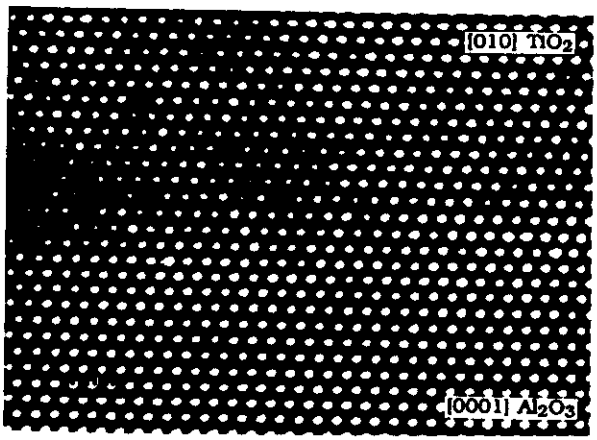

Fig. 1.7 High-resolution transmission-electron micrograph of a perfectly coherent epitaxial interface (dashed line) formed between a thin film of TiO_2 and an Al_2O_3 substrate. Notice the small change in the 'tilt' angle across the interface, resulting from a virtually sudden change at the interface of the lattice parameter in the direction of the interface normal [11] (Courtesy of K. L. Merkle).

of the film thickness, Λ. Also, the energy difference between the coherent and incoherent structures sketched in Fig. 1.6 depends critically on the relative strength of the interaction between atoms across the interface, as well as the modulus for

(a)

Fig. 1.8 (a) TEM image of spinel which has grown topotactically in an olivine matrix as a result of internal oxidation. The precipitate and the matrix are closely lattice-matched on one plane but the misfit is larger on the other – hence the elongated shape of the particles. (b) High-resolution image of one of the particles in (a). [12] (Courtesy of C. B. Carter).

shear locally at the interface [13, 14]. By contrast with strictly crystallographic geometrical concepts, the concept of coherency therefore also involves the elastic behavior of the material locally at the interface [14].

In practice, above a certain 'critical thickness', Λ_c, coherency cannot be sustained, and the interface becomes incoherent. The incoherent structure in Fig. 1.6(b) is therefore usually replaced by either of the **semi-coherent** types of structures sketched in Figs. 1.9 and 1.10 in which a strict one-to-one correspondence between atoms across the interface, as well as the continuity of lattice planes and lines, exists only locally in various regions along the interface. By contrast with **extraneous** (i.e. regular lattice) dislocations, the so-called **inherent** (or **misfit**) dislocations [15] in Figs. 1.9 and 1.10 at a critical distance, Λ_c, from the interface are an integral part of the long-range interface structure and, hence, its geometry and crystallography.

Depending on whether or not the inherent dislocations are long-range ordered, we distinguish in Figs. 1.9 and 1.10 the two types of semi-coherent interfaces, formed by **commensurate and incommensurate** crystal lattices, respectively (section 1.5 below). In most practical cases, if the materials or

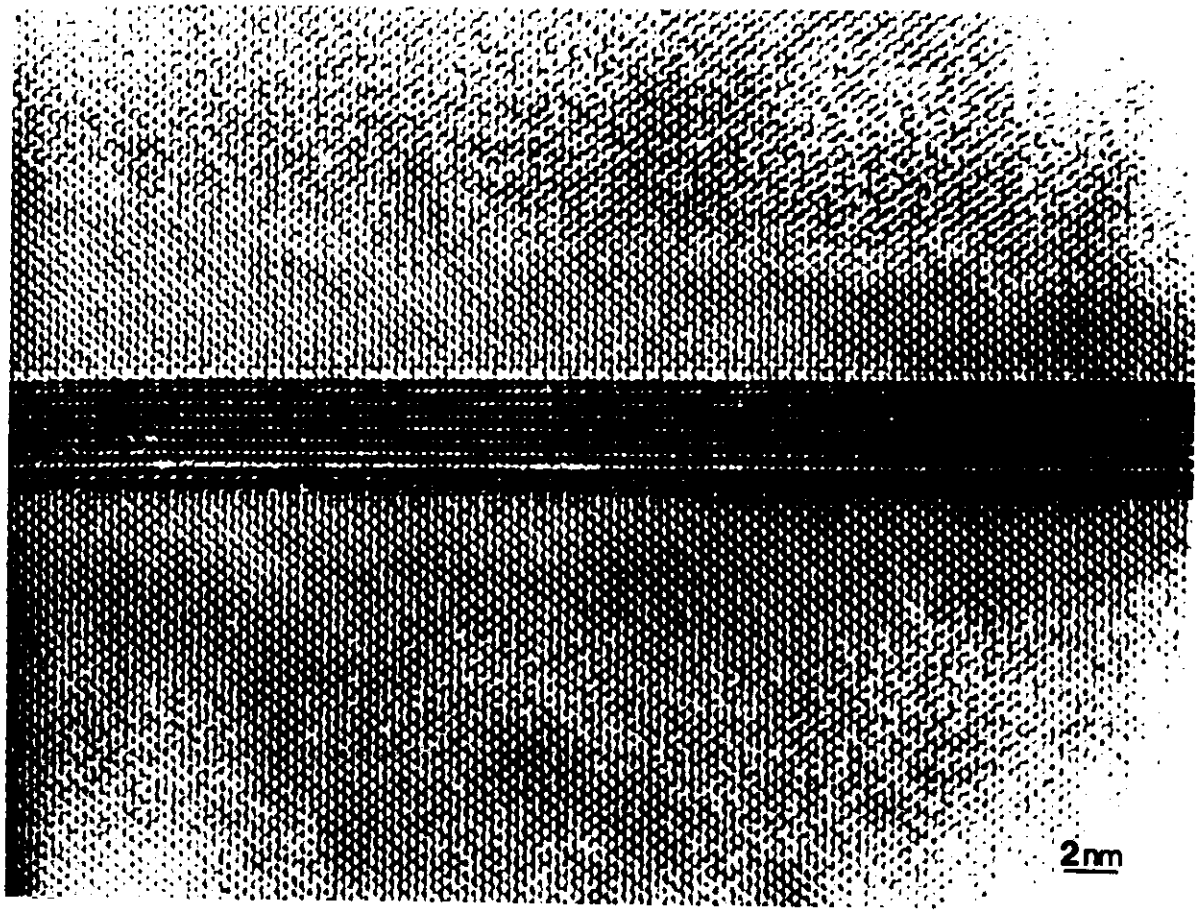

(b)

phases forming the interface are not the same, only the incommensurate structure in Fig. 1.10 exists, unless both the thin-film overlayer and the substrate can adjust their lattice parameters. While this is impossible for the bulk substrates sketched in Figs. 1.6, 1.9, and 1.10, in the thin-film superlattices shown in Fig. 1.11 both a_A and a_B are adjustable due to the effect of interfacial stresses. The **strained-layer** (i.e. coherent) superlattice shown in Fig. 1.11(a) can therefore be expected to exhibit a wider range of stability against becoming incoherent; therefore, in Fig. 1.11(b) we assume a larger critical mismatch and critical thickness than in the corresponding **semi-bulk** epitaxial system in Fig. 1.6(a).

While eq. (1.1) provides a useful measure of the mismatch for a bulk-substrate epitaxial system, it is not very meaningful for thin-film systems (in which neither constituent 'knows' its bulk lattice parameter). The mismatch is then better characterized in terms of the average lattice parameter, $\bar{a} = (a_B + a_A)/2$, by defining [14]

$$\bar{f} = (a_B - a_A)/\bar{a} \tag{1.2}$$

The definitions of the mismatch parameters in eqs. (1.1) and (1.2) for semi-bulk and thin-film interface systems, respectively, have proven useful in the determination of their critical mismatch and thickness, f_c and Λ_c, by means of continuum-elasticity theory [13, 14].

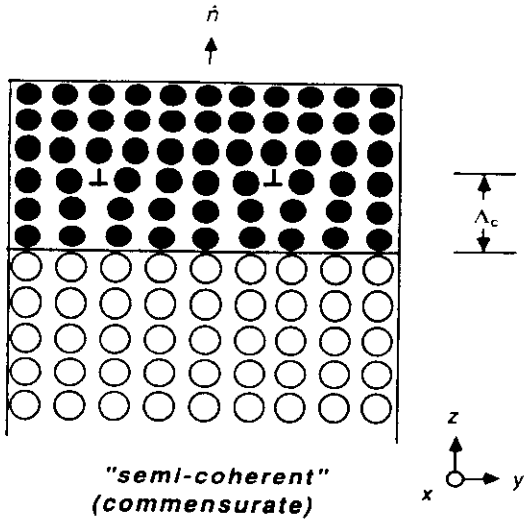

Fig. 1.9 'Semi-coherent' but commensurate (section 1.5) thin-film overlayer in which a strict one-to-one correspondence between atoms across the interface, as well as the continuity of lattice planes and lines, exists only locally in various regions along the interface.

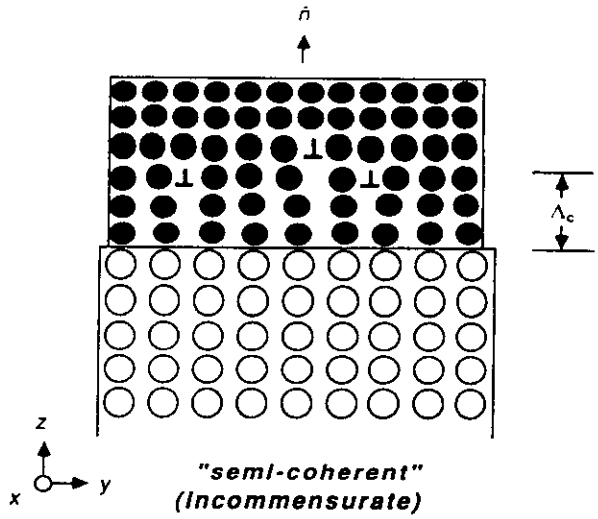

Fig. 1.10 'Semi-coherent' but incommensurate (section 1.5) thin-film overlayer. A planar periodic unit cell cannot be defined for such a system, as indicated by the mismatch between the lateral dimensions on the two sides of the interface.

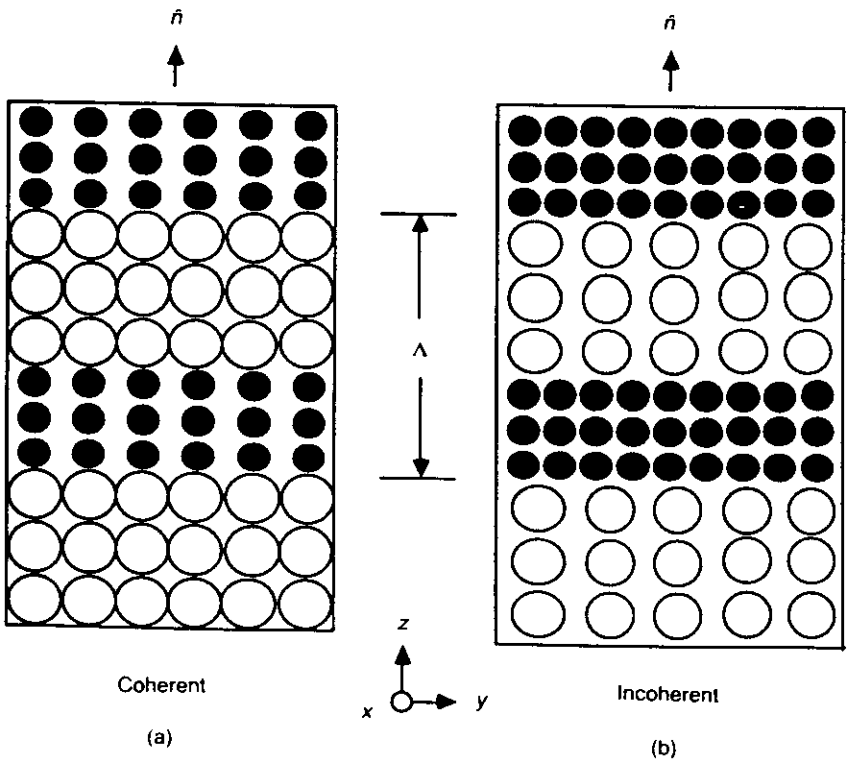

Fig. 1.11 (a) Coherent or 'strained-layer' and (b) incoherent thin-film superlattice. By contrast with the semi-bulk system in Fig. 1.6 (in which the substrate is a bulk material), in the thin-film system sketched here the lattice parameters parallel and perpendicular to the interfaces can adjust in response to interfacial stresses.

Commensu

1.5 COMME

In a commer
on both sid
ordered para
common pla
the periodic
if the atomic
is usually re
concept of c
crystalline lo
planes formin
a crystal and
therefore nev
hand, as evi
mensurate G
crystalline or
formation of

To formula
between two
Bravais lattice
b_2 (Fig. 1.12)
the planar ve
primitive unit
if it exists. As
formation of
primitive unit
combined witl
sight one is te
commensurabi

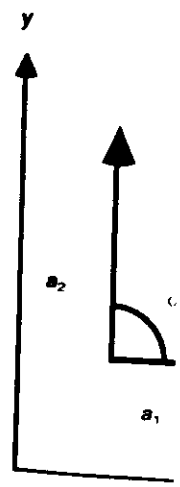

1.5 COMMENSURABILITY

In a **commensurate** interface the atomic positions on both sides of the interface are long-range ordered parallel to the plane of the defect, and a common planar unit cell exists which describes the periodic (i.e. crystalline) structure. Conversely, if the atomic structure is non-periodic, the interface is usually referred to as **incommensurate**. The concept of commensurability obviously requires crystalline long-range order in both sets of lattice planes forming the interface. An interface between a crystal and an amorphous material or a liquid can therefore never be commensurate. On the other hand, as evidenced by the existence of incommensurate GBs, the necessary requirement of crystalline order is not sufficient to guarantee the formation of a commensurate interface.

To formulate the criterion for commensurability between two lattice planes, we define two planar Bravais lattices by the Bravais vectors a_1, a_2 and b_1, b_2 (Fig. 1.12). The task then consists of finding the planar vectors, C_1 and C_2, which define the primitive unit cell of the common 2D superlattice – if it exists. As an example, Fig. 1.13 illustrates the formation of a planar superlattice in which four primitive unit cells of the first (a_1, a_2) plane are combined with nine of the other (b_1, b_2). At first sight one is tempted to require as the condition of commensurability that, in addition to the coordinate origin, there are infinitely many common points which satisfy the relation,

$$n_1 a_1 + n_2 a_2 = m_1 b_1 + m_2 b_2 \tag{1.3}$$

with n_1, n_2, m_1, $m_2 = 0, \pm 1, \pm 2$, etc. (In the example of Fig. 1.13, $n_1 = n_2 = 2$ and $m_1 = m_2 = 3$.) Equation (1.3) would rule out lattice planes with irrational unit-cell dimensions from being commensurate. Yet, as the example in Fig. 1.14 shows, two square planar lattices with a $\sqrt{2}$ ratio of the unit-cell dimensions are commensurate. As illustrated in the right half of the figure, however, in spite of the fact that eq. (1.3) cannot be satisfied, the two lattices are actually commensurate (albeit incoherent) if one allows for a 45° rotation about the common plane normal. The condition (1.3) is hence too restrictive, as it does not permit for the rotation of the two planes relative to one another about their common normal. As discussed in section 1.6.1 below, such a 'twist' rotation by some angle θ is a macroscopic geometrical degree of freedom of the interface and hence should be included in the criterion for commensurability. Equation (1.3) then becomes

$$n_1 a_{1x} + n_2 a_{2x} = (m_1 b_{1x} + m_2 b_{2x}) \sin\theta - (m_1 b_{1y} + m_2 b_{2y}) \cos\theta \tag{1.4a}$$

$$n_1 a_{1y} + n_2 a_{2y} = (m_1 b_{1x} + m_2 b_{2x}) \cos\theta + (m_1 b_{1y} + m_2 b_{2y}) \sin\theta \tag{1.4b}$$

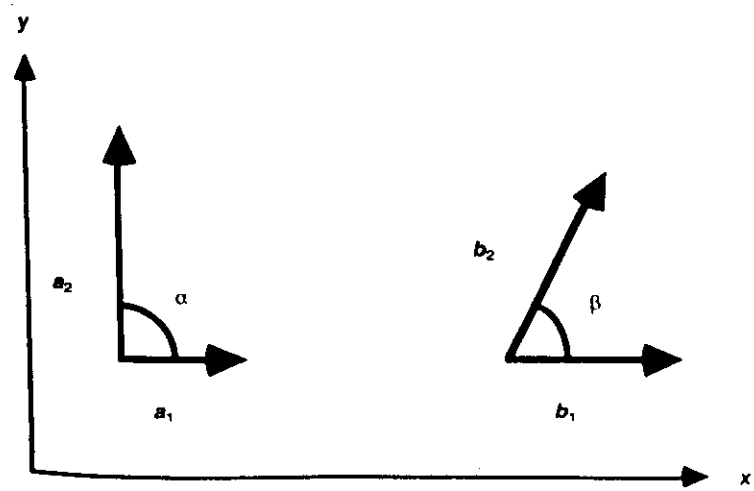

Fig. 1.12 Two sets of planar Bravais vectors a_1, a_2 and b_1, b_2.

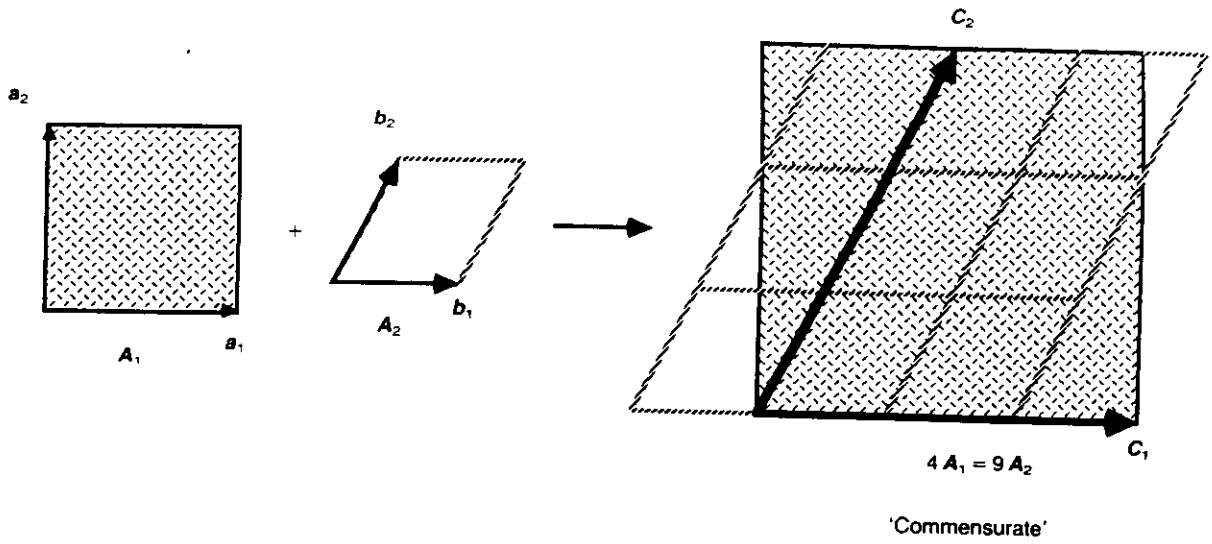

Fig. 1.13 Example illustrating the formation of a commensurate interface by combining four primitive unit cells of the first (a_1, a_2) crystal with nine of the other (b_1, b_2). A_1 and A_2 are the related planar unit-cell areas.

From eqs. (1.4a) and (b) it follows that

$$\tan\theta = \frac{(n_1a_{1x} + n_2a_{2x})(m_1b_{1x} + m_2b_{2x}) + (n_1a_{1y} + n_2a_{2y})(m_1b_{1y} + m_2b_{2y})}{(n_1a_{1y} + n_2a_{2y})(m_1b_{1x} + m_2b_{2x}) - (n_1a_{1x} + n_2a_{2x})(m_1b_{1y} + m_2b_{2y})} \quad (1.5)$$

For a given set of Bravais vectors a_1, a_2, and b_1, b_2, eq. (1.5) provides an infinite set of θ values associated with n_1, n_2, m_1, $m_2 = 0, \pm1, \pm2$, etc. This does not necessarily mean, however, that the two planes are commensurate since, for some allowed angle θ, eq. (1.5) merely describes a line of coincident points in common to the two planar Bravais lattices obtained when the two lattices are rotated relative to each-other. The first non-vanishing point on this line, given by the integers n_1^0, n_2^0, m_1^0 and m_2^0, defines one of the two primitive vectors, say C_1, of the superlattice (expressed here in the unrotated x–y coordinate system in Fig. 1.14):

$$C_1 = n_1^0a_1 + n_2^0a_2 \quad (1.6)$$

For the two planes to be commensurate, for the same angle θ a second vector,

$$C_2 = n_1^1a_1 + n_2^1a_2 \quad (1.7)$$

which is not collinear with C_1, must also exist. The condition of commensurability hence requires that, for the same value of θ, eq. (1.5) yields at least two vectors which satisfy the condition

$$|[C_1 \times C_2]| > 0 \quad (1.8)$$

As is well known, the vector product $[C_1 \times C_2]$ defines the area vector (parallel to the plane normal) of the plane of the common superlattice. Equation (1.8) hence expresses the requirement for the existence of a planar unit cell of the superlattice with a non-vanishing area.

We mention that C_1 and C_2 could have equally been expressed in the rotated x'–y' coordinate system in Fig. 1.14 as follows:

$$C_1' = m_1^0b_1' + m_2^0b_2' \quad (1.9)$$

$$C_2' = m_1^1b_1' + m_2^1b_2' \quad (1.10)$$

and the condition of commensurability becomes:

$$|[C_1' \times C_2']| > 0 \quad (1.11)$$

From the existence of a planar superlattice, it follows that the related primitive planar unit-cell areas, A_1 and A_2, of the underlying Bravais lattices are compatible with one another in that they are

rational multiples of each other, i.e.

$$nA_1 = mA_2 \tag{1.12}$$

where n and m are positive integers. Expressing the areas in terms of the basis vectors, this condition becomes:

$$n(a_{1x}a_{2y} - a_{1y}a_{2x}) = m(b_{1x}b_{2y} - b_{1y}b_{2x}) \tag{1.13}$$

Although the compatibility of the primitive planar unit-cell areas is clearly necessary for two lattice planes to be commensurate, in order to form a superlattice, the two lattice planes also have to share infinitely many common (albeit not necessarily all) lattice points, i.e. satisfy eq. (1.5). (If they share all lattice points, the interface is 'coherent'; section 1.4.)

To illustrate the above expressions with a simple example, we consider the two square lattices of Fig. 1.14, with the Bravais vectors:

$$\boldsymbol{a}_1 = (a, 0),\ \boldsymbol{a}_2 = (0, a);$$
$$\boldsymbol{b}_1 = (\sqrt{2}a, 0),\ \boldsymbol{b}_2 = (0, \sqrt{2}a) \tag{1.14}$$

Inserting eq. (1.14) into eqs. (1.4a) and (b) gives

$$n_1 a = m_1\sqrt{2}a \sin\theta - m_2\sqrt{2}a\cos\theta \tag{1.15a}$$

$$n_2 a = m_1\sqrt{2}a\cos\theta + m_2\sqrt{2}a\sin\theta \tag{1.15b}$$

and, according to eq. (1.5), the angle θ is given by

$$\tan\theta = (n_1m_1 + n_2m_2)/(n_2m_1 - n_1m_2) \tag{1.16}$$

As already discussed, for $n_1m_1 + n_2m_2 = 0$ ($\tan\theta = 0$, i.e. $\theta = 0°$) or $n_2m_1 - n_1m_2 = 0$ ($\tan\theta = \infty$, i.e. $\theta = 90°$), a superlattice does not exist and, as readily verified, the condition (1.8) can therefore not be satisfied. The smallest integers for which eq. (1.16) yields a value of $\tan\theta$ that differs from zero and infinity and which satisfy the condition (1.8) are, for example, $n_1^0 = 1$, $n_2^0 = 1$, $m_1^0 = 1$ and $m_2^0 = 0$, for which eq. (1.16) yields $\tan\theta = 1$, or $\theta = 45°$. According to eq. (1.6) the first vector of the superlattice, $\boldsymbol{C}_1$, expressed in the unrotated (x–y) coordinate system in Fig. 1.14, is hence given by

$$\boldsymbol{C}_1 = \boldsymbol{a}_1 + \boldsymbol{a}_2 \tag{1.17}$$

To determine $\boldsymbol{C}_2$, for the same value of θ a second superlattice point has to be extracted from eq. (1.16) which is not collinear with $\boldsymbol{C}_1$. One such point, also nearest to the origin, is obtained for example for $n_1^1 = 1$, $n_2^1 = -1$, $m_1^1 = 0$ and $m_2^1 = 1$; hence according to eq. (1.7),

$$\boldsymbol{C}_2 = \boldsymbol{a}_1 - \boldsymbol{a}_2 \tag{1.18}$$

$\boldsymbol{C}_1$ and $\boldsymbol{C}_2$ could have been equally determined in the rotated coordinate system, i.e. in terms of the rotated vectors $\boldsymbol{b}_1'$ and $\boldsymbol{b}_2'$. Inserting the values for m_1 and m_2 into eqs. (1.9) and (1.10), we find that (Fig. 1.14)

$$\boldsymbol{C}_1' = \boldsymbol{b}_1',\ \boldsymbol{C}_2' = \boldsymbol{b}_2' \tag{1.19}$$

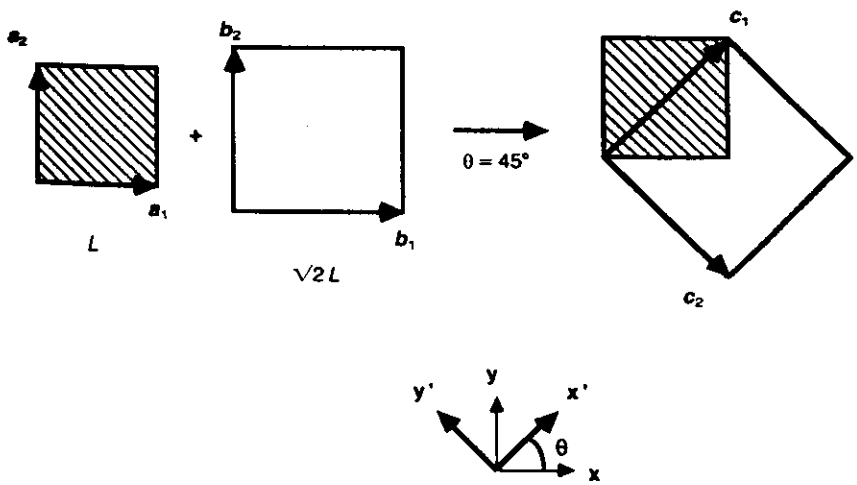

Fig. 1.14 Example illustrating that the formation of a commensurate interface may involve a rotation about the interface normal, in this case by an angle of 45°.

To summarize, two Bravais-lattice planes are commensurate if (a) under a general (twist) rotation, the two lattice planes share infinitely many common lattice points (eq. (1.4)), and (b) their primitive planar unit-cell areas are compatible (eq. (1.12)).

1.6 DEGREES OF FREEDOM OF CRYSTALLINE INTERFACES

The **macroscopic geometry** of interfaces to be discussed in this section includes all aspects of the geometry and crystallography determined by (i) the crystal structure(s) forming the interface and (ii) the degrees of freedom (DOFs) of the interfacial system, including the five macroscopic and the three translational (or 'microscopic') degrees of freedom.

The macroscopic geometrical description of crystalline interfaces has been an area of considerable activity during the past 30 years. Much of this work, particularly in the grain-boundary area, has focused on the formal description, in terms of linear algebra, of the misorientation relationship between the two crystal lattices forming the interface. The description of GB structures in terms of the coincident-site lattice (CSL), the displacement-shift-complete (DSC) lattice, and the 0-lattice are the main outcome of this work [16–19]. Within this framework the **macroscopic** DOFs are defined either within what we call the **CSL-misorientation scheme** or in terms of the **tilt-inclination scheme**; the underlying concepts will be discussed in detail in sections 1.8.1. and 1.8.2.

In common to these two methods for defining the macroscopic DOFs is their focus on how, hypothetically, a particular 2d interface structure can be generated by a single CSL rotation of two interpenetrating 3d crystal lattices. Considering the fact that solid interfaces are **planar** defects, this focus on a **three**-dimensional superlattice in common to the two crystals forming the interface appears somewhat surprising. Apart from the obvious limitation of such a description to **commensurate** interfaces, intuitively one would expect that the physically relevant geometrical features of **crystalline** interfaces are related to (i) the crystallographic orientation of the interface **plane** and (ii) the size and/or shape of the **planar unit cell** (if the interface is commensurate).

Here we will therefore adopt a more widely applicable definition of the macroscopic degrees of freedom of solid interfaces [20], referred to as the **interface-plane scheme** [21], which is applicable to all types of crystalline (homophase and heterophase) interfaces, commensurate or incommensurate, and which enables a direct comparison of the geometry of all three basic types of interfaces from a common point of view. While the underlying terminology, to be developed in section 1.6.1, is rather commonly applied to semi-bulk and thin-film (coherent or incoherent) dissimilar-material interfaces, in the GB area it is not widely used; instead, the geometry of GBs is usually described in terms of the CSL-based terminology. As an example, the three simplest interface systems (from the point of view of their underlying number of DOFs) will be discussed in section 1.6.3. Later, in section 1.8, we will consider the conventional GB terminology within the framework of the interface-plane nomenclature. Apart from providing a basis for the geometrical description of all types of interfaces, the main advantages of the interface-plane terminology over the two CSL-based definitions of the macroscopic DOFs will then, hopefully, become apparent. The three principal advantages are the following:

1. The number of macroscopic DOFs of any particular type of GB is readily apparent, which is of considerable aid in structure–property investigations.
2. The geometrical resemblance between symmetrical and asymmetrical GBs is rather transparent, thus greatly facilitating the comparison of their physical properties.
3. The fact that – from a purely geometrical point of view – symmetrical and asymmetrical-**tilt** boundaries represent a special subset of symmetrical and asymmetrical-**twist** boundaries, respectively, is incorporated naturally into the interface-plane description of the macroscopic geometry.

Degrees

1.6.1 Mac
scheme')

As is well
ture(s) an
parameters
of a singl
DOFs are
scopic an
ones [18].
1.6.2, are
of a vecto
lations par
plane. By
the three c
methods c
atomic-leve
macroscopi
these three
referred to
(section 1.6

A simple
macroscop
or incomm
following (1

{DOFs}

Fig. 1.15 A de
21]. The unit v
coordinate syst
along the princ
defines the $(x_1$,
the top crystal

1.6.1 Macroscopic DOFs ('interface-plane scheme')

As is well known, in addition to the crystal structure(s) and lattice parameter(s) eight geometrical parameters are needed to characterize the geometry of a single bicrystalline interface. These eight DOFs are usually subdivided into the five **macroscopic** and three **translational** or **microscopic** ones [18]. The latter, to be discussed in section 1.6.2, are usually represented by the components of a vector, $\boldsymbol{T}$, associated with rigid-body translations parallel and perpendicular to the interface plane. By their very nature, the determination of the three components of $\boldsymbol{T}$ requires experimental methods capable of detecting 'microscopic' (i.e. atomic-level) translations. By contrast with the macroscopic DOFs and the atomic structure, these three translational DOFs are therefore often referred to as the **microscopic** DOFs of the GB (section 1.6.2 below).

A simple, unified method of defining the five **macroscopic** DOFs of an arbitrary (commensurate or incommensurate) bicrystalline interface is the following (Fig. 1.15): [20]

$$\{\text{DOFs}\} = \{\hat{n}_1, \hat{n}_2, \theta\} \quad \text{('interface-plane scheme')} \qquad (1.20)$$

Here the unit vectors $\hat{n}_1$ and $\hat{n}_2$ represent the common interface-plane normal, $\hat{n}$, in the two halves (Fig. 1.15(b)), referred to the same principal coordinate system (Fig. 1.15(a)). For example, the (x, y, z) system in Fig. 1.15(a) might be aligned along the $\langle 100 \rangle$ principal cubic directions, relative to which the interface-plane normals in the two halves may be defined. In Fig. 1.15(b) the two normals are then aligned parallel to each other, as indicated by the planar structure in the figure, thus defining the (x_1, y_1, z_1) and (x_2, y_2, z_2) coordinate systems. (Naturally, for **crystalline** interfaces $\hat{n}_1$ and $\hat{n}_2$ have to be directions permitted by the particular crystal structure.) Since each unit vector contributes two DOFs, the interface **plane** therefore represents four DOFs. Having thus fixed the interface plane in the two semi-crystals, the only remaining DOF is the one associated with a so-called 'twist' rotation, by the angle θ, about the common interface-plane normal, because any other rotation would change $\hat{n}_1$ and $\hat{n}_2$ (Fig. 1.15(c)).

Because of the emphasis placed on the interface **plane** (by assigning to it four out of the five DOFs), we will refer to the definition in eq. (1.20) as the 'interface-plane scheme' for defining the macroscopic DOFs. As already mentioned, two other CSL-based definitions, referred to as the 'CSL-

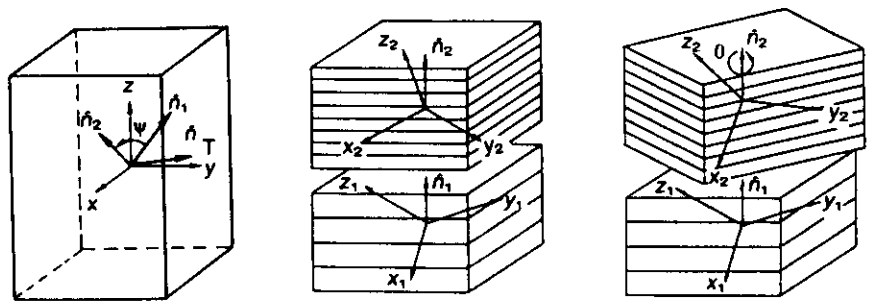

(a) (b) (c)

Fig. 1.15 A definition of the five **macroscopic** DOFs of an arbitrary (commensurate or incommensurate) bicrystalline interface [20, 21]. The unit vectors $\hat{n}_1$ and $\hat{n}_2$ represent the interface-plane normal, $\hat{n}$, in the two halves, however referred to the same principal coordinate system. (a) Illustrates the orientations of $\hat{n}_1$, $\hat{n}_2$, and $\hat{n}_T$ in a space-fixed (x, y, z) coordinate system (oriented, for example, along the principal cubic axes); $\hat{n}_T \equiv [\hat{n}_1 \times \hat{n}_2]/\sin\psi$. A tilt rotation of two identical (x, y, z) coordinate systems of (a) such that $\hat{n}_2 \parallel \hat{n}_1$ defines the (x_1, y_1, z_1) and (x_2, y_2, z_2) coordinate systems in (b). Finally, in (c) the twist component of the GB is introduced by rotating the top crystal in (b) about the GB-plane normal by the angle θ.

misorientation' and 'tilt-inclination' schemes, will be discussed in detail in sections 1.8.1 and 1.8.2 (eqs. (1.45) and (1.54), respectively). We mention that sometimes a sixth macroscopic DOF, representing the **position** of the interface plane in the direction of its normal, is added to the usual five defined here and in the two other schemes [18]; for a fixed (i.e. immobile) interface, however, this DOF is of no relevance.

In the case of GBs, a distinction is usually made between pure **tilt** and pure **twist** boundaries, with a **general** boundary having both tilt and twist components (and hence characterized by the full set of five DOFs; see section 1.8.2 below). This concept is rather useful as it provides information about the types of dislocations present in the GB structure, with the tilt and twist components defining, respectively, the edge- and screw-dislocation content. It can be adopted for other types of crystalline interfaces as well, including commensurate and incommensurate heterophase interfaces. As is common for GBs, we thus define a twist rotation as a rotation about an axis, described by the unit normal $\hat{n}_r$, which is parallel to the common interface-plane normal, $\hat{n}$ ($\hat{n}_r \parallel \hat{n}$). In a tilt rotation, by contrast, $\hat{n}_r$ and $\hat{n}$ are perpendicular to one another ($\hat{n}_r \perp \hat{n}$).

From these definitions, the tilt and twist components of a 'general' bicrystalline interface defined in eq. (1.20) are readily apparent. The angle θ, by definition, describes a twist rotation, since any other rotation would change the interface normal; the corresponding rotation matrix is denoted by $\boldsymbol{R}(\hat{n}_1, \theta)$. Provided we define $\theta = 0°$ as the angle for which the interface is of a pure tilt type (i.e. its structure contains only edge dislocations), the twist component of a general interface, defined by the rotation $\boldsymbol{R}(\hat{n}_1, \theta)$, is immediately obvious from the DOFs in eq. (1.20). The tilt component, characterized by the rotation matrix $\boldsymbol{R}(\hat{n}_T, \psi)$, is governed by the condition that $\hat{n}_T \perp \hat{n}_1, \hat{n}_2$ (Fig. 1.15(a)); hence [21]

$$\hat{n}_T = [\hat{n}_1 \times \hat{n}_2]/\sin\psi \tag{1.21}$$

with

$$\sin\psi = |[\hat{n}_1 \times \hat{n}_2]| \tag{1.22}$$

where $\hat{n}_T$ is a unit vector defining the orientation of the tilt axis, while ψ is the so-called tilt angle (Fig. 1.15(a)).

In much of the work on free surfaces, the tilt axis and tilt angle defined here are referred to as the **pole** axis and **pole** angle, respectively. This terminology is related to the **pole figure** in which the possible orientations of a unit vector are represented on the surface of a unit sphere (Fig. 1.16). This corresponds to defining the two DOFs of the unit vector in terms of spherical coordinates (section 1.6 below). The so-called **pole of a plane** thus represents, by its position on the unit sphere, the orientation of that plane. [22] A plane may also be represented by the great circle of the sphere which is perpendicular to the plane normal. For example, the great circles ABCD and KDMB in Fig. 1.16 represent, respectively, the planes with unit normals $\hat{n}_1$ and $\hat{n}_2$, whose poles are the points P_1 and P_2, respectively. The 'pole' axis and 'pole' angle, $\hat{n}_T$ and ψ, respectively, are the same as the 'tilt' axis and 'tilt' angle defined in eqs. (1.21) and (1.22).

Equations (1.21) and (1.22) illustrate that the tilt component of a **general interface** (i.e. one with all five DOFs, see Fig. 1.15(c)) is solely determined by the normals $\hat{n}_1$ and $\hat{n}_2$, i.e. by the interface **plane**. Irrespective of the value of the twist angle, θ, in eq. (1.20), an interface therefore has a tilt component whenever $\hat{n}_1$ and $\hat{n}_2$ represent different crystallographic directions or, if the interface is symmetrical (see below), different sets of crystallographically equivalent lattice planes. Because of the similarity of a general interface to a pure (i.e. symmetrical) twist boundary, a general interface will also be referred to as an **asymmetrical-twist** interface; however, because of the asymmetry in the interface plane, such an interface always has a tilt component (given by eqs. (1.21) and (1.22)), in contrast to the symmetrical-twist interface discussed below. In the special case for $\theta = 0°$ (and $\theta = 180°$; section 1.8.2), a pure **asymmetrical-tilt** interface with only 4 DOFs is obtained (see Fig. 1.15(b)). If the two lattice planes forming the GB are incommensurate (section 1.5), a unique definition of the origin of the twist rotation, i.e. of $\theta = 0°$, and of an asymmetrical-tilt configuration is not

Degrees

possible. F
commensur
For exar
normal, say
the substrat
assigned a
rotation fro
overlayer. I
the substrat
an asymme
in addition.
(i.e. for θ
asymmetric
Finally, i
be given ir
according tc

$\hat{n} = (h^2 +$

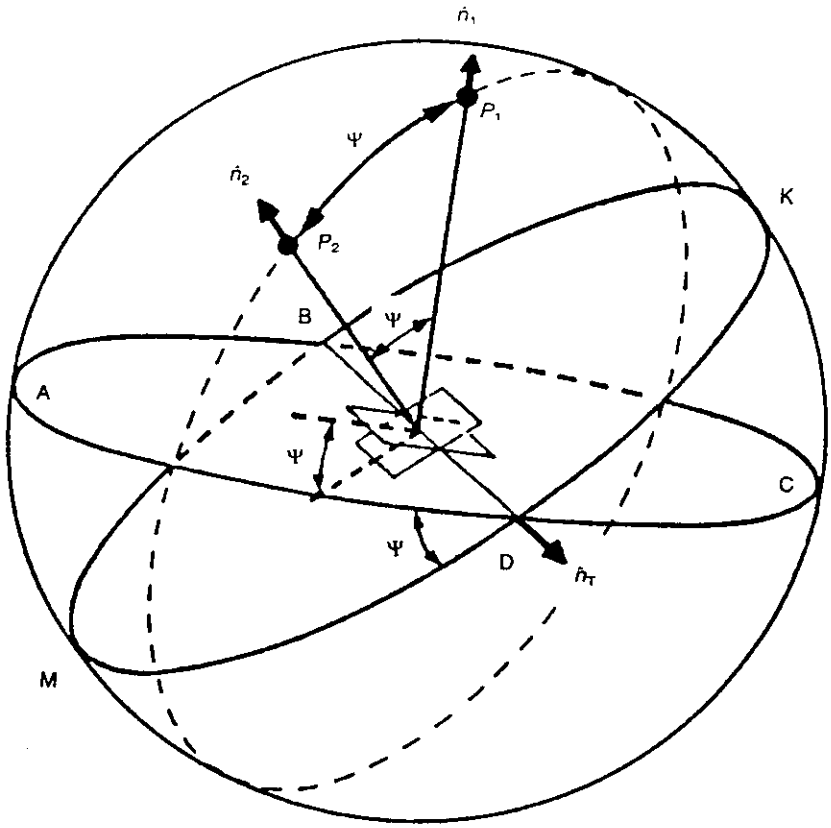

Fig. 1.16 Definition of the angle between two planes in terms of a pole figure [22]. The 'pole' axis and 'pole' angle, $\hat{n}_T$ and ψ, are identical to the 'tilt' axis and 'tilt' angle defined in eqs. (1.21) and (1.22). The great circles ABCD and KDMB represent, respectively, the planes with unit normals $\hat{n}_1$ and $\hat{n}_2$, whose poles are the points P_1 and P_2, respectively.

possible. Here, however, by considering only commensurate GBs, we avoid this issue altogether.

For example, a thin-film overlayer with a normal, say ⟨100⟩, which differs from that of the substrate, say with a ⟨111⟩ normal, may be assigned a tilt axis and angle expressing the rotation from the substrate normal to that of the overlayer. If the overlayer is perfectly aligned with the substrate (i.e. for $\theta = 0°$), the interface is of **an asymmetrical-tilt** type. If the overlayer is, in addition, rotated about the substrate normal (i.e. for $\theta \neq 0°$), the interface is a **general** or **asymmetrical-twist** interface (Fig. 1.15(c)).

Finally, in cubic crystals the normal $\hat{n}$ may be given in terms of the Miller indices, (hkl), according to

$$\hat{n} = (h^2 + k^2 + l^2)^{-\frac{1}{2}} \begin{pmatrix} h \\ k \\ l \end{pmatrix} \tag{1.23}$$

and all relevant geometrical parameters may be expressed in terms of the h, k and l associated with a given plane. The definition in eq. (1.20) may then be rewritten as follows:

$$\{\text{DOFs}\} = \{(h_1, k_1, l_1), (h_2, k_2, l_2), \theta\} \quad \text{('interface-plane scheme')} \tag{1.24}$$

where, in order to simplify the notation, the plane **normals** in eq. (1.20) have been replaced by the actual lattice **planes** forming the interface.

In a close parallel with the terminology commonly used for GBs (see section 1.8), one can classify the various types of interfaces described by eqs. (1.20) and (1.24). Thus, a **symmetrical** interface is defined as one for which $\hat{n}_1$ and $\hat{n}_2$ are linearly related, i.e. there exists a **linear** relationship,

$$\hat{n}_2 = L(\hat{n}_1) \tag{1.25a}$$

in the sense that $\hat{n}_1$ and $\hat{n}_2$ represent crystallographically equivalent lattice planes, which reduces the number of DOFs from five to only three:

$$\{\text{DOFs}\} = \{\hat{n}_1, \hat{n}_2 = L(\hat{n}_1), \theta\} \quad \text{(symmetrical interface)} \tag{1.26a}$$

All other interfaces are hence **asymmetrical**.

As an example for eq. (1.25a) we consider the collinearity condition,

$$\hat{n}_2 = \pm\hat{n}_1 \tag{1.25b}$$

Equation (1.26a) then becomes:

$$\{\text{DOFs}\} = \{\hat{n}_1, \pm\hat{n}_1, \theta\} \quad \text{(symmetrical twist)} \tag{1.26b}$$

An interface characterized by eq. (1.25b) obviously has no tilt component because $[\hat{n}_1 \times \hat{n}_2] = 0$. By analogy to the GB terminology, such an interface is therefore called a **symmetrical-twist** (or **pure twist**) interface. Analogously, as already mentioned, if the interface is asymmetrical (eq. (1.20)) we refer to it as an **asymmetrical-twist** interface.

For the + sign in eq. (1.26b), the two sets of lattice planes forming the interface are obviously identical, while the − sign describes a bicrystal in which one of its two halves has been turned upside down with respect to the other. To illustrate a simple relationship between the two sign choices, we consider a perfect crystal, which is obviously included in eq. (1.26b) as the special case in which

$$\{\text{DOFs}\} = \{\hat{n}_1, \hat{n}_1, \theta = 0°\} \tag{1.27a}$$

In a crystal lattice with inversion symmetry, in which a 180° rotation about some crystallographically allowed rotation axis inverts any lattice vector, $\boldsymbol{r}$ (i.e. $\boldsymbol{r} \rightarrow -\boldsymbol{r}$; section 1.7.2), a perfect crystal is also obtained for

$$\{\text{DOFs}\} = \{\hat{n}_1, -\hat{n}_1, \theta = 180°\} \tag{1.27b}$$

For any other value of θ, a **symmetrical-twist** interface is obtained. Since either of the two perfect-crystal configurations in eqs. (1.27a) and (1.27b) may be used as starting point for the twist rotation, the following relationship holds:

$$\{\text{DOFs}\} = \{\hat{n}_1, \hat{n}_1, \theta\} = \{\hat{n}_1, -\hat{n}_1, 180° - \theta\} \tag{1.28}$$

We emphasize that this relation is only valid for a crystal lattice with inversion symmetry (section 1.7.2).

At the atomic level, the most characteristic geometrical feature of a symmetrical-**tilt** grain boundary (STGB) is the inverted stacking of the lattice planes on one side of the interface with respect to the other (section 1.8.3). In a crystal lattice with inversion symmetry, STGBs may therefore be viewed as special twist boundaries (for $\theta = 180°$) [20]. Similar to the perfect crystal considered in eqs. (1.27a) and (1.27b), the STGB configuration is thus situated at the endpoints of the twist-rotation range, and is characterized as follows:

$$\{\text{DOFs}\} = \{\hat{n}_1, \hat{n}_1, \theta = 180°\} \quad \text{(symmetrical tilt)} \tag{1.29a}$$

or

$$\{\text{DOFs}\} = \{\hat{n}_1, -\hat{n}_1, \theta = 0°\} \quad \text{(symmetrical tilt)} \tag{1.29b}$$

The fact that STGBs may be viewed as a subset of symmetrical-twist boundaries translates into a unique atomic-level geometry of STGBs, in comparison with all other GBs (sections 1.7.3 and 1.8.4).

This definition of STGBs as a subset of symmetrical-twist boundaries is in apparent conflict with the fact that, according to eqs. (1.21) and (1.22), these interfaces have no tilt component. Moreover, if we identify the type of a GB as tilt or twist by the edge or screw dislocations in its structure, then STGBs should be classified as tilt and not twist boundaries. This apparent discrepancy originates from the fact that the example of the symmetry relation (1.25a) given in eq. (1.25b) does not cover all sets of crystallographically equivalent lattice planes which satisfy eq. (1.25a) but not (1.25b). To formally assign a tilt component to a symmetrical interface, a non-collinear combination of $\hat{n}_1$ and $\hat{n}_2$ has to be found which characterizes the same set of crystallographically equivalent planes. In a cubic crystal such sets are readily identified. For example, a GB formed by the two crystallographically equivalent (albeit not identical) sets (h, k, l) and $(k, h, -l)$, would

obviously be considered to be 'symmetrical', since on an atom-by-atom basis the two types of lattice planes are indistinguishable. Generally for cubic crystals, if we define $\hat{n}_1$ by the normal $[h_1, k_1, l_1]$, the general condition of symmetry [eq. (1.25a)] may be formulated as follows: [21]

$$[h_2, k_2, l_2] = \in \{\langle \pm h_1, \pm k_1, \pm l_1 \rangle\} \qquad (1.30)$$

where the angular brackets indicate that any permutation of the Miller indices, including their signs, is permitted. The set of normals, $\{\langle \pm h_1, \pm k_1, \pm l_1 \rangle\}$, obviously includes the collinear normals in eq. (1.25b) as the special cases in which $[h_2, k_2, l_2] = [h_1, k_1, l_1]$ or $[h_2, k_2, l_2] = [-h_1, -k_1, -l_1]$. Equation (1.30) thus represents the general condition of symmetry for cubic crystals.

1.6.2 Translational ('microscopic') DOFs

As already mentioned, the different types of interfaces discussed above still have three independent **translational** (or so-called microscopic) DOFs involving translations, $\boldsymbol{T} = (T_x, T_y, T_z)$, **parallel** (x, y) and perpendicular to the interface **plane** (z). From a thermodynamics point of view, **the** z component of $\boldsymbol{T}$ (parallel to the interface **normal**) is particularly important in that it accounts **for** any volume expansion at the interface. Such an **excess** free volume of the interface can be expected **to** (a) be closely related to its excess free energy and **(b)** give rise to stresses near the interface that are **similar** in nature to the well-known surface stress in **free** surfaces.

Similar to the definition of the excess free energy **of** the interface as the change in Gibbs free energy, G, with interface area, A, at constant temperature, T, pressure, p, and chemical composition (expressed in terms of the numbers of atoms, N_i, of **each** species), according to [23]

$$\gamma = (\partial G/\partial A)_{T,p,N_i} \qquad (1.31)$$

the so-called excess free volume per unit area of the **interface** is defined by [24]

$$\delta V = (\partial V/\partial A)_{T,p,N_i} \qquad (1.32)$$

By definition, δV is a volume expansion **per unit area** (and is conveniently given in units of the lattice parameter, a) and is to be distinguished from the overall three-dimensional thermodynamic volume, V.

According to eqs. (3.31) and (3.32), the Gibbsian excess free energy and free volume per unit area are to be determined while the temperature, pressure, and composition are held fixed. This constraint may pose particular conceptual problems in some computer simulations of these excess quantities. Following these definitions, simulations always require consideration of an appropriate interface-free reference system under the same conditions of T, p, and N_i as the interfacial system. For example, constant-volume simulations lead not only to numerically wrong values of γ for a given potential, but energies thus determined are conceptually not the true excess energy in the Gibbsian sense (which is the one usually determined experimentally).

In the case of GBs, the existence of translations parallel to the interface have been well established by means of high-resolution transmission-electron-microscopy (TEM) experiments, as well as computer simulations. These translations contribute to a lowering of the excess free energy of the system by avoiding energetically unfavorable translational states. They are also thought to play an important role during the process of GB migration [25, 26].

1.6.3 The three 'simplest' interface systems

Given that crystalline interfaces are **planar** defects, at least two macroscopic DOFs (namely the two associated with the interface normal) are required to characterize even the simplest interface. According to eq. (1.26b), such an interface is symmetrical and its twist angle must be fixed, or else be irrelevant altogether. There are in total three distinct types of **homophase** interfacial systems satisfying this condition, namely stacking faults, symmetrical-tilt grain boundaries (STGBs) and free surfaces (Fig. 1.17). Although not an internal interface, the free surface (a crystal–vacuum interface) is included here. Because of its importance as the final state in interfacial decohesion, a terminology and geometrical description in common to both internal interfaces and external

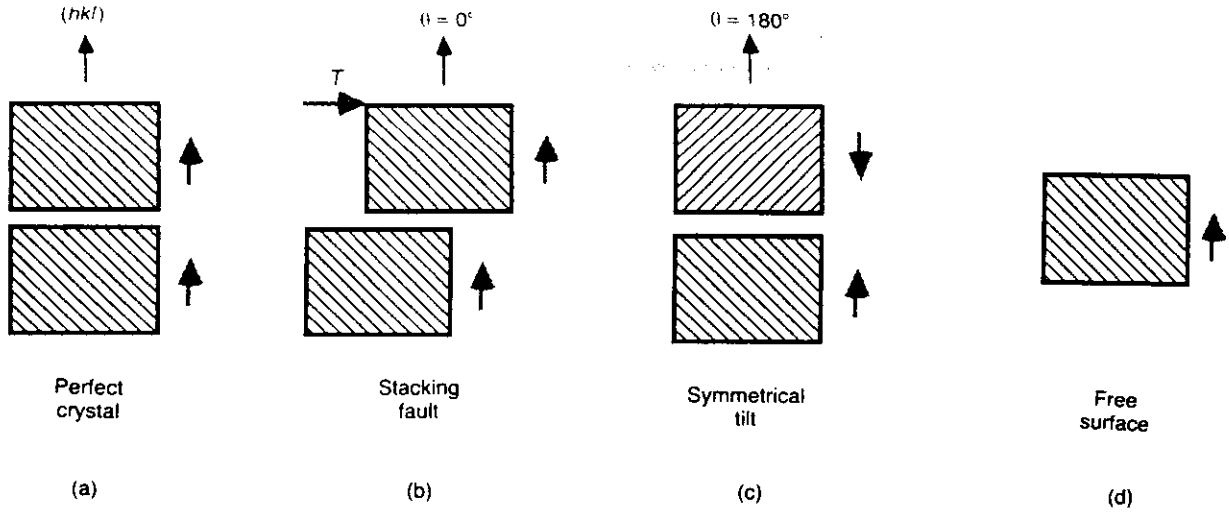

Fig. 1.17 From the point of view of the number of macroscopic DOFs involved, the stacking fault in (b), the symmetrical-tilt grain boundary (STGB: (c)) and the free surface in (d) represent the three simplest of all homophase planar defects (schematic). For comparison, a perfect crystal with the same crystallographic orientation is sketched in (a). The shaded arrows indicate the direction of planar stacking to be discussed in detail later. (An atomic-level view of these geometries is given in section 1.7.3; Fig. 1.30).

surfaces might facilitate a better understanding of interface fracture. From the point of view of the number of DOFs involved, these interfaces represent the simplest of all homophase interface systems. Among the **heterophase** systems, the coherent, incoherent and semi-coherent semi-bulk and thin-film (strained-layer) systems in Figs. 1.6, 1.10, and 1.11 and the topotaxy in Fig. 1.8 could also be included here. However, because of their geometrical similarity (particularly the coherent systems) with the three homophase systems described here, they will not be considered in this context.

First, a **stacking fault** may be generated on a given plane by any suitable in-plane translation, (T_x, T_y), of the perfect-crystal configuration in Fig. 1.17(a), thus destroying the perfect registry between the planes adjacent to the interface. Since no rotation is involved ($\theta = 0°$), in addition to these two translational DOFs, the stacking fault is characterized by only the two macroscopic DOFs associated with orientation of the fault plane. In principle, the translation may be accompanied by a volume expansion, hence requiring all three microscopic DOFs to be specified for its full characterization.

Second, the **symmetrical-tilt** GB on the same plane, with its familiar 'twinned' inversion of the stacking sequence of lattice planes at the interface (Fig. 1.17(c)), is obtained by simply turning one of the two halves upside down. As discussed in more detail in sections 1.7.3 and 1.8.4 below, in crystal lattices with inversion symmetry, the STGB configuration on a given plane is obtained simply from a 180°-twist rotation of, say, the upper semicrystal. If the components of $\boldsymbol{T}$ are such that one plane is a mirror plane (i.e. shared by both semicrystals), this inverted configuration represents a **special twin**, to be distinguished from the **general-twin** configuration obtained for some arbitrary translation (and hence merely with an inverted planar stacking at the interface, but without a mirror plane; for details see section 1.8.3 and Fig. 1.30).

Third, the free surface on a given plane (Fig. 1.17(d)), also with only two macroscopic DOFs, differs from the stacking fault and the symmetrical-tilt configuration on the same plane by not having

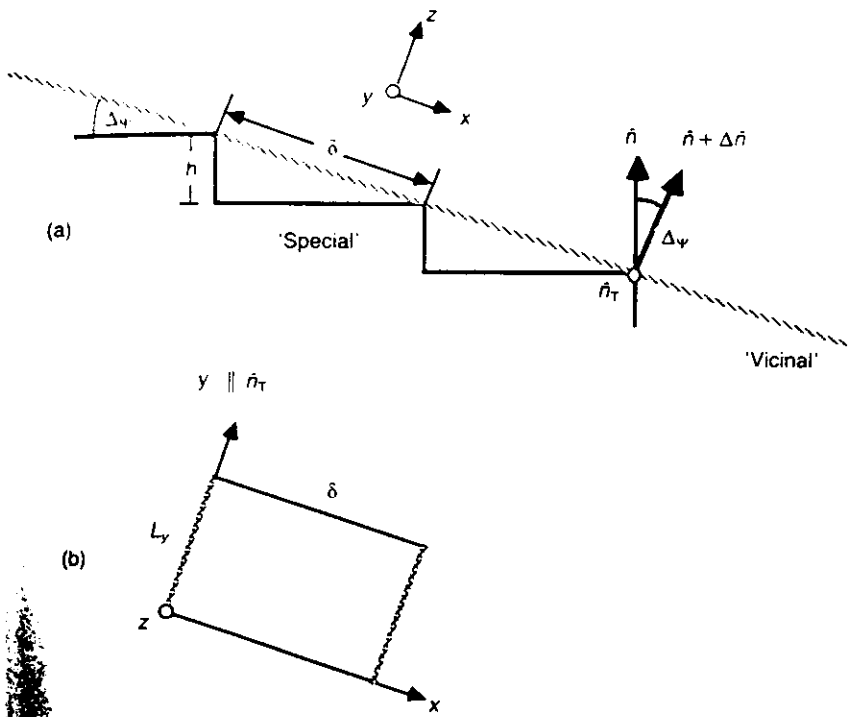

Fig. 1.18 Distinction between 'special' and 'vicinal' surfaces. While the special surface, with normal $\hat{n}$, represents a cusped minimum-energy orientation in the $\gamma(\hat{n})$ plot, the geometry, atomic structure, and physical properties of vicinal (i.e. nearby) surfaces are governed by those of the special surface and by the spacing between and the geometry of its steps.

any translational DOFs, as in the case of the perfect crystal. Formally, the free surface may be viewed as having been generated from the perfect crystal, the stacking fault, or the STGB as the limit in which $T_z \rightarrow \infty$, thus creating a symmetrical arrangement of two infinitely separated (i.e. non-interacting) surfaces. The magnitudes of T_x and T_y are then obviously irrelevant, as is the twist angle θ, and no microscopic DOFs are required to characterize the surface.

In spite of these geometrical similarities between the simplest three interface systems, which will be investigated further at the atomic level in section 1.4.3 below, to date little is known about any similarities in their physical properties [27].

1.6.4 'Vicinal' versus 'special' interfaces

While in the case of external surfaces a distinction between 'special' and 'vicinal' interface planes has been commonly made for almost a century [28], in the case of internal interfaces such a distinction has only recently been suggested [29]. To illustrate these concepts for the case of free surfaces, we consider a 'special' low-index surface with normal $\hat{n}$ which is as nearly as possible atomically 'flat' (i.e. free of steps), and a second surface with a slightly different orientation, say, $\hat{n} + \Delta\hat{n}$ [27]. If $\Delta\hat{n}$ is small, the second surface will look just like the first one, except for the appearance of widely separated steps (Fig. 1.18). Because each step adds to the surface energy, $\gamma(\hat{n} + \Delta\hat{n}) - \gamma(\hat{n})$ will be positive for any orientation of $\Delta\hat{n}$ and, for small values of $\Delta\hat{n}$, will be asymptotically proportional to the density of steps. The surface with normal $\hat{n}$ hence represents a **cusped** minimum-energy orientation in a $\gamma(\hat{n})$ plot [27]. Such a surface is called a **special** surface; it is distinguished from the nearby **vicinal** surfaces whose geometry, atomic structure, and physical properties are governed by those of the special surface and by the vector difference, $\Delta\hat{n}$, in the phase space representing the two macroscopic DOFs associated with the surface normal, $\hat{n}$.

As illustrated in Fig. 1.18, the misorientation

between $\hat{n}$ and $\hat{n} + \Delta\hat{n}$ may be characterized by the rotation axis, $\hat{n}_T$, and rotation angle, $\Delta\psi$ (given by eqs. (1.21) and (1.22), respectively), and for a fixed rotation axis the surface energy may be expressed solely as a function of $\Delta\psi$. Assuming the steps to be far enough apart that their mutual interaction may be ignored, one can easily show that [27, 30].

$$\gamma(\Delta\psi) = \gamma_{cusp} \cos \Delta\psi + \Gamma^{\infty} \sin \Delta\psi/h \qquad (1.33)$$

where γ_{cusp} denotes the cusped energy of the special surface and Γ^{∞} represents the energy per unit length of individual steps whose height is denoted by h (Fig. 1.18).

In the example shown in Fig. 1.19, the unrelaxed and relaxed zero-temperature energies of fcc surfaces perpendicular to a ⟨110⟩ pole axis are plotted against 2ψ which is defined as the angle of a particular surface with respect to the (110) plane. These energies were determined [31] by means of the simple Lennard-Jones (LJ) potential fitted to the lattice parameter and approximate melting point of Cu, although this potential function is usually thought to be more appropriate for noble-gas crystals. The fact that the unrelaxed and relaxed energies differ by only very little indicates that (i) the change in surface energy as a function of $\Delta\psi$ is governed by strictly crystallographic factors, namely the total length of the steps, and (ii) the interaction between steps, given by the relaxation energy, is, indeed, very small.

Figure 1.19 demonstrates the existence of three cusped 'special' orientations associated with the three principal planes in the fcc lattice, namely (111), (100), and (100). Being the densest planes in the fcc lattice, the smallest number of nearest-neighbor bonds is broken when one of these surfaces is created. This is thought to be the reason for the appearance of cusps for these particular surfaces, with the depths of the cusps decreasing rapidly with decreasing planar density, i.e. interplanar lattice spacing, $d(hkl)$ (Table 1.1). A detailed analysis of the smooth variation of $\gamma(\Delta\psi)$ in the vicinity of the cusps [27] indicates that eq. (1.33) provides an excellent representation of the simulation data near all three cusps; such an analysis also provides values of the step energy per unit length for all three types of steps.

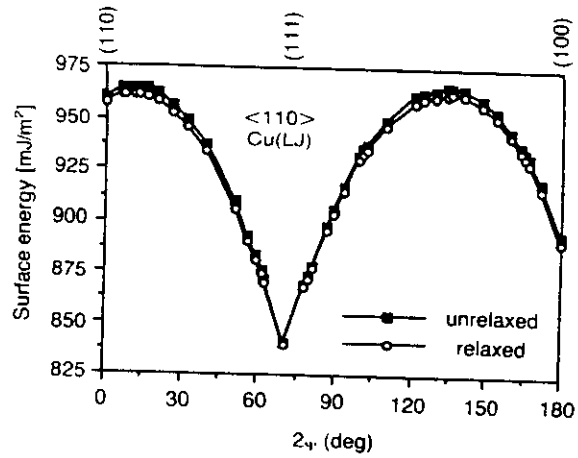

Fig. 1.19 Unrelaxed and relaxed zero-temperature energies of fcc surfaces (computed by means of a Lennard-Jones potential fitted for Cu), plotted against the tilt angle of each surface with respect to the (110) plane. All surfaces are perpendicular to the ⟨110⟩ pole axis [31].

Table 1.1 Interplanar spacing, $d(hkl)$ (in units of the lattice parameter a), and number of planes in the repeat stacking sequence, $P(hkl)$ (the so-called stacking period), for the most widely spaced planes in the fcc lattice. According to eq. (1.44), these planes also correspond to the ones with the highest planar density of atoms

No.	(hkl)	$(h^2 + k^2 + l^2)$	$P(hkl)$	$d(hkl)/a$
1	(111)	3	3	0.5774
2	(100)	1	2	0.5000
3	(110)	2	2	0.3535
4	(113)	11	11	0.3015
5	(331)	19	38	0.2294
6	(210)	5	10	0.2236
7	(112)	6	6	0.2041
8	(115)	27	27	0.1925

Plots similar to Fig. 1.19 have also been obtained for symmetrical and asymmetrical-tilt and twist GBs, suggesting that the distinction between 'special' and 'vicinal' interfaces is meaningful for GBs as well as for free surfaces. In particular, most (symmetrical or asymmetrical) **low-angle twist** boundaries may be viewed as vicinal to the corresponding **tilt** boundaries (sections 1.8.2 and 1.8.3). A well known special case is that of symmetrical low-angle twist boundaries which may be

considered as vicinals of the perfect crystal. Similar to the steps in free surfaces, the dislocation structure of these GBs preserves areas of perfect crystal. (For further details, see [27] and [32] and sections 1.8.2 and 1.8.3.)

Finally, we mention that the distinction between special and vicinal interfaces is not possible on a strictly crystallographic basis alone because the identification of the special interfaces requires a knowledge of the relaxed energy of the system. Free surfaces represent somewhat of an exception in that geometrical concepts, based for example on the number of broken bonds per unit area, are very useful in predicting some of their basic properties [31].

1.6.5 Misorientation phase space

One of the main goals of structure-property investigations is the exploration of the so-called **misorientation phase space** represented by the five **macroscopic** DOFs of the interface. In principle, any property in this five-dimensional (5D) phase space, say, the interface energy γ, can therefore be represented as a 6D hypersurface, $\gamma(\hat{n}_1, \hat{n}_2, \theta)$. Needless to say, even a mere geometrical representation of such a hypersurface, perhaps via 3D cross-sections, is a non-trivial conceptual undertaking. Any symmetries which reduce the number of DOFs should therefore be fully exploited because they simplify the misorientation phase space considerably; a knowledge of the exact number of DOFs of the interfacial system under investigation is therefore imperative.

To illustrate possible ways of exploring misorientation phase space, we start with the simplest interface systems, characterized by only the two macroscopic DOFs associated with the crystallographic orientation of the interface normal, $\hat{n}$. The generally 6D structure-energy hypersurface, $\gamma(\hat{n}_1, \hat{n}_2, \theta)$, thus degenerates into a single 3D plot, $\gamma(\hat{n})$, which can be constructed as follows. For simplicity we limit ourselves to cubic crystals for which, when all symmetry operations are considered, all possible orientations of $\hat{n}$ fall into a triangle on the unit sphere of Fig. 1.16, with the principal cubic poles at its corners (see the shaded triangle in Fig. 1.20). Naturally, it is desirable to project this spherical triangle onto a plane (Fig. 1.20) by the so-called **stereographic projection** [22]. However, because of the highly non-linear nature of this projection, the angle scale of the **stereographic triangle** thus obtained is non-linear, which renders its use a somewhat complicated endeavor.

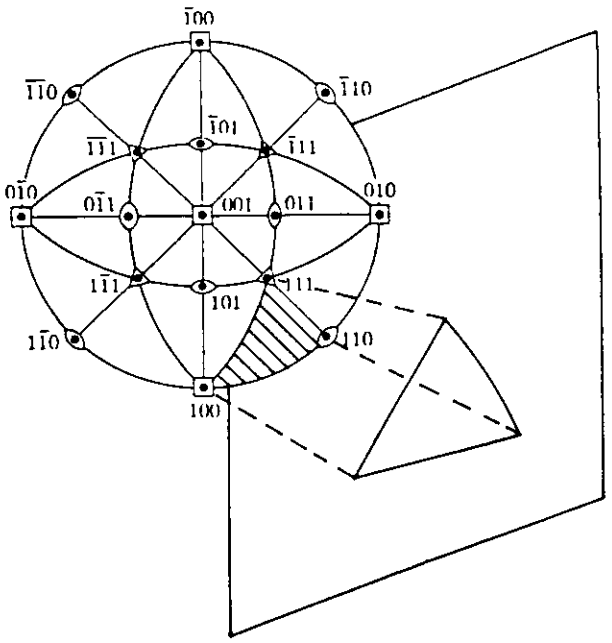

Fig. 1.20 Standard projection for cubic crystals of the unit sphere of Fig. 1.16 onto a plane, with the (001) pole in the center (so-called 'projection on (001)'). Due to the cubic symmetry, all possible orientations of a unit vector fall into a spherical triangle, such as the shaded one. (For details see Ref. [22]).

To simplify this projection while yet still capturing the essential features of the stereographic triangle, however, we express the orientation of $\hat{n}$ in terms of spherical coordinates, ϑ and φ, according to (eq. (1.23))

$$(h^2 + k^2 + l^2)^{-\frac{1}{2}} \begin{pmatrix} h \\ k \\ l \end{pmatrix} = \begin{pmatrix} \sin\vartheta\cos\varphi \\ \sin\vartheta\sin\varphi \\ \cos\vartheta \end{pmatrix} \qquad (1.34)$$

For $h \geq k \geq l$, all orientations of $\hat{n} = (h^2 + k^2 + l^2)^{-\frac{1}{2}}(h, k, l)$ then fall into the **phase-space triangle**

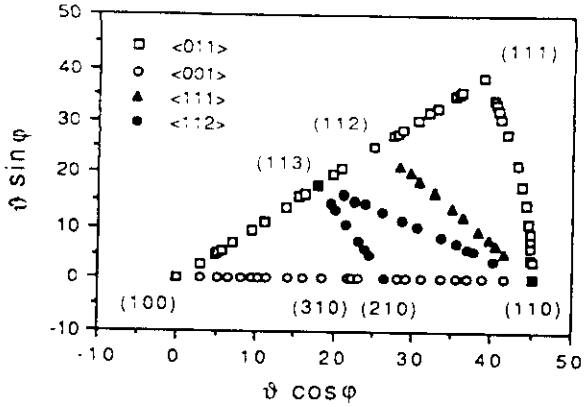

Fig. 1.21 Schematic plot, similar to the stereographic projection, of the spherical triangle of Fig. 1.20 onto a plane. ϑ and φ are the usual spherical coordinates which define the orientation of the interface normal according to eq. (1.34); ϑ is in degrees. The symbols indicate positions in the phase-space triangle at which the free-surface energy in Fig. 1.22(a) was determined [31].

sketched in Fig. 1.21, with the three principal cubic orientations at the corners [31]. This triangle differs slightly from the conventional stereographic triangle sketched in Fig. 1.20 in that its axes are scaled **linearly**. Given values of ϑ and φ, this simplification makes it a rather straightforward matter to locate its position within the triangle. As in the stereographic triangle, all orientations perpendicular to a $\langle 110 \rangle$ pole axis appear along the edge connecting (100), via (113), (112), and (111), with (110). Similarly, all orientations perpendicular to a $\langle 100 \rangle$ pole axis appear along the edge connecting (100) more directly with (110) via (310) and (210)], while plane orientations perpendicular to $\langle 111 \rangle$, $\langle 112 \rangle$, etc. cover the central regions of the triangle.

Using this phase-space triangle as the base plane, the surface energy, $\gamma(\hat{n}) \equiv \gamma(\vartheta, \varphi)$, obtained by means of the LJ potential is given by the 3D structure–energy plot shown in Fig. 1.22(a). By contrast with the 2D cross-section in Fig. 1.19 (along the edge connecting (100), via (113), (112), and (111), with (110)), this plot demonstrates the full extent in phase space of the three energy cusps at the corners of the triangle, with a remarkable absence of cusps in the central regions of the phase space. Figure 1.22(b) represents a similar plot for the number of broken nearest-neighbor bonds per unit surface area. The remarkable similarity of Figs. 1.22(a) and (b) demonstrates that the structure-energy correlation for free surfaces in fcc crystals is dominated by geometrical factors, with elastic effects associated with the interactions between the surface steps being relatively unimportant [27, 31]. We mention in passing that a similar plot is obtained for symmetrical-tilt GBs [33]. Combining the two plots permits one to determine the work of adhesion (i.e. the ideal cleavage-fracture energy)

$$E^{\mathrm{cl}}(\vartheta, \varphi) = 2\gamma(\vartheta, \varphi) - E^{\mathrm{STGB}}(\vartheta, \varphi) \qquad (1.35)$$

in the entire 2D phase space [27, 33].

If the twist angle, θ, is now added as a third DOF, every point in the 2D-phase-space triangle associated with the interface plane is unfolded into a infinite number of θ values which, in Fig. 1.21, are projected into a single point. Any structure–property correlation for symmetrical interfaces may hence be thought of as a 4D hypersurface.

To illustrate a method for constructing 3D cross-sections through this hypersurface, we briefly consider the case of symmetrical GBs [33]. As already mentioned, the 3D phase space for these boundaries contains infinitely many twist boundaries for every STGB (section 1.6.1). To gain some insight into what the corresponding 4D structure–energy hypersurface might look like and, in particular, to illustrate the distribution of the tilt and twist boundaries in this phase space, we consider cross-sections obtained as follows. In each 3D cross-section we limit ourselves to a well-defined subset of lattice planes, defined to be perpendicular to a particular pole (or tilt) axis, such as $\langle 110 \rangle$, $\langle 100 \rangle$, $\langle 111 \rangle$, $\langle 112 \rangle$, etc. By fixing the tilt axis, a single tilt angle, ψ, uniquely defines a given GB plane (see, for example, Fig. 1.21). Combined with the twist angle, θ, a 3D cross-section of the structure–energy phase space may thus be obtained for any given tilt axis.

One such cross-section, perpendicular to a $\langle 110 \rangle$ tilt axis, is shown in Fig. 1.23 for the same Cu(LJ) potential used above. On each plane, i.e. for each value of the tilt angle, the STGB configuration appears at the twist angle $\theta = 180°$ (while all other

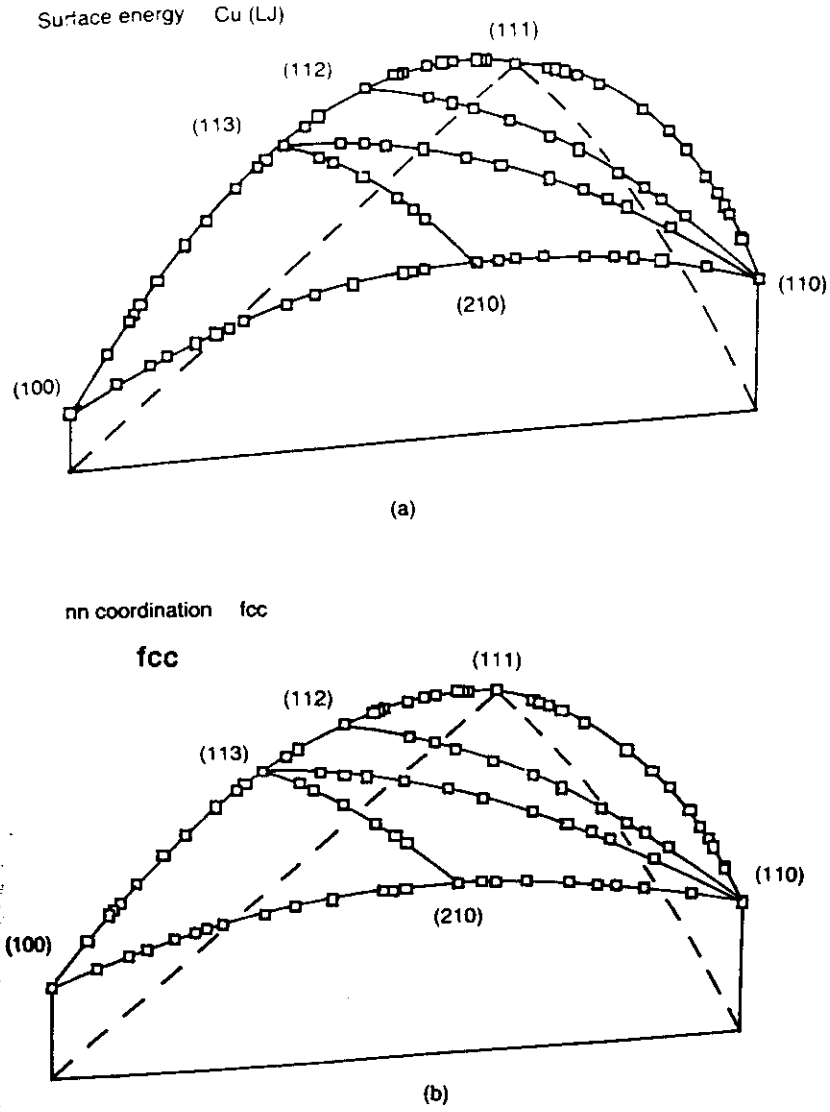

Fig. 1.22 (a) Three-dimensional structure–energy plot for free surfaces in fcc crystals (in arbitrary units, simulated by means of the Cu(LJ) potential), with the 2D-phase-space triangle of Fig. 1.21 as base plane [31]. (b) Nearest-neighbor miscoordination per unit area for the same surfaces.

GBs are pure twist boundaries), demonstrating the geometrical uniqueness of the STGBs in the phase space (sections 1.7.3 and 1.8.3). The deep energy cusps at the corresponding $\theta = 180°$ angles indicates that this unique geometry translates into a particularly low GB energy. The deep valley at the (111) plane demonstrates that the densest plane of the fcc lattice is a 'special' GB plane, with the slopes of the valley representing 'vicinal' GB-plane orientations. (Notice that the endpoint of the (111) valley at $\theta = 180°$ represents the well-known (111) twin boundary.)

Finally, the GB and free surface energies in Figs. 1.22(a) and 1.23 can be combined to determine the variation of the ideal-cleavage energy,

$$E^{cl}(\vartheta, \varphi, \theta) = 2\gamma(\vartheta, \varphi) - E^{GB}(\vartheta, \varphi, \theta) \quad (1.36)$$

in the three-parameter phase space for all symmetrical GBs. A $\langle 110 \rangle$ cross section through this 4D hypersurface, similar to Fig. 1.23, is shown in

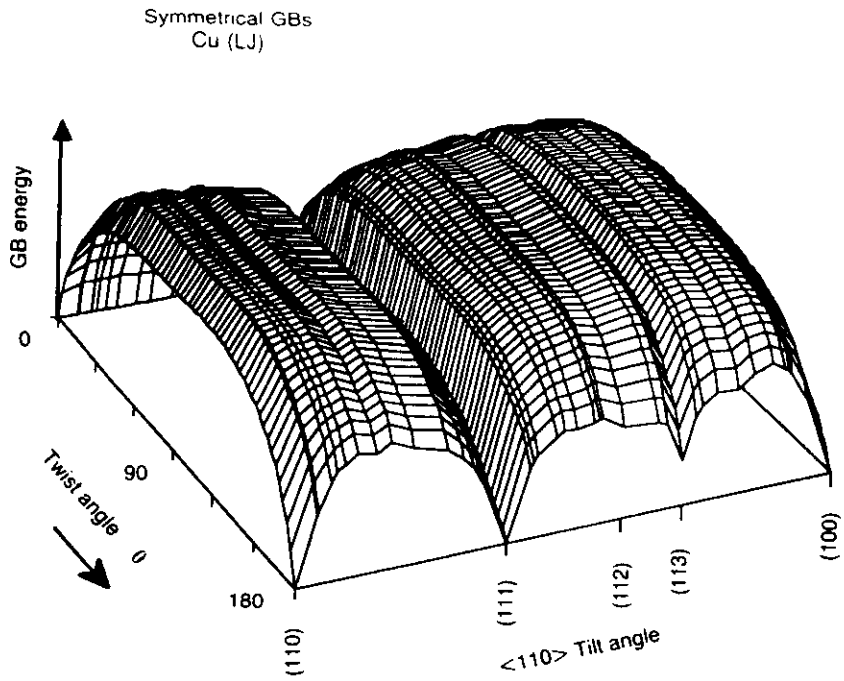

Fig. 1.23 Three-dimensional cross section of the 4D structure–energy plot for symmetrical GBs in fcc metals for the Cu(LJ) potential (in arbitrary units). In the particular cross section shown here, only GB planes perpendicular to a ⟨110⟩ tilt axis are considered (see also Fig. 1.21) [33].

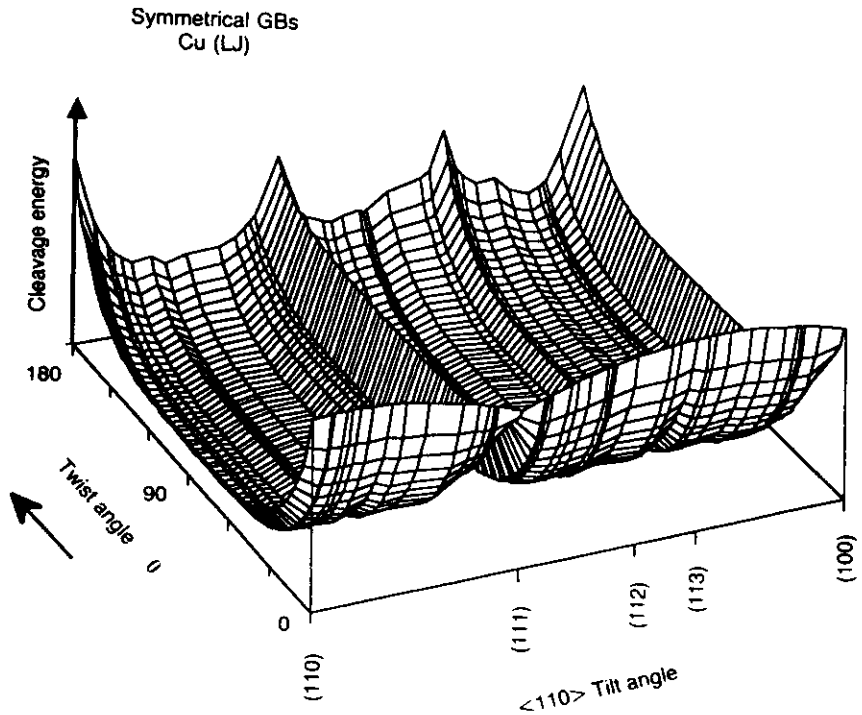

Fig. 1.24 Three-dimensional ⟨110⟩ cross section similar to Fig. 1.23 for the ideal cleavage-fracture energy (see eq. (1.36)) of symmetrical GBs in fcc metals for the Cu(LJ) potential (in arbitrary units). To show more clearly the bulk-cleavage energies, 2γ (at $\theta = 0°$), the direction of increasing twist angle was chosen opposite to that in Fig. 1.23 [33].

Fig. 1.24. Notice that, for reasons of clarity, the direction of increasing twist angle was chosen opposite to that in Fig. 1.23. We point out that, since for zero twist angle a perfect crystal is obtained (eq. (1.27a)), the cleavage energy at $\theta = 0^\circ$, $E^{cl}(\vartheta, \varphi, 0^\circ)$, represents the energy to cleave a perfect fcc crystal along a specific plane, i.e. twice the energy of the related free surface, $2\gamma(\vartheta, \varphi)$.

If the free-surface energy, γ, were isotropic (i.e. independent of ϑ and φ), Fig. 1.24 would represent merely an upside-down version of Fig. 1.23). However, as discussed earlier in Fig. 1.22(a), γ varies significantly in the two-parameter phase space, although its variation is not as pronounced as that of the GBs.

1.7 ATOMIC-LEVEL GEOMETRY OF PLANAR STACKING

Following the focus in the preceding section on the macroscopic geometrical description of crystalline interfaces, we are now ready to take the geometrical characterization one step further, down to the level of the atoms (albeit in their unrelaxed positions). This leads us naturally to the concept of the **atomic-level geometry** of solid interfaces, from which the concepts of coherency, commensurability, epitaxy and topotaxy discussed in section 1.2 follow logically. As an example, in section 1.7.3 the three simplest interface systems discussed earlier only at the macroscopic level (see section 1.6.3), will be revisited. Later on, in section 1.8, the atomic-level geometry of GBs will be discussed within the same framework.

1.7.1 Planar stacking in Bravais lattices

Since in both of its halves a crystalline interface contains stacks of well-defined lattice planes, in the following we briefly consider some basic geometrical definitions and properties associated with the planar stacking in a perfect Bravais lattice. Similar to Fig. 1.12, the underlying three-dimensional Bravais lattice is defined by the three Bravais vectors, a_1, a_2, and a_3, defined in Fig. 1.25 with

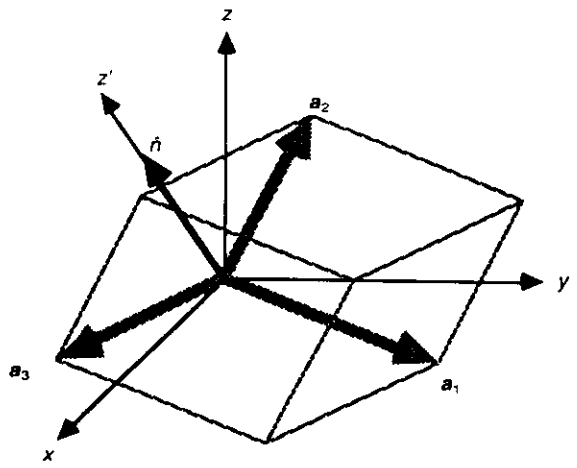

Fig. 1.25 Definition of a three-dimensional Bravais lattice by the Bravais vectors a_1, a_2, and a_3 in a Cartesian (x, y, z) coordinate system. z' defines some arbitrary direction in the lattice, with unit normal $\hat{n}$.

respect to a Cartesian (x, y, z) coordinate system. For simplicity we assume the basis attached to the Bravais lattice to contain only one atom such that the crystal lattice, identical to the Bravais lattice, is simply given by

$$r = la_1 + ma_2 + na_3 \tag{1.37}$$

with $l, m, n = 0, \pm 1, \pm 2, \ldots$. The conventional geometrical description of the crystal lattice is then based on the primitive unit cell sketched in Fig. 1.25 which, together with its periodic images, defines the lattice completely.

In crystalline interface materials, a different choice of the primitive periodic Bravais unit cell, which emphasizes the plane-by-plane arrangement of the atoms and hence greatly facilitates the visualization of the atomic structure, is often advantageous. We start by defining an arbitrary (but rational) direction, z', defined in Fig. 1.25 by some unit vector $\hat{n}$, which represents the normal to a set of lattice planes which we will choose as the lattice planes of interest. The (x', y', z') coordinate system in Fig. 1.26(a) is then chosen such that the generally non-orthogonal x' and y' directions point along the edges c_1, c_2 of the primitive **planar** Bravais unit cell of the plane with normal $\hat{n}$, while the z' direction (orthogonal to the x'–y' plane) is

defined in Fig. 1.25 to be parallel to the normal $\hat{n}$. In this new coordinate system, the atom positions are given by the new basis vectors c_1, c_2, and c_3, according to (Fig. 1.26)

$$r' = l'c_1 + m'c_2 + n'c_3 \qquad (1.38)$$

with $l', m', n' = 0, \pm 1, \pm 2, \ldots$. While the vectors c_1 and c_2 define the primitive **planar** unit cell (with plane normal $\hat{n}$), the out-of-plane vector c_3 enables one to proceed successively from one lattice plane to the next. It is important to recognize that the vector $c_3 = d + e$ does not generally point along the z' direction; this gives rise to a staggering of the planes. While its out-of-plane component, d (along z'), is determined by the interplanar spacing in the direction of $\hat{n}$, $d = |d|$, the relative translation of one plane relative to another is governed by e, the in-plane component of c_3. The 'natural' coordinate system associated with a given direction, $\hat{n}$, in the crystal is therefore the (x', y', z'') system shown in Fig. 1.26(a): Within the plane the atom sites are given by the vectors c_1 and c_2 whereas the z''-direction, parallel to c_3, defines the 'direction of staggering' of one plane relative to a neighboring one. In this coordinate system all lattice planes are consequently identical, with no net in-plane (x', y') translation required as one proceeds from one plane to a neighboring one. The 3D unit cell of this lattice is sketched in Fig. 1.26(b).

To express the new, **plane-based** primitive Bravais vectors, c_1, c_2, and c_3, in terms of the primitive vectors, a_1, a_2, and a_3, of the **conventional** Bravais lattice and the normal $\hat{n}$ simply requires the projection of a_1, a_2, and a_3 onto the plane and the z' direction (parallel to $\hat{n}$). Since both the conventional (a_1, a_2, a_3) and the plane-based (c_1, c_2, c_3) Bravais unit cells are primitive (i.e. contain exactly one lattice site), with volume Ω, the two have identical volumes, i.e.

$$([a_1 \times a_2] \cdot a_3) = ([c_1 \times c_2] \cdot c_3) = \Omega \qquad (1.39)$$

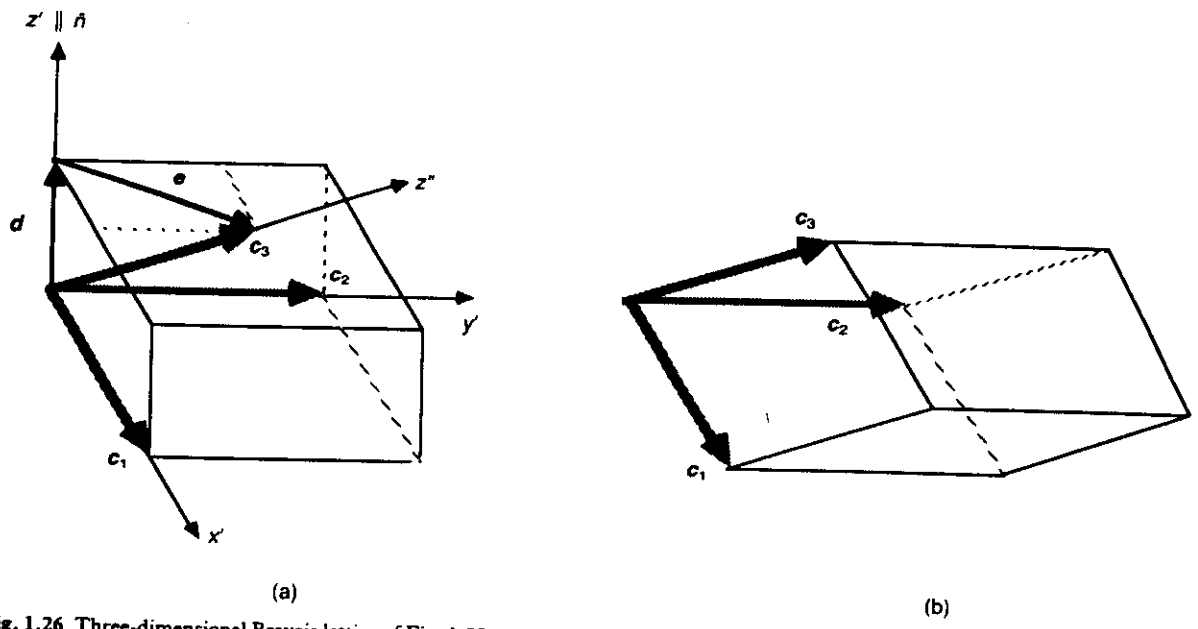

Fig. 1.26 Three-dimensional Bravais lattice of Fig. 1.25 projected into an (x', y', z') coordinate system chosen such that $z' \parallel \hat{n}$ while the (generally non-orthogonal) x' and y' directions point along the edges of the primitive **planar** Bravais unit cell of the plane with normal $\hat{n}$. The out-of-plane component of c_3, d (along z'), is determined by the interplanar spacing in the direction of $\hat{n}$. By contrast, the relative translation of one plane relative to another ('staggering of planes') is governed by the in-plane component of c_3, e. The primitive **volume** unit cell of the Bravais lattice, defined by c_1, c_2, and c_3, is sketched in (b).

A simple example of the two Bravais representations is shown in Fig. 1.27 for the (001) plane in the fcc lattice. Because both a_1 ($\parallel$ [110]) and a_2 ($\parallel$ [$\bar{1}$10]) lie in the (001) plane, in this case the vectors a_1, a_2, and a_3 of the well-known rhombohedral primitive fcc unit cell are identical to the vectors c_1, c_2, and c_3, with the vectors d and e along [001] and [010], respectively.

Given that the lattice planes are in general staggered, an obvious question concerns the number of lattice planes in the repeat stacking unit, sometimes referred to as the **stacking period**, P. The well-known . . . |ABC|ABC| . . . stacking of the (111) planes in the fcc lattice is an example of a three-plane stacking period; also, the two-plane . . . |AB|AB| . . . stacking period of the (001) and (011) planes is readily recognized. To determine P, one has to find the nearest lattice plane in the direction of $\hat{n}$ in the Cartesian coordinate system which is identical to the plane through the origin (i.e. entirely untranslated or translated by a multiple of the planar unit-cell dimensions); i.e. P is the smallest integer which satisfies the condition (eq. (1.38))

$$Pe = l'c_1 + m'c_2 \tag{1.40}$$

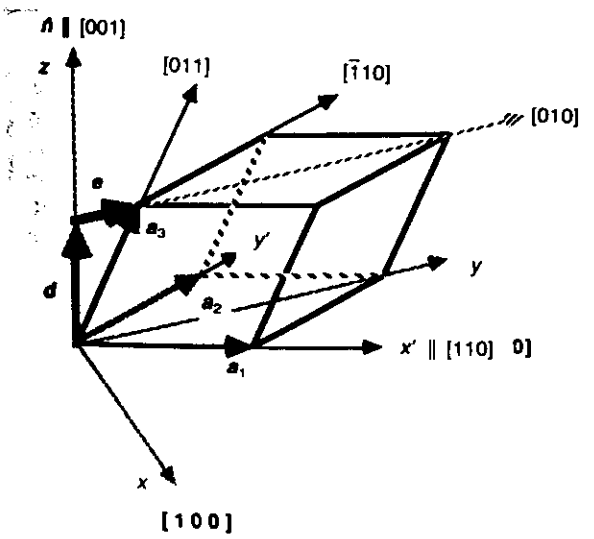

Fig. 1.27 Conventional (a_1, a_2, a_3) and (001)-plane-based (c_1, c_2, c_3) fcc Bravais lattices (see also Figs. 1.25 and 1.26). Since a_1 and a_2 lie in the (001) plane, $c_1 \equiv a_1$ and $c_2 \equiv a_2$ in this case.

with l' or $m' = 0, \pm 1$, etc. and e, c_1, and c_2 as defined in Fig. 1.26(a).

To illustrate eq. (1.40) we consider a cubic crystal in which the normal $\hat{n}$ may be given in terms of the Miller indices (hkl) (eq. (1.24)). All relevant geometrical parameters, including P, may then be expressed in terms of the Miller indices. For example, in a Cartesian coordinate system the interplanar spacing, $|d| = d(hkl)$ (Fig. 1.26(a)), is given by the well-known expression

$$d(hkl) = \varepsilon a(h^2 + k^2 + l^2)^{-\frac{1}{2}}, \quad (\varepsilon = 0.5 \text{ or } 1) \tag{1.41}$$

where a is the cubic lattice parameter and where the value of $\varepsilon(=0.5$ or 1) depends on the particular combination of odd and even Miller indices. (For example, in the fcc lattice, $\varepsilon = 1$ if h, k, and l are all odd but 0.5 otherwise.) The period, $P \equiv P(hkl)$, is similarly given by

$$P(hkl) = \delta(h^2 + k^2 + l^2), \quad (\delta = 1 \text{ or } 2) \tag{1.42}$$

where the value of δ (=1 or 2) also has to be determined in each case by inspection of the various odd and even combinations of Miller indices.

To illustrate these expressions, in Tables 1.1 and 1.2 the values of $d(hkl)$ and $P(hkl)$ are listed for the eight planes of the fcc and bcc lattices with the largest values of $d(hkl)$. Also, Fig. 1.28 shows schematically a **unit stack** of lattice planes, labeled . . . |AB . . IJ| . . . , in a direction with $P(hkl) = 10$ planes in the stacking period (such as the ⟨210⟩ direction of the fcc lattice; Table 1.1). The x' and z' axes, parallel to c_1 and d, respectively, are the same ones shown in Fig. 1.26(a),

Table 1.2 Same as Table 1.1, but for the bcc lattice

No.	(*hkl*)	$(h^2 + k^2 + l^2)$	*P*(*hkl*)	*d*(*hkl*)/*a*
1	(110)	2	2	0.7071
2	(100)	1	2	0.5000
3	(112)	6	6	0.4082
4	(310)	10	10	0.3162
5	(111)	3	3	0.2887
6	(321)	14	14	0.2673
7	(114)	18	18	0.2357
8	(210)	5	10	0.2236

and periodic border conditions are implied in all three dimensions. Figure 1.28 illustrates the constant in-plane translation, e, as one proceeds from one plane to another. Because of the periodicity parallel to the plane, the lattice site in plane F, which would normally fall outside of the unit cell as the vector e is added to the E plane, is reflected back into the unit cell.

The unit stack shown in Fig. 1.28 is obviously comprised of $P(hkl) = 10$ primitive plane-based Bravais unit cells c_1, c_2, and c_3. Since each plane contains exactly one atom (because we have chosen a basis containing only one atom), the planar unit-cell area, $A(hkl)$, and the interplanar spacing, $d(hkl)$, are related via the atomic volume, Ω, as follows:

$$A(hkl)d(hkl) = \Omega \tag{1.43}$$

Based on this relationship, the most widely spaced planes correspond to the ones with the smallest planar unit-cell areas, i.e. the densest planes of the crystal lattice (also Tables 1.1 and 1.2).

As discussed in section 1.5.4, a necessary condition for two lattice planes to be commensurate is that their planar unit-cell areas are compatible, and hence satisfy eq. (1.12). Given eqs. (1.43) and (1.41), for the lattice planes in two different cubic crystal lattices (with lattice parameters a_1 and a_2, respectively) eq. (1.12) may be rewritten as follows:

$$\varepsilon_2^2 a_2^2(h_1^2 + k_1^2 + l_1^2)/\varepsilon_1^2 a_1^2(h_2^2 + k_2^2 + l_2^2) = m^2/n^2, \quad (\varepsilon_1, \varepsilon_2 = 0.5 \text{ or } 1) \tag{1.44}$$

In the case of GBs (for which $a_1 = a_2$), the ratio of the sum of the squares of the Miller indices hence has to be a ratio of squares of integers. The lattice planes with the smallest unit cells which are then compatible with the (111), (001), and (011) planes are listed in Table 1.3. These are the only relatively low-index combinations of planes forming commensurate GB interfaces with one of the three densest planes on one side. All other combinations have to form aperiodic or quasiperiodic structures [32].

Finally, we mention that the validity of eq. (1.43) is not limited to cubic lattices, as readily seen from eq. (1.39). The unit-cell area is generally given by the vector $[c_1 \times c_2]$ which is parallel to $\hat{n}$ (Fig. 1.26(a)). According to eq. (1.39), the unit-cell volume is the dot product of the vector c_3 and the area vector $[c_1 \times c_2]$. Since the latter is parallel to $\hat{n}$ (Fig. 1.26(a)) and since the projection of c_3 onto $\hat{n}$ is identical to the interplanar spacing, $|d|$, eq. (1.43) is reproduced.

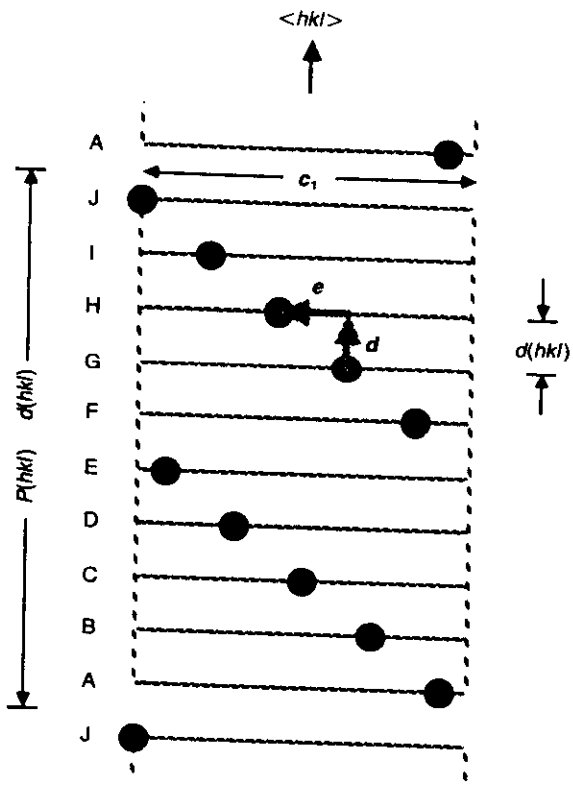

Fig. 1.28 Unit stack of lattice planes, labeled ... |AB ... IJ| ... , in a direction with $P(hkl) = 10$ planes in the stacking period (such as for the (210) plane in the fcc lattice; see Table 1.1). Illustrated is the constant in-plane translation, e, with the vector d allowing one to proceed from one plane to the nearest one (schematic).

1.7.2 Stacking inversion by rotation

A basic property of all lattices with inversion symmetry, particularly all Bravais lattices, is that the stacking sequence in a particular (rational) direction, $\langle hkl \rangle$, may be inverted by a 180° rotation about the plane normal $\langle hkl \rangle$. This property

Table 1.3 Cubic la
(see eq. 1.44) for

No.	$h_2k_2l_2$
1	(111)
2	(111)
3	(111)
4	(111)
5	(111)
6	(111)
7	(111)
8	(111)

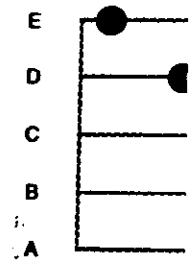

Fig. 1.29 Inversion
normal. (a) Before r

is illustrated in
thetical) five-pl
in Fig. 1.29(a)
$r = e + d$, w
1.28), between
the stack. A l
mal, $\langle hkl \rangle$, tra
$(-e_x, -e_y, d)$. I
symmetry a latt
one at r'; the v
therefore repres

So far we ha
center for the 1
$\langle hkl \rangle$, which
Obviously, for
lattice point in
(such as the C

Table 1.3 Cubic lattice planes with the smallest unit cells which are commensurate with the (111), (001) and (011) planes, respectively (see eq. 1.44 for $a_1 = a_2$ and $\alpha_1 = \alpha_2$)

No.	$h_2k_2l_2$	$h_1k_1l_1$	m^2/n^2	$(h_2k_2l_2)$	$(h_1k_1l_1)$	m^2/n^2	$(h_2k_2l_2)$	$(h_1k_1l_1)$	m^2/n^2
1	111	111	1	(001)	(001)	1	(011)	(011)	1
2	111	115	9	(001)	(221)	9	(011)	(114)	9
3	111	157	25	(001)	(430)	25	(011)	(071)	25
4	111	1511	49	(001)	(236)	49	(011)	(345)	25
5	111	11111	81	(001)	(148)	81	(011)	(149)	49
6	111	5713	81	(001)	(447)	81	(011)	(358)	49
7	111	1119	121	(001)	(667)	121	(011)	(4511)	81
8	111	5717	121	(001)	(269)	121	(011)	(778)	81

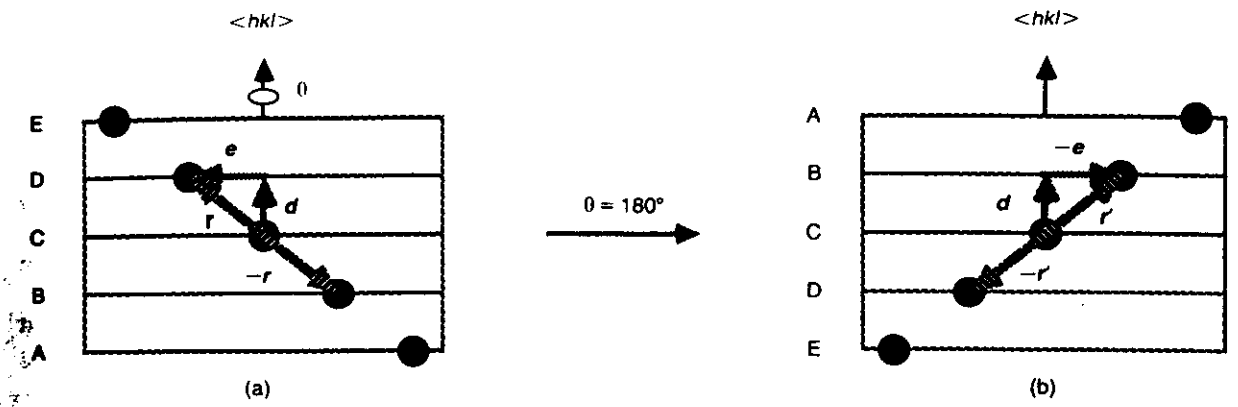

Fig. 1.29 Inversion of a (hypothetical) five-plane ideal-crystal stack of lattice planes, A–E, by a 180° twist rotation about the plane normal. (a) Before rotation; (b) after 180° rotation and application of inversion-symmetry operation (schematic).

is illustrated in Fig. 1.29 for the case of a (hypothetical) five-plane stacking period. The vector $\boldsymbol{r}$ in Fig. 1.29(a) represents the translation vector, $\boldsymbol{r} = \boldsymbol{e} + \boldsymbol{d}$, with components (e_x, e_y, d) (Fig. 1.28), between atoms in neighboring planes of the stack. A 180° rotation about the plane normal, $\langle hkl \rangle$, transforms $\boldsymbol{r}$ into $\boldsymbol{r}' = -\boldsymbol{e} + \boldsymbol{d} = (-e_x, -e_y, d)$. However, in a lattice with inversion symmetry a lattice point is found at $-\boldsymbol{r}'$ if there is one at $\boldsymbol{r}'$; the vector $-\boldsymbol{r}' = \boldsymbol{e} - \boldsymbol{d} = (e_x, e_y, -d)$ therefore represents a lattice point as well.

So far we have not elaborated on the rotation center for the 180° rotation about the plane normal, $\langle hkl \rangle$, which inverts the stacking sequence. Obviously, for a direction with an odd period, any lattice point in the central plane of the unit stack (such as the C plane in Fig. 1.29(a)) represents a possible rotation center. By contrast, for a direction with an even period, any half-way point between lattice sites in symmetrically related planes may serve as rotation center.

If the rotation axis for the unit-stack inversion has m-fold rotation symmetry, inversion is also achieved for the corresponding twist angles of $\theta = 180°/m \pm k\,360°/m$ ($k = 1, 2, \ldots, m - 1$). Thus, although each individual (111) plane in a cubic crystal contains a six-fold rotation axis, the staggered three-plane $\langle 111 \rangle$ unit stack only has three-fold symmetry ($m = 3$) because the center for this inversion rotation differs from that of the six-fold rotation symmetry. For similar reasons, $m = 2$ for a two-plane $\langle 100 \rangle$ unit stack, although individual (100) planes have four-fold rotation symmetry.

The property that in a crystal lattice with

inversion symmetry the stacking sequence may be inverted by a 180° rotation about the plane normal has important consequences for the atomic-level geometry of GBs. As illustrated further in section 1.8 below, it is responsible for the fact that in such crystal lattices (i) all symmetrical-tilt boundaries represent special 180° twist boundaries (section 1.6.1); (ii) asymmetrical-tilt boundaries (ATGBs) form a special subset of general (or asymmetrical-twist) boundaries; and (iii) for every asymmetrical combination of lattice planes, there are two distinct ATGB configurations (obtained for $\theta = 0°$ and 180°, respectively) which differ merely by the inversion of the stacking in one half relative to the other.

1.7.3 Example: stacking faults, free surfaces and symmetrical-tilt GBs in cubic crystals

In section 1.6 we described three interface systems which share the common property of having only two macroscopic DOFs, namely STGBs, stacking faults, and free surfaces. From the preceding discussion it is clear that they also share some important geometrical features. Most importantly, these three systems have identical planar unit-cell dimensions and areas (Figs. 1.30(b)–(d)), and their planar unit cell projected onto the interface plane is identical to that of the perfect crystal on the same plane, sketched in Fig. 1.30(a). Also, a tilt axis and a tilt angle may be formally assigned to all three, although in the case of stacking faults this terminology is not commonly used, while in the case of the surfaces the **tilt** axis is usually referred to as the **pole** axis.

Because a stacking fault differs from the STGB on the same plane only by the inversion of the stacking sequence in the latter (Figs. 1.30(b) and (c)), but is otherwise so similar to the STGB configuration, one might expect their physical properties to be rather similar also. In fact, based on their close geometrical relationship, one would expect that STGBs have a lot more in common with stacking faults than with GBs; this is contrasted by the common practice of viewing STGBs as high-angle GBs. Hence, rather than referring to these simple planar defects as **grain boundaries**, it might be more illustrative to call them **'inverted'** or **'tilted' stacking faults**. This would merely require a broadening of the definition of a stacking fault to include not only translations parallel to the fault plane but also a possible inversion of the stacking sequence at the plane of the defect.

As a consequence of having the smallest planar

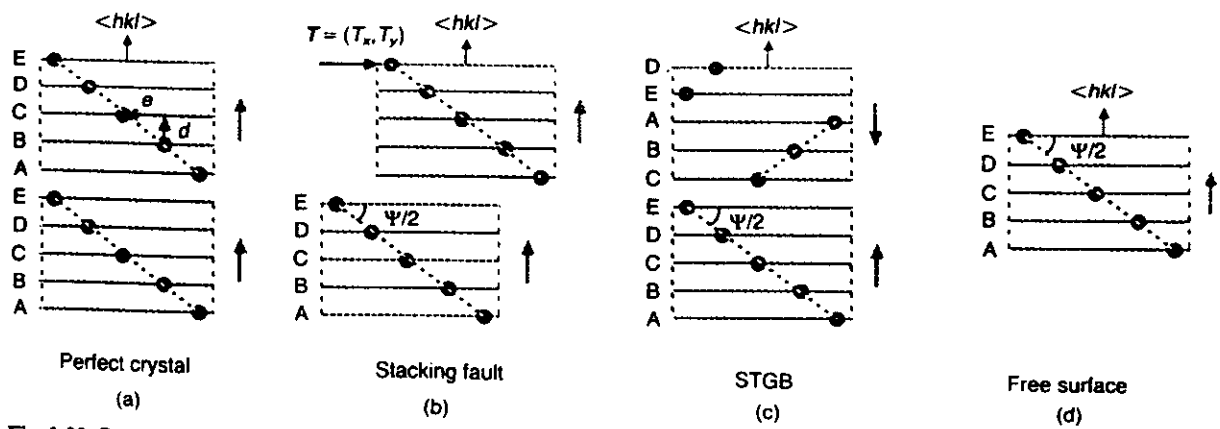

Fig. 1.30 Comparison of the atomic-level geometry of the simplest three interface systems in (b)–(d) with a perfect crystal in (a) (see also Fig. 1.1). Most importantly, the four systems sketched here have identical planar unit-cell dimensions and areas; this unit cell is the smallest possible for any atom arrangement involving this particular lattice plane, with a $\langle hkl \rangle$ normal. The shaded arrows indicate the direction of planar stacking. We note that Figs. 1.17 and 1.30 may be directly superimposed, illustrating the considerable similarity among these three systems and with the perfect crystal.

unit cell of any planar defect on a particular plane, the energies of stacking faults and STGBs are extremely sensitive functions of translations parallel to the interface, with a consequently large resistance towards shear parallel to the plane of the defect. This extreme sensitivity towards translations has been shown to be the cause for the appearance of energy cusps for symmetrical GBs whenever the STGB configuration on a particular plane is approached (i.e. as $\theta \rightarrow 180^{\circ}$; Fig. 1.23) [32, 33].

It appears that the close geometrical similarity between STGBs and free surfaces (Figs. 1.30(c) and (d)) has not always been recognized in the past, which might be one of the reasons why only relatively little is known about the work of adhesion of even these simplest of all GBs (section 1.6.5 and Fig. 1.24). From a conceptual viewpoint it appears that when an STGB is cleaved, thus creating two identical free surfaces, the **dislocations** in the GB are transformed into **steps** in the surfaces (Fig. 1.18), while the planar unit-cell dimensions of the interface are left unchanged. It would therefore seem that a better understanding of ideal-cleavage fracture requires an investigation of the relationship between steps in surfaces, on the one hand, and edge dislocations in STGBs on the other. The realization of the close geometrical similarity between these two simple interface systems might be of some aid in elucidating this complex problem [27].

1.8 GRAIN BOUNDARIES

Grain boundaries (GBs) represent ideal model systems for the investigation of the strictly geometrical aspects of structure–property correlations for the following three reasons. First, the complexity due to the myriad of possible choices of material combinations forming the interface is avoided, thus enabling a focus on the distinct roles played by the GB geometry, on the one hand, and the atomic structure on the other. Second, because GBs are bulk interfaces, dimensional interface parameters (such as the modulation wavelength in strained-layer superlattices, or the thickness of epitaxial layers) do not enter into the problem. Finally, the GB **energy** is thought to play a central role in various GB properties, such as impurity segregation, GB mobility and fracture, GB diffusion and cavitation, to name but a few. A better understanding of the correlation between the structure and the energy of GBs therefore promises to offer insights into more complex structure–property correlations as well. This correlation also represents a base line against which the effects of interfacial chemistry can be probed.

Although GBs probably represent the best-studied type of all interface systems, relatively little knowledge acquired on their physical behavior has filtered into other areas of interface research. It appears that one reason responsible for this unfortunate situation is related to the terminology used to describe their geometry, which differs fundamentally from that commonly used to describe, for example, epitaxial and thin-film interfaces. In this section we will review some of the GB 'jargon' within the framework of the concepts described in sections 1.6 and 1.7; a good understanding of these sections is therefore helpful. By defining these important defects in the context of the unified interface terminology, we hope to further elucidate the geometrical features in common to all interface systems and materials.

1.8.1 Coincident-site lattice description ('CSL-misorientation scheme')

As is well known, whether a GB is of a pure tilt, twist or mixed type, whether it is symmetrical or asymmetrical, or whether it is of a low- or high-angle type is fully determined by the choice of the five macroscopic DOFs of the interface. While, so far, we have reviewed one definition of these five geometrical variables (the interface-plane scheme in section 1.6.1), much of the terminology used to describe the geometry of GBs is based on the concept of the **coincident-site lattice** (**CSL**). By contrast with the interface-plane scheme in eq. (1.20), the CSL description of GBs focuses on the misorientation between the two grains, rather than on the plane of the defect. Also, because of the requirement that a superlattice must exist in common to the two halves of a bicrystal (at least

prior to allowing for rigid-body translations associated with the three translational DOFs), the CSL terminology is limited to commensurate interfaces and is hence not usually applied to interfaces other than GBs, rendering a comparison of properties with those of other interfacial systems virtually impossible.

In this and the following section, we will discuss two CSL-based, and often intermixed, definitions of the five macroscopic DOFs (the **CSL-misorientation** and **tilt-inclination schemes**). We then explore the relationship between the three rather different definitions of the macroscopic DOFs of crystalline interfaces discussed in this chapter by investigating the mathematical connections between them.

Within the framework of the CSL description of GBs [16–19], three of the five macroscopic DOFs are identified with the CSL misorientation, and only the remaining two DOFs are assigned to the GB plane. (Although redundant, the inverse volume density of CSL sites, Σ, is usually added as a sixth parameter.) The misorientation between the crystal lattices associated with the two grains may be characterized by the rotation matrix $\mathbf{R}(\hat{n}_{CSL}, \phi_{CSL})$, with $\hat{n}_{CSL}$ and ϕ_{CSL} denoting the CSL rotation axis and angle, respectively (representing three DOFs). The five DOFs are then defined as follows:

$$\{\text{DOFs}\} = \{\hat{n}_{CSL}, \phi_{CSL}, \hat{n}_1\} \quad \text{('CSL-misorientation scheme')} \tag{1.45}$$

where, as in the interface-plane scheme in eq. (1.20), $\hat{n}_1$ represents the GB-plane normal in either of the two halves of the bicrystal (here chosen to be semicrystal 1). Both $\hat{n}_{CSL}$ and $\hat{n}_1$ are expressed in a space-fixed principal crystallographic coordinate system, such as the (x, y, z) system in Fig. 1.15(a). Because of its focus on the CSL misorientation between the two halves of the bicrystal, the definition in eq. (1.45) will be referred to as the 'CSL-misorientation scheme'. Given these five variables, the GB-plane normal in the second crystal, $\hat{n}_2$, is determined by [18, 21]

$$\hat{n}_2 = \mathbf{R}(\hat{n}_{CSL}, \phi_{CSL})\hat{n}_1 \tag{1.46a}$$

Similarly, the inverse density of CSL sites, Σ, is governed completely by the three DOFs in the CSL rotation, i.e. $\Sigma = \Sigma(\mathbf{R}(\hat{n}_{CSL}, \phi_{CSL}))$.

We note that, prior to the CSL rotation, the two interpenetrating crystal lattices need not necessarily be identical. If they are identical, the CSL rotation results in the formation of a CSL for a **grain boundary**. Obviously, a superlattice in common to the two crystal lattices can not be formed unless the two are commensurate in all three dimensions (analogous to the concept of two-dimensional commensurability defined in section 1.5).

More explicitly, if one defines $\hat{n}_{CSL}$ by its direction cosines, say, in the (x, y, z) coordinate system in Fig. 1.15(a), according to $\hat{n}_{CSL} = (u, v, w)$ (with $u^2 + v^2 + w^2 = 1$), and if one uses the abbreviations $\cos\phi_{CSL} = c$, $\sin\phi_{CSL} = s$, the rotation matrix may be written as follows [18]:

$$\begin{aligned}\mathbf{R}(\hat{n}_{CSL}, \phi_{CSL}) &= \mathbf{R}(u, v, w, c, s) \\ &= (1-c)\begin{pmatrix} u^2 & uv & uw \\ uv & v^2 & vw \\ uw & vw & w^2 \end{pmatrix} \\ &\quad + \begin{pmatrix} c & -ws & vs \\ ws & c & -us \\ -vs & us & c \end{pmatrix}\end{aligned} \tag{1.47}$$

A pure **tilt** boundary is defined by the condition that $\hat{n}_{CSL}$ be perpendicular to $\hat{n}_1$ in eq. (1.45), while a pure **twist** boundary is obtained whenever $\hat{n}_{CSL}$ is parallel to $\hat{n}_1$. As illustrated in Fig. 1.15, the total (CSL) misorientation between the two halves of the bicrystal may be viewed as consisting of a tilt rotation (Fig. 1.15(b)) followed by a twist rotation (Fig. 1.15(c)). Using the perfect crystal in Fig. 1.15(a) as starting point, the purpose of the tilt rotation is to align $\hat{n}_1$ and $\hat{n}_2$, thus defining the common GB-plane normal in Fig. 1.15(b). This rotation is followed by a twist rotation about this common normal, thus adding a twist component to the tilt component while forming a 'general' GB. The CSL rotation matrix, $\mathbf{R}(\hat{n}_{CSL}, \phi_{CSL})$, may therefore be decomposed into its tilt and twist components, $\mathbf{R}(\hat{n}_T, \psi)$ and $\mathbf{R}(\hat{n}_1, \theta)$, respectively (with the tilt and twist angles ψ and θ, respectively), according to [18]

$$\mathbf{R}(\hat{n}_{CSL}, \phi_{CSL}) = \mathbf{R}(\hat{n}_1, \theta)\,\mathbf{R}(\hat{n}_T, \psi) \tag{1.48}$$

Because rotations do not generally commute, interchanging the sequence of the tilt and twist rotations leads to a different final state, as is also evident from the matrix equation (1.48).

Finally, since the twist rotation does not alter the common GB normal, the CSL rotation in eq. (1.46a) may be replaced by its tilt component, and

$$\hat{n}_2 = \mathbf{R}(\hat{n}_T, \psi)\,\hat{n}_1 \tag{1.46b}$$

Equation (1.46b) expresses the fact that the **plane** of a general GB is fully determined by its tilt component; conversely, the tilt component of a general GB is determined fully by the GB plane (section 1.6.1 and eqs. (1.21) and (1.22)).

A problem with the above CSL-based terminology is that within its framework the underlying number of macroscopic DOFs of a given GB is not always readily apparent. The three rotation matrices defined above involve a total of **nine** geometrical variables in $\hat{n}_{CSL}$, ϕ_{CSL}, $\hat{n}_T$, ψ, $\hat{n}_1$ and θ for an overall misorientation which is characterized by only the **three** DOFs in $\hat{n}_{CSL}$ and ϕ_{CSL}. Six relationships must therefore exist among these variables. While eq. (1.48) represents three of these, the remaining three may be obtained by expressing $\hat{n}_{CSL}$ and ϕ_{CSL} directly in terms of the twist and tilt axes and angles, according to [21]

$$\begin{aligned}\hat{n}_{CSL} = \beta^{-1}\{&[(1 + \cos\theta)(1 - \cos\psi)]^{\frac{1}{2}}\,\hat{n}_T \\ &+ [(1 - \cos\theta)(1 + \cos\psi)]^{\frac{1}{2}}\,\hat{n}_1 \\ &+ [(1 - \cos\theta)(1 + \cos\psi)]^{\frac{1}{2}}\,[\hat{n}_T \times \hat{n}_1]\}\end{aligned} \tag{1.49}$$

and

$$\cos\phi_{CSL} = (1 + \cos\theta)(1 + \cos\psi)/2 - 1 \tag{1.50}$$

where

$$\beta = (3 - \cos\theta - \cos\psi - \cos\theta\cos\psi)^{\frac{1}{2}} \tag{1.51}$$

While the (unit-) vector equation (1.49) connecting the three rotation axes represents two of the three additional relationships, the remaining one is eq. (1.50) which relates the three rotation angles to one another.

As is readily verified, eqs. (1.49)–(1.51) pass several trivial tests [21]:

(1) for $\psi \equiv 0$, $\hat{n}_{CSL} \equiv \hat{n}_1$ with $\phi_{CSL} \equiv \theta$ (pure twist);
(2) for $\theta \equiv 0$, $\hat{n}_{CSL} \equiv \hat{n}_T$ with $\phi_{CSL} \equiv \psi$ (pure tilt);
(3) for $\phi_{CSL} \equiv 0$ (no CSL misorientation), eq. (1.50) yields $\theta = \psi \equiv 0$; however, $\hat{n}_{CLS}$ becomes singular in this case because a rotation axis cannot be defined for this singularity of the CSL rotation.

Together with eqs. (1.21) and (1.22), the above expressions may be used to make the connection between the interface-plane and the CSL-misorientation schemes for the characterization of the same interface. For example, starting from the interface-plane definition of the five DOFs in eq. (1.20), the expressions (1.21) and (1.22) may be used to determine the tilt component, $(\hat{n}_T, \psi)$, of the interface. With its twist component, $(\hat{n}_1, \theta)$, apparent from the outset in eq. (1.20), eqs. (1.49) and (1.50) may then be used to determine the CSL misorientation, $(\hat{n}_{CSL}, \phi_{CSL})$. Conversely, starting from the CSL-based definition of the five DOFs in eq. (1.45), the expression (1.46a) may be used to determine $\hat{n}_2$. Given $\hat{n}_1$ and $\hat{n}_2$, the tilt component of the CSL boundary is simply given by eqs. (1.21) and (1.22); using this information in eq. (1.50), one may determine the twist angle θ needed in eq. (1.20).

The above CSL-based expressions describe rather elegantly, in terms of linear algebra, how a commensurate interface can be formed by a single rotation of two infinitely large, interpenetrating crystal lattices with respect to one another. From a practical viewpoint it is important to recognize that the CSL rotation axis and angle, as well as the GB-plane normal, are defined in the **unrotated** principal coordinate system associated with one of the two semicrystals (Fig. 1.15(a)). This makes it rather tedious at times to characterize a GB experimentally, starting from the already **rotated** positions of the atoms at hand. By contrast, the interface-plane scheme in eq. (1.20) focuses on the actual interface geometry at hand rather than on how this particular geometry may be thought of as

having been generated by a single rotation of two interpenetrating crystal lattices with respect to one another.

Finally, we mention that the CSL-based terminology is further complicated by the concept of the boundary-plane **inclination**, α, which introduces a fourth rotation to the three already defined above (for details section 1.8.2). The number of CSL-based geometrical variables often used interchangeably to describe a single bicrystalline GB (with at most five DOFs) thus increases to a total of 13, including $\hat{n}_{CSL}$, ϕ_{CSL}, $\hat{n}_T$, ψ, $\hat{n}_1$, θ, $\hat{n}_2$, α, and Σ. This somewhat startling number emphasizes the importance in GB studies of knowing the correct number of independent degrees of freedom of the system, particularly when structure–property correlations are being investigated. As a practical matter, it might help in any such investigation to adhere strictly to any one of the three choices of DOFs given in eqs. (1.20), (1.45), and (1.54) below, from which all the others can, in principle, be derived, via expressions such as the ones given here and in section 1.6.1.

1.8.2 Asymmetrical GBs

In spite of indications for the preponderance of **asymmetrical** GBs in polycrystalline materials [34], our current understanding of structure–property interrelations is based largely on the investigation of symmetrical boundaries. With the development of high-resolution transmission-electron-microscopy methods (HREM) in 'edge-on' studies of tilt GBs, much atomic-level information concerning the orientation of the GB plane has become available during recent years. Much of this work shows that in both metals [35–37] and ceramic materials [38, 39] asymmetrical combinations of lattice planes and faceting occur rather commonly.

Two types of asymmetrical GBs are usually distinguished; these are known as **asymmetrical-tilt** boundaries (ATGBs) and **general** boundaries (Fig. 1.31). In this section we will attempt to describe their geometry within the framework of both the interface-plane scheme and the CSL-based terminology.

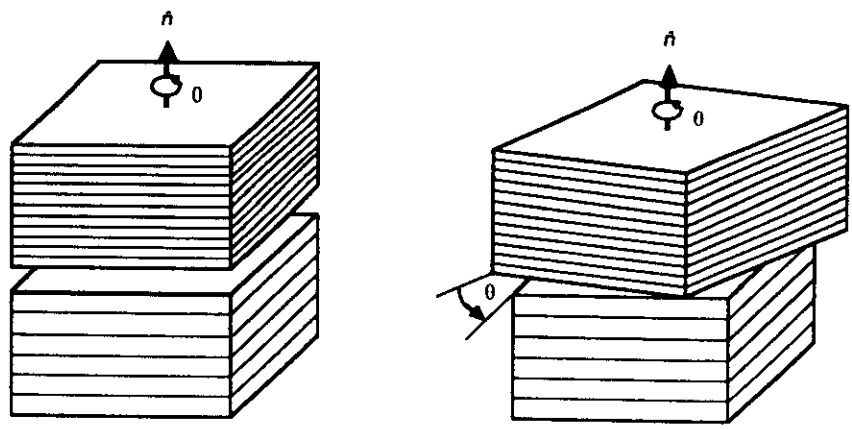

Fig. 1.31 Distinction between **asymmetrical-tilt** and **asymmetrical-twist** grain boundaries. While an **asymmetrical-tilt** boundary (ATGB) is obtained for $\theta = 0°$ or 180°, for some arbitrary twist angle, θ, an asymmetrical-twist or **general** GB, sketched in (b), is obtained. The alignment of the lattice planes is analogous to that in Figs. 1.15(b) and (c).

Geometry of general GBs

Applying the interface-plane based nomenclature in eq. (1.20) to asymmetrical GBs, one can readily distinguish the tilt and twist components of the interface. Its tilt component, and hence its edge-dislocation content, is completely given by the two sets of lattice planes forming the interface, i.e. by the GB **plane** (Fig. 1.31(a) and eqs. (1.21) and (1.22)). The twist angle θ introduces in addition a twist component, i.e. screw dislocations, into the boundary (Fig. 1.31(b)). The values of θ corresponding to the beginning and end of the twist-misorientation range (i.e. $\theta = 0°$ and 180°; see Fig. 1.31(a)) are most appropriately chosen such that the GB has no twist component, i.e. that its structure contains edge dislocations only. The interface thus obtained for (eq. (1.20))

$$\{\text{DOFs}\} = \{\hat{n}_1, \hat{n}_2, \theta = 0° \text{ or } \theta = 180°\} \quad (1.52)$$

is therefore of a pure tilt type and is commonly referred to as an **asymmetrical-tilt boundary** (ATGB). Because of the absence of screw dislocations (which, similar to the case of low-angle twist boundaries, would increase the planar unit cell area of the GB), this interface has the smallest possible planar unit cell of any asymmetrical GB formed by a given set of lattice planes. Since the value of θ is fixed, an ATGB has only four DOFs, by contrast with a **general** boundary which also has a twist component and, hence, five DOFs (Fig. 1.31(b)).

To relate this GB-plane-based picture of an asymmetrical boundary to the conventional CSL-based picture, Fig. 1.32 offers a different view of how the ATGB structure in Fig. 1.31(a) may be thought of as having been generated by a pure tilt rotation. The orientation of the tilt axis, $\hat{n}_T$, perpendicular to the GB-plane normal, $\hat{n}$, is illustrated in Fig. 1.32(a). Adding the tilt angle, ψ, to the two unit vectors, $\hat{n}_T$ and $\hat{n}$, according to Fig. 1.32(a) and eq. (1.45), it appears that five geometrical variables are necessary to specify an asymmetrical-tilt boundary, because now

$$\{\text{DOFs}\} = \{\hat{n}_T, \psi, \hat{n}\} \quad (1.53)$$

However, since $\hat{n}_T$ and ψ are fully governed by $\hat{n}_1$ and $\hat{n}_2$ (see eqs. (1.21) and (1.22)), ATGBs have only four DOFs; therefore they are a subset of asymmetrical-**twist** boundaries.

In the conventional 'edge-on' view (down the tilt axis) of an ATGB, the atoms in densest directions perpendicular to the tilt axis are usually connected (Fig. 1.32(c)). In Fig. 1.32(b) the same atoms are, instead, connected by lines parallel to the GB, making clear the connection with the ATGB configuration in Fig. 1.31(a). Finally, Fig. 1.32(d) provides a view onto the GB plane, showing the

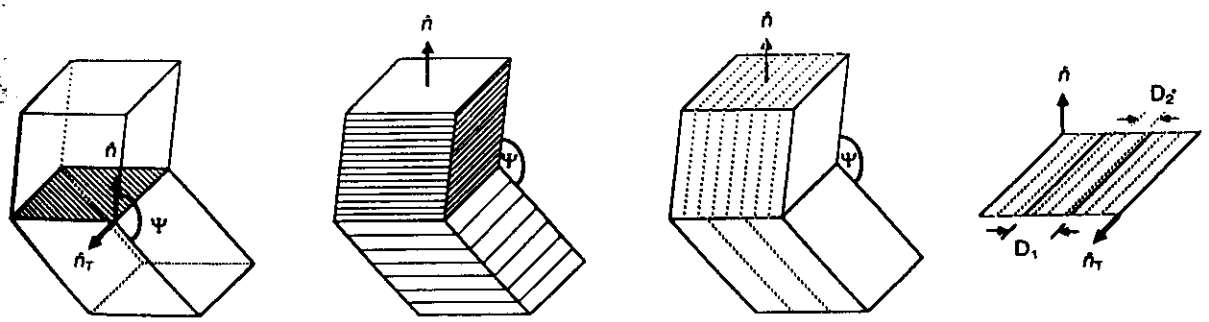

Fig. 1.32 Conventional CSL generation of an asymmetrical-tilt boundary by a pure tilt rotation (a). In the edge-on view in (c), the atoms in the densest directions perpendicular to the tilt axis are connected. To demonstrate the connection with the ATGB configuration in Fig. 1.31(a), in (b) the same atoms are, instead, connected by lines parallel to the GB-plane. Finally, (d) provides a view onto the GB plane, showing the two sets of edge dislocations, with spacings D_1 and D_2; in the edge-on view in (c), these dislocations correspond to the (dashed) lattice planes terminating at the GB.

two sets of edge dislocations, with spacings D_1 and D_2; in the edge-on view in Fig. 1.32(c), these dislocations correspond to the (dashed) lattice planes terminating at the GB.

It is important to recognize that for the same combination of lattice planes forming the asymmetrical GB, two ATGB configurations are obtained. To illustrate this little recognized geometrical feature of ATGBs, in Fig. 1.33 we have chosen two hypothetical orientations, $\hat{n}_1$ and $\hat{n}_2$, with $P(\hat{n}_1) = P_1 = 3$ and $P(\hat{n}_2) = P_2 = 11$ planes in the repeat stacking period defined in section 1.7.1. For the purpose of this illustration, we also assume that the planar unit cells are commensurate such that, say, nine planar unit cells of crystal 2 (3×3) match a single unit cell of crystal 1; the unit-cell areas are hence related by $A_2/A_1 = \frac{1}{9}$ (Fig. 1.33). As discussed in section 1.7.2, in crystal lattices with inversion symmetry a $180°/m$ twist rotation (about the common GB-plane normal) leads to the inversion of the stacking sequence on one side of the interface with respect to the other. (Here m characterizes a possible rotation symmetry (for $m > 1$) in the planar unit cell of the GB; section 1.7.2.) In such a lattice the two ATGB configurations thus obtained for the twist angles of $\theta = 0°$ and $\theta = 180°/m$ differ merely by the inversion of the stacking sequence, while their unit-cell dimensions are identical (Fig. 1.33). Since only a relative rotation of the two halves is involved, starting from the ATGB in Fig. 1.33(a) the same ATGB configuration in (b) would have been obtained had the **lower** semicrystal been inverted (provided both crystal lattices have inversion symmetry). More generally, in a crystal lattice without inversion symmetry the two ATGB configurations

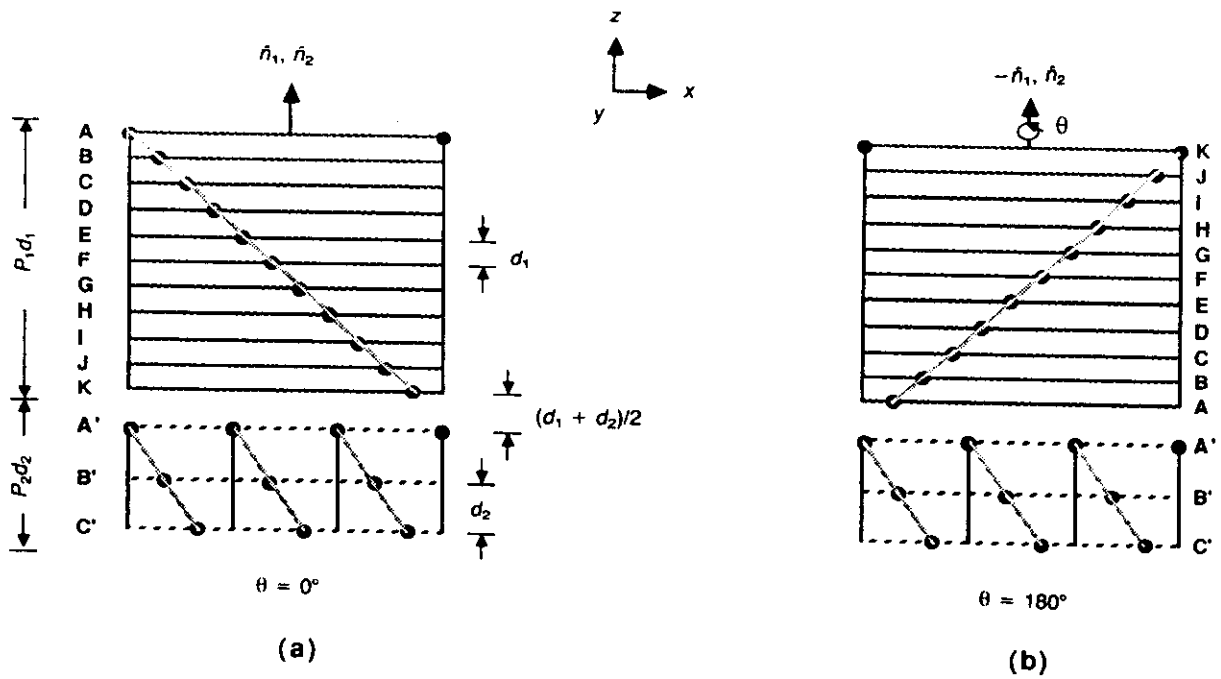

Fig. 1.33 Two **asymmetrical-tilt** configurations, with identical unit-cell dimensions but inverted stacking sequences in one with respect to the other, are obtained for $\theta = 0°$ and 180°, respectively. In the case shown, the upper crystal was inverted (i.e. turned upside down) by the twist rotation. Since only a **relative** rotation of the two halves is involved, the same ATGB configuration in (b) would have been obtained had the lower semicrystal been inverted (provided the crystal lattices have inversion symmetry). $d_\alpha = d(\hat{n}_\alpha)$ and $P\alpha = P(\hat{n}_\alpha)$ ($\alpha = 1, 2$) denote, respectively, the interplanar lattice spacings and stacking periods in the two halves. To preserve the perfect-crystal density, the effective interplanar spacing at the interface is given by the arithmetic average, $d_{\text{eff}} = (d_1 + d_2)/2$.

in Fig. 1.33(a) and (b) would differ also by the inversion of stacking at the interface; however, to achieve that inversion, one semicrystal has to be turned upside down with respect to the other, an operation not possible by a pure twist rotation.

In a few high-symmetry cases, the two ATGB configurations generally possible for a particular combination of lattice planes may be identical. For example, the (100) and (110) planes in the fcc and bcc lattices exhibit only a two-plane stacking period, . . . |AB|AB| . . . . The inversion of these planes by a 90° twist rotation (because $m = 2$; section 1.7.2) about ⟨100⟩ or ⟨110⟩, respectively, can be undone simply by a rigid-body translation parallel to the plane, thus restoring the original unrotated perfect crystal (Fig. 1.39 below). Hence, in asymmetrical GBs in fcc or bcc metals with a (100) or (110) plane on one side of the interface, the two ATGB configurations are identical. (To better visualize the effect of a twist rotation by 180°, one may simply think of its net effect being the turning upside down of one of the semi-crystals in Fig. 1.33(a).) Generally, an asymmetrical GB must be formed by two sets of lattice planes, each with more than two planes in the stacking period, for the two ATGB configurations to be different.

As already mentioned, the introduction of screw dislocations, in addition to the edge dislocations already present in the ATGB, obviously increases the planar unit-cell area of the interface. The two ATGBs obtained for a given combination of planes therefore represent the asymmetrical GBs with the smallest planar unit-cell area of all the GBs that can be formed by these lattice planes. From a strictly geometrical point of view, asymmetrical-twist boundaries may therefore be viewed as 'vicinals' to the two 'special' ATGBs obtained for a given combination of planes (section 1.6.4). Moreover, since the inversion of the stacking sequence preserves the planar unit-cell dimensions, the two ATGB configurations are unique geometrically in that they have identical planar unit-cell dimensions, with an area which is the smallest of all the GBs formed by the same combination of lattice planes. As illustrated in Chapter 3 of this volume [32], in both fcc and bcc metals this unique geometry translates into a particularly low energy of asymmetrical-tilt boundaries, giving rise to energy cusps and, hence, indeed 'special' properties of these two configurations at the endpoints of the twist-misorientation range. Most asymmetrical-twist boundaries are therefore 'vicinal' boundaries, in the sense defined in section 1.6.4.

We finally mention that the interface-plane-based view of asymmetrical GBs brings out naturally that (i) the tilt component of a general boundary is solely responsible for the asymmetry in the GB plane, (ii) ATGBs are a special subset, with four DOFs, of general boundaries, (iii) there are generally two ATGB configurations for every combination of lattice planes, and (iv) there is considerable resemblance of a general (or asymmetrical-twist boundary) with a symmetrical-twist boundary, in that both may be generated by a rotation about the GB-plane normal by some angle θ (compare Fig. 1.31(b) with Fig. 1.35(b)), introducing screw dislocations into the GB. As illustrated in Chapter 3 of this volume [32], the incorporation of this geometrical similarity between general and symmetrical GBs in the interface-plane-based definition of the macroscopic DOFs is of considerable aid in the investigation of their properties. Finally, since the interface-plane-based description of GBs is not limited to commensurate interfaces, it facilitates a direct comparison of GBs with other types of interface systems.

The concept of the GB-plane inclination ('tilt-inclination scheme')

One CSL-based description of asymmetrical GBs uses the concept of the inclination of the GB plane, thus adding a fourth rotation to the CSL-, tilt- and twist rotations already discussed in section 1.8.1. The related choice of macroscopic DOFs (referred to as the 'tilt inclination scheme') has the advantage that it closely resembles an experimental situation in which the tilt misorientation between two grains is fixed, while the GB plane may choose whatever inclination may lead to a particularly low GB energy. Such a situation is encountered, for example, when a tilt bicrystal is grown from two preoriented seeds [37].

It may be useful to describe the concept of the

GB-plane inclination in a somewhat unconventional manner. We start with the observation that the tilt component, $(\hat{n}_T, \psi)$, of a general GB is fully determined by the GB-plane normals, $\hat{n}_1$ and $\hat{n}_2$ (eqs. (1.21) and (1.22)). Hence, starting from the **three** variables in $\hat{n}_T$ and ψ, in order to fix the GB **plane**, a single additional parameter, α, is required; α is called the inclination angle. Therefore, by replacing $\hat{n}_1$ and $\hat{n}_2$ in eq. (1.20) by the tilt misorientation and inclination angle, the five DOFs may be defined as follows:

$$\{\text{DOFs}\} = \{\hat{n}_T, \psi, \alpha, \theta\} \quad \text{('tilt-inclination scheme')} \qquad (1.54)$$

The geometrical meaning of α is illustrated in Fig. 1.34(a) [37] for the case of pure (symmetrical and asymmetrical) **tilt** boundaries in cubic crystals (eqs. (1.52) and (1.53)). For a given fixed tilt misorientation, $(\hat{n}_T, \psi)$, **symmetrical** boundary-plane configurations are obtained for the angles $\alpha = \psi/2$ (labeled $STGB_1$) and $\alpha = \psi/2 + 90°$ (labeled $STGB_2$), respectively. The asymmetrical combinations of GB planes may conveniently be characterized by the inclination angle, α, with respect to the $STGB_1$ orientation (Fig. 1.34(a)). The two STGB configurations are then defined by $\alpha = 0°$ and $\alpha = 90°$, while for any other value of α an ATGB is obtained.

Figure 1.34(a) also illustrates that for every combination of $\hat{n}_T$ and ψ, at most two symmetrical, but infinitely many asymmetrical, GB-plane orientations are possible. (We should point out, however, that this is true only for a rational tilt axes in cubic crystals; for systems with less symmetry, a symmetrical configuration may not exist [37].)

A simple method for determining α is the following. Starting with the fixed tilt misorientation between two grains, the two STGBs are usually either well known (based on the value of Σ) or readily determined [19]; these define the angles $\alpha = 0°$ and $90°$. Given an ATGB in the same tilt bicrystal (i.e. with the same tilt axis and angle), $\cos\alpha$ is simply given by the dot product between corresponding STGB and ATGB plane normals in the same half of the bicrystal.

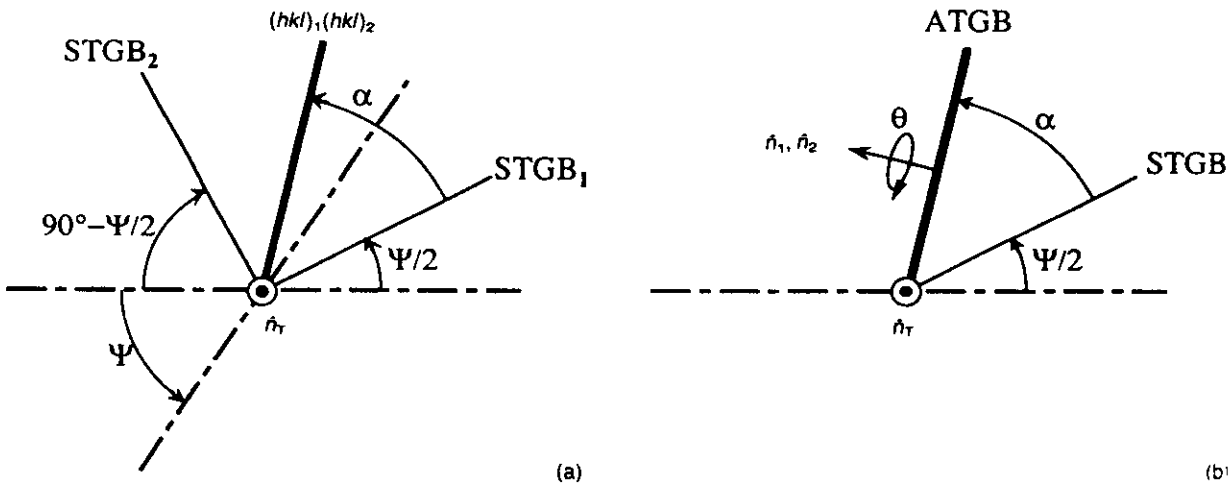

Fig. 1.34 (a) Definition of the two symmetrical-tilt configurations, $STGB_1$ and $STGB_2$, obtained for a given **tilt** misorientation, by the angle ψ, about the two-fold tilt axis with unit vector $\hat{n}_T$ (schematic) [37]. One of the mirror planes is indicated by dash-dotted lines for both crystal 1 and crystal 2. α is the inclination of the GB plane of some arbitrary **asymmetrical**-tilt configuration, combining $(h_1k_1l_1)$ and $(h_2k_2l_2)$ planes, measured with respect to $STGB_1$. The two **symmetrical** configurations correspond to inclinations $\alpha = \psi/2$ and $\alpha = \psi/2 + 90°$, respectively. (b) illustrates how a **twist** component may be introduced into the ATGB via a rotation, by the angle θ, about the common ATGB-plane normal, resulting in a **general** (or **asymmetrical-twist**) boundary, with both tilt and twist components. The meaning of θ is the same as in Figs. 1.15(c) and 1.31(b). (For further details, see Ref. [37]).

Within the tilt-inclination scheme, only one of the five DOFs (α) is actually assigned to the GB plane, and the determination of $\hat{n}_1$ and $\hat{n}_2$ represent a non-trivial undertaking. However, given the GB-plane normal on one side of the interface, $\hat{n}_1 = \hat{n}_1(\hat{n}_T, \psi, \alpha)$, the GB-plane orientation in the other half is determined by (eq. (1.46b))

$$\hat{n}_2 = \mathbf{R}(\hat{n}_T, \psi)\, \hat{n}_1(\hat{n}_T, \psi, \alpha) \tag{1.55}$$

To complete the definition of all five DOFs, a twist component ($\hat{n}_2$, θ), may be introduced into the ATGB in Fig. 1.34(a) via a rotation about the common GB-plane normal (Fig. 1.34(b)).

In the tilt-inclination scheme, a symmetrical interface is charactertized as follows:

$$\{\text{DOFs}\} = \{\hat{n}_T, \psi, \alpha = 0° \text{ or } \alpha = 90°, \theta\} \tag{1.56}$$

At first sight, eq. (1.56) appears to require the four variables in $\hat{n}_T$, ψ and θ for the characterization of an interface with only three DOFs. However, when the condition of symmetry, $\hat{n}_1 = \pm\hat{n}_2$ (eq. (1.25b)) is combined with eq. (1.55), a relationship between $\hat{n}_T$ and ψ is obtained, according to $\hat{n}_1 = \pm\mathbf{R}(\hat{n}_T, \psi)\, \hat{n}_1$, which permits ψ to be expressed as a function of $\hat{n}_T$, $\psi = \psi(\hat{n}_T)$, thus reducing the number of independent variables in eq. (1.56) to only three.

As already mentioned, the choice of macroscopic DOFs in eqs. (1.54) and (1.56) has the advantage that it sometimes resembles an experimental situation rather closely [37]. On the other hand, particularly when the twist component of an asymmetrical GB is varied systematically, it is more advantageous to use the interface-plane definition in eq. (1.20) and the concept of the asymmetrical-twist boundary. Hence, while formally one choice is as good as another, any particular choice will depend on the particular experimental situation.

Finally, as an example we consider the two ATGB configurations that can be formed when bringing together two fcc grains with (557) and (771) faces, respectively [37]. Within the interface-plane terminology, the two ATGB configurations at $\alpha = 0°$ and $\theta = 180°$ would be characterized by (eqs. (1.24) and (1.52))

$$\{\text{DOFs}\} = \{(557), (771), \theta = 0° \text{ or } \theta = 180°\} \tag{1.57}$$

and the fact that geometrically they differ merely by the inversion of the stacking sequence at the interface in one with respect to the other is obvious.

In the CSL-misorientation scheme, the two boundaries are characterized as follows (see also eqs. (1.45) and (1.53)) [37]:

$$\{\text{DOFs}\} = \{\langle 1\bar{1}0\rangle, 38.94° (557)\} \quad (\Sigma = 9) \tag{1.58a}$$

and

$$\{\text{DOFs}\} = \{\langle 1\bar{1}0\rangle, 50.58° (557)\} \quad (\Sigma = 11) \tag{1.58b}$$

where, for clarity, the related values of Σ are given in parentheses, indicating that the two ATGBs belong to different CSL systems. Given these definitions of their DOFs, the two GBs are readily identified as tilt boundaries (by contrast with general or pure twist boundaries, because $\hat{n}_{CSL} \perp \hat{n}_1$). However, it is neither obvious that the two GBs are asymmetrical tilts nor that they are such close relatives of one another geometrically. Also, identifying the GB plane in the other half of the bicrystal as the (771) plane requires one to solve eq. (1.46) with the rotation matrix (1.47).

Finally, in the tilt-inclination scheme, the two ATGBs are characterized by (eq. 1.56)

$$\{\text{DOFs}\} = \{\langle 1\bar{1}0\rangle, 38.94°, \alpha = 25.24°, \theta = 0°\} \quad (\Sigma = 9) \tag{1.59a}$$

and

$$\{\text{DOFs}\} = \{\langle 1\bar{1}0\rangle, 50.58°, \alpha = 70.53°, \theta = 0°\} \quad (\Sigma = 11) \tag{1.59b}$$

Here the underlying values of α were determined from the knowledge of the corresponding symmetrical configurations ((114)(11$\bar{4}$) and (221)(22$\bar{1}$) in the $\Sigma = 9$ system, and (113)(11$\bar{3}$) and (332)(33$\bar{2}$) for $\Sigma = 11$), from which $\cos\alpha$ is simply given by the dot product of corresponding symmetrical and asymmetrical planes in the same half of the bicrystal.

Again, as in eqs. (1.58a) and (b), the two GBs are readily identified as pure tilt GBs (from the fact

that $\theta = 0^\circ$), and their asymmetry follows directly from the fact that $\alpha \neq 0^\circ$ and $\alpha \neq 90^\circ$. However, starting from these parameters, the identification of the actual GB plane from a determination of $\hat{n}_1$ and $\hat{n}_2$, is non-trivial. Also, as in their CSL-misorientation description, their close geometrical similarity is not very obvious, particularly that (i) they are formed by the same set of lattice planes, and (ii) they have identical planar unit-cell dimensions.

1.8.3 Symmetrical GBs

In section 1.6.1 we defined an interface as **symmetrical** if $\hat{n}_1$ and $\hat{n}_2$ are related **linearly**, i.e. if $\hat{n}_2 = L(\hat{n}_1)$, such as $\hat{n}_2 = \pm\hat{n}_1$ (eqs. (1.25a) and (b)), thus reducing the number of DOFs from five to only three (eq. (1.26b)). $\theta = 0^\circ$ now corresponds to the perfect crystal while, for some arbitrary value of θ, a **symmetrical-twist** boundary (with three DOFs and no tilt component) is obtained (Fig. 1.35). This terminology emphasizes the similarity of Figs. 1.35(a) and (b) with the **asymmetrical-twist** boundary shown in Fig. 1.13(b).

As discussed in section 1.7.2, in crystals with inversion symmetry a twist rotation by $\theta = 180^\circ$ (i.e. about the GB-plane normal, $\hat{n}_2 = \hat{n}_1$) inverts the stacking sequence on one side of the interface with respect to the other while preserving the perfect-crystal planar unit-cell dimensions (Figs. 1.29 and 1.36). Consequently, the symmetrical-tilt boundary (STGB) thus obtained for $\theta = 180^\circ$ (and $\hat{n}_2 = \hat{n}_1$) is fully determined by only the two DOFs associated with the GB plane, $\hat{n}_2 = \hat{n}_1$, and eqs. (1.29a) and (1.29b) are obtained, i.e.

$$\{\text{DOFs}\} = \{\hat{n}_1, \hat{n}_1, \theta = 180^\circ\} \tag{1.60a}$$

In crystals without inversion symmetry, a 180° twist rotation inverts only the Bravais planes but not the basis, resulting in an incomplete inversion of the crystal planes. More generally, the STGB may then be viewed as a perfect crystal ($\theta = 0^\circ$) in which one half is turned upside down (i.e. $\hat{n}_2 = -\hat{n}_1$), according to

$$\{\text{DOFs}\} = \{\hat{n}_1, -\hat{n}_1, \theta = 0^\circ\} \tag{1.60b}$$

a characterization which does not require inversion symmetry.

As in the asymmetrical case, for any twist deviation from $\theta = 0^\circ$ and $\theta = 180^\circ$ in Figs. 1.36(a) and (b) the planar unit-cell area increases by introduction of screw dislocations. The crossed grid of screw dislocations is sketched schematically in Fig. 1.35(c). According to Frank's formula [10], the spacing, D, between these dislocations is given by

$$D = b/[2 \sin(\theta/2)] \approx b/\theta \tag{1.61}$$

where b is the Burgers vector. The linearization in eq. (1.61) is valid only for **low-angle** twist boundaries; for larger twist angles this approximation is not possible, thus defining the regime of **high-angle** twist boundaries. Given eq. (1.61), the

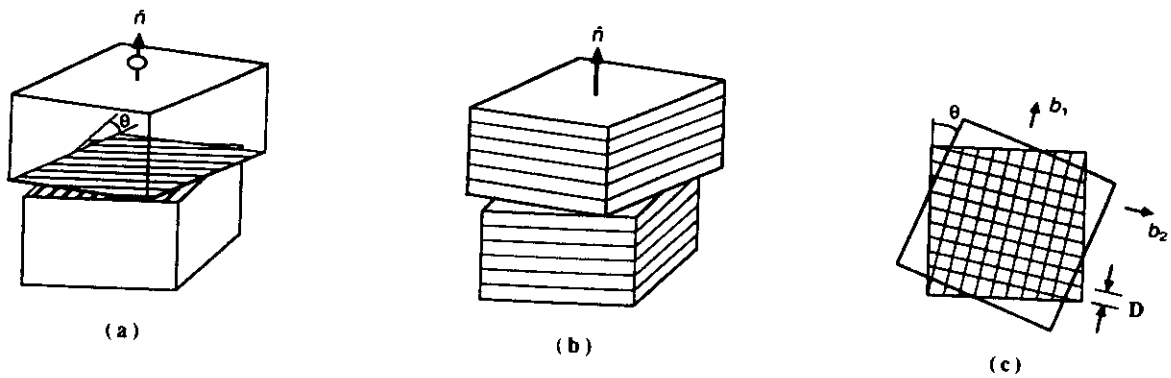

Fig. 1.35 (a) **Symmetrical-twist** boundary, obtained by rotation of two symmetrically aligned semicrystals ($\hat{n}_2 = \hat{n}_1$) about the common GB-plane normal, $\hat{n}$. The lattice planes shown in (b) illustrate the similarity with the **asymmetrical-twist** boundary, Fig. 1.31(b). (c) shows the crossed grid of screw dislocations characteristic for the structure of such an interface, with a spacing, D, given by eq. (1.61).

strain-field energy of the dislocation grid, with its well-known logarithmic cusp at $\theta = 0°$, was first derived by Read and Shockley [40] in terms of isotropic continuum-elasticity theory.

The increase in the planar unit-cell area of the GB as one rotates from the perfect-crystal or STGB configuration can be characterized by the inverse **planar** density of CSL sites, Γ. In contrast with Σ (which is the inverse **volume** density of CSL sites), the value of Γ indicates directly by how much the unit-cell area, $A(\theta)$, of a twist boundary exceeds that of the perfect-crystal or STGB configuration, $A(\theta = 0°) = A(\theta = 180°)$, on that plane because (eq. (1.28))

$$\begin{aligned} A(\theta) &\equiv \Gamma(\theta)\, A(\theta = 0°) \\ &= \Gamma(180° - \theta)\, A(\theta = 180°) \\ &\equiv A(180° - \theta) \end{aligned} \tag{1.62}$$

By definition,

$$\Gamma(\theta = 0°) = \Gamma(\theta = 180°) \equiv 1 \tag{1.63}$$

Equation (1.63) expresses the fact that the STGB and perfect-crystal configurations on a given plane are unique in that they share identical planar unit-cell dimensions, with an area which is the smallest possible for any planar defect on that plane (Fig. 1.36) [20]. In Chapter 3 of this volume [32] it will be shown that this unique geometry of the pure tilt configuration gives rise to a deep energy cusp at $\theta = 180°$ and hence to 'special' properties of STGBs. Most symmetrical-twist boundaries may therefore be viewed as 'vicinal' to either the STGB configuration on a given plane or to the perfect crystal; in the latter case, they are the well-known low-angle boundaries.

To relate the GB-plane-based picture of the STGB in Fig. 1.36 to the conventional CSL-based view, Fig. 1.37 shows the generation of the STGB structure in Fig. 1.36(b) by a pure tilt rotation. Figure 1.37(a) illustrates the orientation of the tilt axis, $\hat{n}_T$, perpendicular to the normal $\hat{n}$ of the GB; this normal is the same in the two semi-crystals. By contrast with the asymmetrical case in Fig. 1.32, the GB-plane normal and, therefore the tilt angle, Ψ, are fixed by the condition of symmetry, leaving only two independent DOFs in the CSL characterization of these simple planar defects by the five variables in (eqs. (1.45) and (1.53))

$$\{\text{DOFs}\} = \{\hat{n}_T, \Psi, \hat{n}\} \tag{1.64}$$

The fact that the CSL characterization of both STGBs and ATGBs is based equally on a set of five parameters (eqs. (1.63) and (1.64)) illustrates the difficulty in identifying a GB as either symmetrical or asymmetrical in this scheme.

In the conventional edge-on view of an STGB, the atom columns parallel to the tilt axis are usually connected (Fig. 1.37(c)). In Fig. 1.37(b) the same

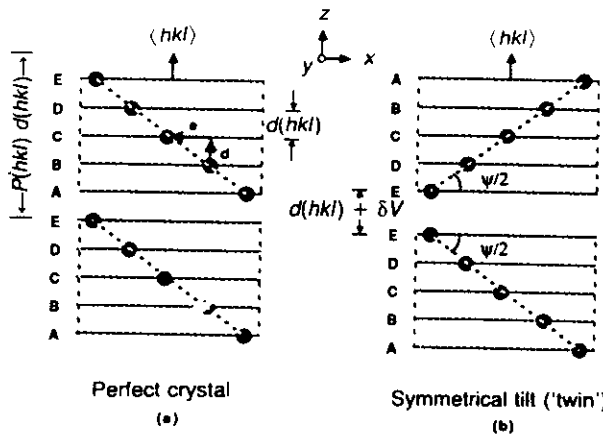

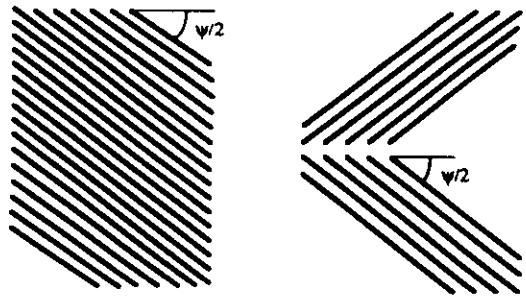

Fig. 1.36 In a perfect crystal with inversion symmetry, sketched schematically in (a) for a (hypothetical) five-plane stacking period, a rotation of one half about ⟨*hkl*⟩ generates the STGB configuration on the (*hkl*) plane sketched in (b). The latter is characterized by the familiar inversion of the stacking of the lattice planes at the interface ('twinning'), a feature in common to all STGBs. This inversion usually results in a volume expansion per unit GB area, δV. $d(hkl)$ and $P(hkl)$ are the interplanar spacing and repeat stacking period defined in section 1.7 (see eqs. (1.41) and (1.42)). The lower half represents an 'edge-on' view of the densest lattice directions, i.e. a view of atom columns parallel to the tilt axis. In this case, the tilt axis is parallel to the y direction; the tilt angle, ψ, is indicated.

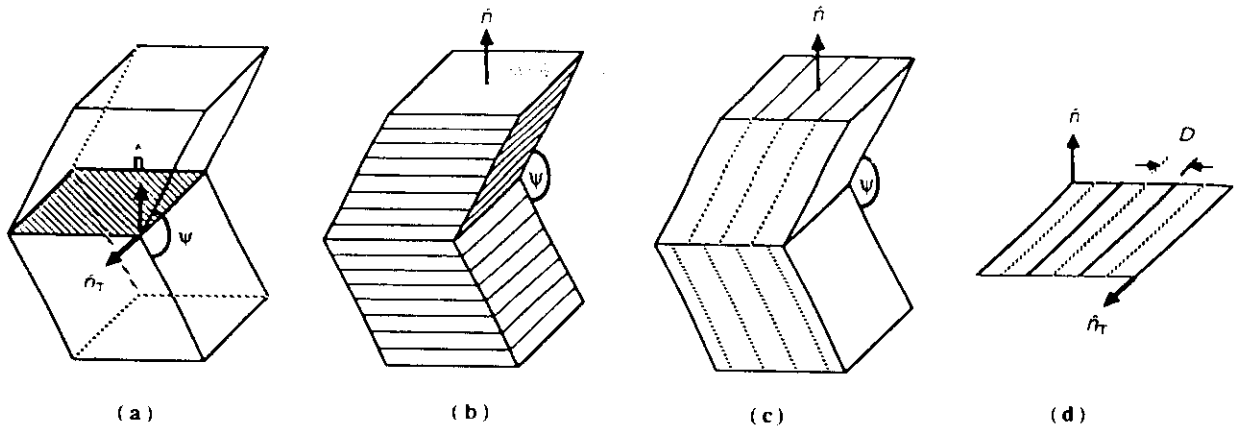

Fig. 1.37 Conventional CSL-based generation of the STGB structure in Fig. 1.36(b) by a pure tilt rotation. (a) Orientation of the tilt axis, $\hat{n}_T$, perpendicular to the normal, $\hat{n}$, of the GB; (b) lattice planes parallel to the GB illustrating the similarity with the asymmetrical-tilt boundary in Fig. 1.32(b). (c) shows the usual edge-on view down the tilt axis, in which the atom columns parallel to $\hat{n}_T$ are connected. (d) A view onto the GB plane shows two parallel sets of edge dislocations, with a spacing, D, given by eq. (1.61).

atoms are, instead, connected by lines parallel to the GB, making clear the connection with the STGB configuration in Fig. 1.36(b) and the ATGB in Fig. 1.32(b). Finally, the two sets of edge dislocations (one from each side of the interface) characteristic for this structure are sketched in the view onto the GB plane in Fig. 1.37(d). In contrast with the symmetrical-twist boundaries, the two sets of dislocations (identifiable, of course, only for small tilt angles) are parallel in this case. Interestingly, for strictly geometrical reasons in both cases the dislocation spacing is given by Frank's formula (1.61).

Finally, as an example we consider the characterization of the STGB configuration on the (332) plane of the fcc lattice, which belongs to the same $\Sigma = 11$ CSL system as one of the two ATGBs considered at the end of the preceding section. Within the interface-plane terminology, this boundary may be characterized in one of two ways. First, for $\hat{n}_2 = +\hat{n}_1$ the boundary would be characterized as a 180° twist boundary (which is permissible because the fcc lattice has inversion symmetry), according to (eqs. (1.24) and (1.60a))

$$\{\text{DOFs}\} = \{(332), (332), \theta = 180°\} \qquad (1.65a)$$

More generally, the boundary may be viewed as a perfect crystal ($\theta = 0°$) in which one half is turned upside down (i.e. $\hat{n}_2 = -\hat{n}_1$), according to (eq. (1.60b))

$$\{\text{DOFs}\} = \{(332), (33\bar{2}), \theta = 0°\} \qquad (1.65b)$$

a characterization which does not utilize the inversion symmetry. In writing the last expression, we have taken into account the fact discussed in section 1.8.4 below that in a cubic crystal an arbitrary combination of Miller indices $(-h, -k, -l)$, can always be reduced, by a sequence of 90° rotations about ⟨100⟩ which transforms the crystal into itself, for example to a form $(h, k, -l)$, $(h, -k, l)$, or $(-h, k, l)$.

In the CSL-misorientation scheme, the same boundary would be characterized in terms of five parameters as follows (eqs. (1.45) and (1.53)) [41]:

$$\{\text{DOFs}\} = \{(1\bar{1}0), 50.58° (332)\} (\Sigma = 11) \qquad (1.66)$$

where the value of Σ is included in parentheses. The GB is readily identified as a tilt boundary (because $\hat{n}_{CSL} \perp \hat{n}_1$). However, a comparison with the asymmetrical boundary in eq. (1.58b) (which belongs to the same $\Sigma = 11$ CSL system) demonstrates the difficulties in identifying the GB as symmetrical or asymmetrical.

Finally, in the tilt-inclination scheme the boundary is characterized by (eq. (1.54))

$$\{\text{DOFs}\} = \{(1\bar{1}0),\ 50.58^\circ,\ \alpha = 0^\circ,\ \theta = 0^\circ\}_{\Sigma = 11} \tag{1.67}$$

Again, as in the CSL scheme, the GB is readily identified as a pure tilt GB (from the fact that $\theta = 0^\circ$), and its symmetry follows directly from the fact that $\alpha = 0^\circ$. However, starting from these parameters, the identification of the crystallographic orientation of the GB plane is non-trivial.

We conclude this section by emphasizing an aspect of the conceptualization of symmetrical-tilt boundaries as special twist boundaries; this is of particular relevance to the computer simulation of GBs. In all GB simulations, in addition to the bicrystal at hand, a suitable undefected reference system containing the same number of atoms has to be considered in order to determine any excess quantity associated with the interface (such as the interface energy, thermal expansion, etc.). STGBs are conventionally generated by rotating two infinite, interpenetrating lattices with respect to one another, with the subsequent removal of corresponding atoms on both sides of the GB plane. This procedure gives rise to ambiguities regarding the undefected reference system with the same density and crystallographic orientation of the simulation cell as the bicrystal, rendering the determination of any excess quantities ambiguous.

1.8.4 Atomic-level geometry of symmetrical-tilt boundaries

From a strictly geometrical viewpoint, symmetrical-tilt boundaries are fascinating, yet little understood, objects. Since, like free surfaces and stacking faults, these simplest of all GBs have only two macroscopic DOFs (section 1.6.3), in this section we will discuss their atomic-level geometry in more detail.

As illustrated in Fig. 1.36(b), the atomic structure of an STBG is characterized by the familiar inversion of the stacking of the lattice planes at the interface ('twinning'), a feature in common to all STGBs. However, the directly inverted configuration in Fig. 1.36(b) is usually unstable because two identical lattice planes are right on top of one other. We refer to this translational state, in which the GB-plane is a mirror plane but not an atom plane, as the **unstable** twin. Two energetically more favorable translational states are shown in Fig. 1.38. In the **special** twin in Fig. 1.38(b), the GB is both a mirror plane and an atom plane. In the fcc lattice, for example, there is only one special-twin configuration, namely the STGB on the (111) plane. With the . . . |ABC| . . . stacking of (111) planes (with a three-plane stacking sequence, $P(111) = 3$; section 1.7.1 and Table 1.1), the directly inverted, unstable-twin configuration would be characterized by . . . |ABC|CBA| . . . , while in the optimal translational state the C plane is shared by the two halves, according to . . . |ABC|AB C BA|CBA| . . . .

On some arbitrary higher-index lattice plane, no physical reasons exist to favor the particular, high-symmetry special-twin configuration in Fig. 1.38(b). The STGB on such a plane usually exhibits some rather arbitrary rigid-body translation which is not generally a multiple of the in-plane stacking vector $\boldsymbol{e}$ in Fig. 1.28. We refer to such a translational state, sketched in Fig. 1.38(c), as a **general** twin, emphasizing the fact that its planar structure is still characterized by the inversion at the GB ('twin'), but that no special rigid-body translation exists.

Figure 1.39 illustrates that at least *three* planes are required in the repeat stacking sequence in the direction of $\hat{\boldsymbol{n}}$, $P(\hat{\boldsymbol{n}})$, for that plane to accommodate an STGB configuration. Consider, for example, the generation of an STGB on a set of lattice planes with only two planes in the repeat stacking sequences, such as the (100) and (110) planes in the fcc and bcc lattices. Starting with the perfect-crystal stacking . . . |AB|AB| . . . in Fig. 1.39(a), a 180° twist rotation yields the inverted configuration . . . |AB|BA| . . . (Fig. 1.39(b)). For reasons given above, this configuration of the STGB in which two planes are right on top of one another is usually unstable (Fig. 1.38(a)), giving rise to a rigid-body translation, $\boldsymbol{T} = (T_x, T_y)$, parallel to the interface. The obvious translation to minimize the mismatch across the interface is one in which B returns to A; such a translation, however, leads to

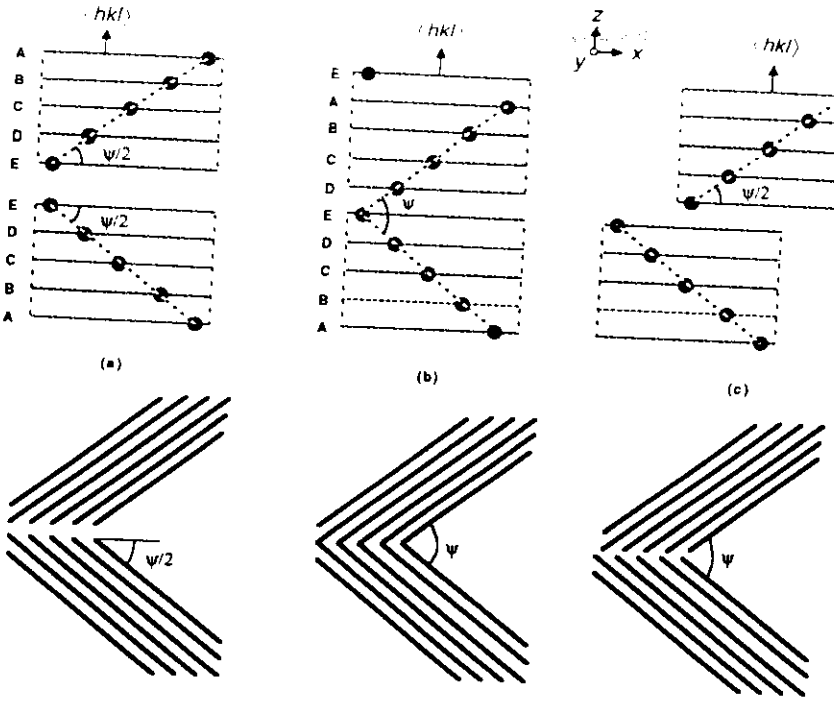

Fig. 1.38 Definition of three well-characterized translational states of an STGB. (a) Directly inverted (and usually unstable) configuration of Fig. 1.36(b) in which two identical (*hkl*) planes face each other across the interface. Notice that in this configuration the GB-plane is a twinning plane, but not an atom plane. (b) In the 'special' twin, the GB is both the twinning and an atom plane. (c) In most cases, an STGB exhibits some rather arbitrary rigid-body translation, referred to as a general twin, emphasizing the fact that its planar structure is still characterized by the inversion at the GB ('twin') but that no special rigid-body translation exists.

the re-establishment of the ideal-crystal stacking in the lower crystal, as illustrated in Fig. 1.39(c). Consequently, the 'STGB' on a set of lattice planes with two or only one plane in the repeat stacking sequence is identical to the ideal crystal.

With three planes in the repeat stacking sequence, the lowest-index plane in the fcc lattice which can actually accommodate an STGB is the (111) plane. Because of the three-fold symmetry axis of a unit stack of (111) planes discussed in section 1.7.2, a rotation by 60° ± k*120° ($k = 0, 1, 2, \ldots$) about the ⟨111⟩ normal produces the well-known (111) twin boundary sketched in Fig. 1.40. (In the GB community, this geometrically most special of all STGBs in the fcc lattice is commonly known as the **coherent twin**; however, because in section 1.6.3 the concept of coherency was defined in a different sense, here we try to avoid this term.) All other STGBs in the fcc lattice involve at least a six-plane repeat stacking sequence (Table 1.1), and no other STGB has been observed to exist in the 'special-twin' configuration (in which the GB plane is a mirror plane).

For a more quantitative discussion of the geometry of STGBs, we now turn to cubic crystals in which all relevant geometrical parameters may be expressed explicitly in terms of the Miller indices, (h, k, l), associated with the GB plane [20].

Formally, according to eqs. (1.21) and (1.22), the interface characterized by eq. (1.60) has a vanishing tilt component because $[\hat{n}_1 \times \hat{n}_2] = 0$. As discussed in section 1.6.1, this apparent discrepancy originates from the fact that the symmetry relation, $\hat{n}_2 = \pm\hat{n}_1$ (eq. (1.25b)) does not cover all sets of crystallographically equivalent lattice planes (see eq. (1.30)). To formally assign a tilt component to a symmetrical interface, at least one non-collinear combination of $\hat{n}_1$ and $\hat{n}_2$ has to be found which characterizes the same set of crystallographically equivalent planes.

To illustrate the formal assignment of a tilt component to an STGB, we mention the well-known fact that in a cubic crystal an arbitrary combination of Miller indices $(\pm h, \pm k, \pm l)$, can always be converted, by a sequence of 90° rotations about ⟨100⟩ which transforms the crystal into itself, for

Grain b

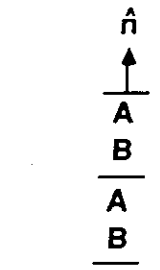

Ideal crystal

(a)

Fig. 1.39 The
or bcc lattice
illustrates tha
configuration
(a).

<111>

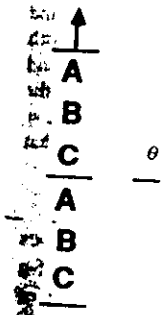

θ

Ideal crystal

(a)

Fig. 1.40 Genera
lattice as a 60° twi
interface-plane no
terized by either
and (b)). Its CSL-
boundary would
boundary it would

example into a
k, l). Starting,
perform a 90°
y → z, z → −x
rotation about x
y → z) finally y

Finally, in the tilt-inclination scheme the boundary is characterized by (eq. (1.54))

$$\{\text{DOFs}\} = \{(1\bar{1}0),\ 50.58^{\circ},\ \alpha = 0^{\circ},\ \theta = 0^{\circ}\} \quad (\Sigma = 11) \tag{1.67}$$

Again, as in the CSL scheme, the GB is readily identified as a pure tilt GB (from the fact that $\theta = 0^{\circ}$), and its symmetry follows directly from the fact that $\alpha = 0^{\circ}$. However, starting from these parameters, the identification of the crystallographic orientation of the GB plane is non-trivial.

We conclude this section by emphasizing an aspect of the conceptualization of symmetrical-tilt boundaries as special twist boundaries; this is of particular relevance to the computer simulation of GBs. In all GB simulations, in addition to the bicrystal at hand, a suitable undefected reference system containing the same number of atoms has to be considered in order to determine any excess quantity associated with the interface (such as the interface energy, thermal expansion, etc.). STGBs are conventionally generated by rotating two infinite, interpenetrating lattices with respect to one another, with the subsequent removal of corresponding atoms on both sides of the GB plane. This procedure gives rise to ambiguities regarding the undefected reference system with the same density and crystallographic orientation of the simulation cell as the bicrystal, rendering the determination of any excess quantities ambiguous.

1.8.4 Atomic-level geometry of symmetrical-tilt boundaries

From a strictly geometrical viewpoint, symmetrical-tilt boundaries are fascinating, yet little understood, objects. Since, like free surfaces and stacking faults, these simplest of all GBs have only two macroscopic DOFs (section 1.6.3), in this section we will discuss their atomic-level geometry in more detail.

As illustrated in Fig. 1.36(b), the atomic structure of an STBG is characterized by the familiar inversion of the stacking of the lattice planes at the interface ('twinning'), a feature in common to all STGBs. However, the directly inverted configuration in Fig. 1.36(b) is usually unstable because two identical lattice planes are right on top of one other. We refer to this translational state, in which the GB-plane is a mirror plane but not an atom plane, as the **unstable** twin. Two energetically more favorable translational states are shown in Fig. 1.38. In the **special twin** in Fig. 1.38(b), the GB is both a mirror plane and an atom plane. In the fcc lattice, for example, there is only one special-twin configuration, namely the STGB on the (111) plane. With the . . . |ABC| . . . stacking of (111) planes (with a three-plane stacking sequence, $P(111) = 3$, section 1.7.1 and Table 1.1), the directly inverted, unstable-twin configuration would be characterized by . . . |ABC|CBA| . . . , while in the optimal translational state the C plane is shared by the two halves, according to . . . |ABC|AB C BA|CBA| . . . .

On some arbitrary higher-index lattice plane, no physical reasons exist to favor the particular, high-symmetry special-twin configuration in Fig. 1.38(b). The STGB on such a plane usually exhibits some rather arbitrary rigid-body translation which is not generally a multiple of the in-plane stacking vector $\boldsymbol{e}$ in Fig. 1.28. We refer to such a translational state, sketched in Fig. 1.38(c), as a **general** twin, emphasizing the fact that its planar structure is still characterized by the inversion at the GB ('twin'), but that no special rigid-body translation exists.

Figure 1.39 illustrates that at least *three* planes are required in the repeat stacking sequence in the direction of $\hat{n}$, $P(\hat{n})$, for that plane to accommodate an STGB configuration. Consider, for example, the generation of an STGB on a set of lattice planes with only two planes in the repeat stacking sequences, such as the (100) and (110) planes in the fcc and bcc lattices. Starting with the perfect-crystal stacking . . . |AB|AB| . . . in Fig. 1.39(a), a 180° twist rotation yields the inverted configuration . . . |AB|BA| . . . (Fig. 1.39(b)). For reasons given above, this configuration of the STGB in which two planes are right on top of one another is usually unstable (Fig. 1.38(a)), giving rise to a rigid-body translation, $\boldsymbol{T} = (T_x, T_y)$, parallel to the interface. The obvious translation to minimize the mismatch across the interface is one in which B returns to A; such a translation, however, leads to

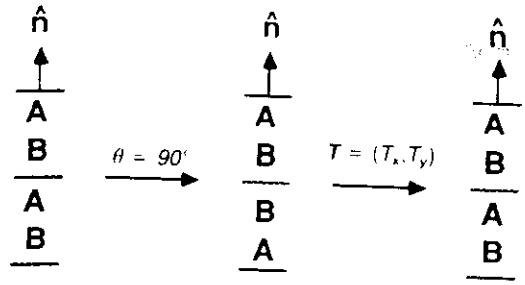

Fig. 1.39 The creation of an STGB on the (100) plane in the fcc or bcc lattice by a 90° twist rotation (for $m = 2$; section 1.7.2) illustrates that, upon suitable translation in (c), the STGB configuration in (b) becomes identical to the perfect crystal in (a).

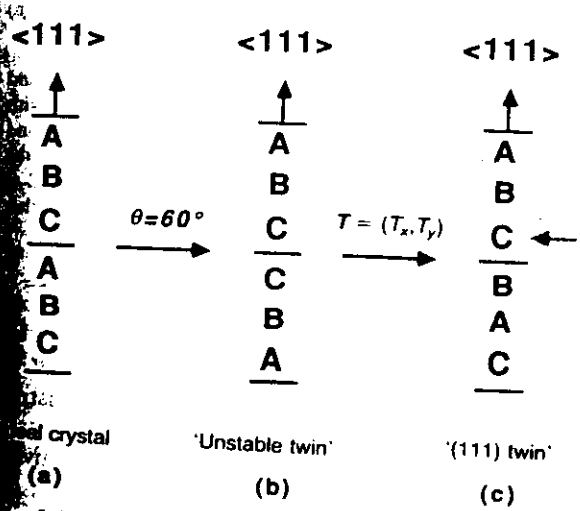

Fig. 1.40 Generation of the (111) twin boundary in the fcc lattice as a 60° twist boundary (with $m = 3$; section 1.7.2). In the interface-plane nomenclature, this STGB would thus be characterized by either (111) (111) 60° or (111) (11$\bar{1}$) 0° (eqs. (1.60a) and (b)). Its CSL-based characterization (eq. (1.64)) as a twist boundary would be (111) 60° (111); by contrast, as a tilt boundary it would be defined by ⟨110⟩ 70.53° (111) ($\Sigma = 3$).

example into a form $(h, k, \pm l)$, $(h, \pm k, l)$, or $(\pm h, k, l)$. Starting, for example, with $(-k, l, h)$, one can perform a 90° rotation about the y-axis (such that $x \to z$, $z \to -x$, $x \to z$) to obtain $(h, l, -k)$; next, a rotation about x by −90° (such that $x \to x$, $z \to -y$, $y \to z$) finally yields the (h, k, l) configuration.

Let us now consider the case in which $\hat{n}_2 = -\hat{n}_1$, i.e. in Miller indices the interface is characterized by (eq. (1.60b))

$$\{\text{DOFs}\} = \{(h, k, l), (-h, -k, -l), \theta = 0°\} \tag{1.68}$$

Applying the cubic symmetry operations illustrated above, this expression may be rewritten, for example, as follows (Fig. 1.41):

$$\{\text{DOFs}\} = \{(h, k, l), (h, k, -l), \theta = 0°\} \tag{1.69}$$

where, in order to be specific, the z-direction was chosen as the symmetry direction. (Had we chosen, for example, the y-axis as the symmetry direction, $(h, k, -l)$ would be simply replaced by $(h, -k, l)$.) As illustrated in Fig. 1.41, the condition, $\hat{n}_2 = -\hat{n}_1$ may thus be equally written as $(\hat{n}_2)_z = -(\hat{n}_1)_z$.

To summarize, a non-collinear set of planes which is crystallographically equivalent to the collinear set for $\hat{n}_2 = -\hat{n}_1$ is given, for example, by the condition that $(\hat{n}_2)_z = -(\hat{n}_1)_z$. These expressions for $\hat{n}_1$ and $\hat{n}_2$ may be inserted into eqs. (1.21) and (1.22) to determine the tilt component of the interface, according to [21]

$$\hat{n}_T = (h^2 + k^2)^{-\frac{1}{2}} \begin{pmatrix} -k \\ h \\ 0 \end{pmatrix} \tag{1.70}$$

$$\sin \psi = 2 * l(h^2 + k^2)^{\frac{1}{2}}/(h^2 + k^2 + l^2) \tag{1.71}$$

i.e. the tilt axis and -angle are fully determined by the Miller indices associated with the STGB plane.

Given that an STGB has only *two* DOFs, but that $\hat{n}_T$ and Ψ represent three geometrical parameters, it is not surprising that the tilt axis and angle obtained from eqs. (1.70) and (1.71) are not unique, and other $(\hat{n}_T, \psi)$ combinations may be given for the same STGB on the (h, k, l) plane. The number of combinations is finite, however, because the number of crystallographically equivalent non-collinear combinations of Miller indices is finite. As an example, we consider the STGB on the (3, 4, 1) plane which, according to eqs. (1.70) and (1.71), may be considered as having been generated by a rotation about the ⟨−4, 3, 0⟩ axis by $\psi = 22.62°$. However, in deriving eqs. (1.70) and (1.71), we could have chosen, for

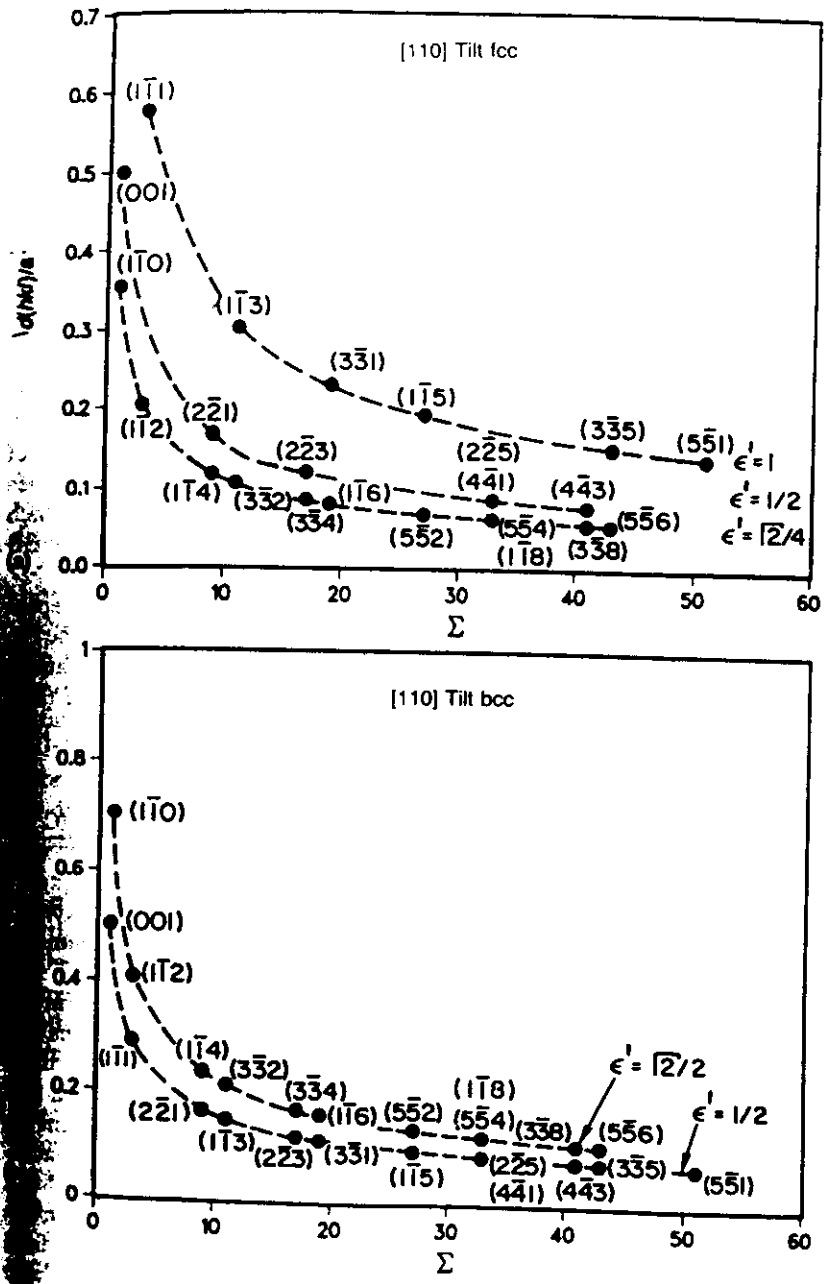

Fig. 1.43 Relationship according to eq. (1.74) between $\Sigma = \Sigma(hkl)$ and $d(hkl)$ for STGBs with a common ⟨110⟩ tilt axis in (a) the fcc and (b) the bcc lattice [20]. The figure demonstrates that a low value of Σ is necessary, but not sufficient, for a large value of $d(hkl)$. The value of $\varepsilon' = \varepsilon'(hkl)$ defined in eq. (1.74) also has to assume one of its largest values for $d(hkl)$ to be large.

$$\Sigma = \beta'\varepsilon^2 a^2 [d(hkl)]^{-2}, \quad (\beta', \varepsilon = 1 \text{ or } 0.5)$$
$$= \beta'' a^2 [d(hkl)]^{-2}, \quad (\beta'' = 1, 0.5, 0.25 \text{ or } 0.125) \qquad (1.73)$$

This relationship between $d(hkl)$ and the value of Σ of the STGB on that plane is illustrated in Figs. 1.43(a) and (b) for STGBs in the fcc and bcc lattices, respectively. Instead of plotting Σ as a function of $d(h, k, l)$, however, the figure shows the inverse relation (eq. (1.73))

$$d(h, k, l) = (\beta'')^{-\frac{1}{2}} a\Sigma^{-\frac{1}{2}} = \varepsilon' a\Sigma^{-\frac{1}{2}},$$
$$(\varepsilon' = 1, \sqrt{2}/2, 0.5, \text{or } \sqrt{2}/4) \quad (1.74)$$

Finally, for a Bravais lattice with a basis of one atom (with atomic volume Ω), the planar unit-cell area of the STGB and perfect-crystal configurations on the (h, k, l) plane is given by (eqs. (1.41) and (1.43))

$$A(h, k, l) = \Omega/d(h, k, l)$$
$$= (\Omega/a)\varepsilon^{-1}(h^2 + k^2 + l^2)^{-\frac{1}{2}},$$
$$(\varepsilon = 0.5 \text{ or } 1) \quad (1.75)$$

For example, with $\Omega = a^3/4$ and $\Omega = a^3/2$ for the fcc and bcc lattices, respectively, the areal units Ω/a in eq. (1.75) are given by $a^2/4$ and $a^2/2$, respectively. Equation (1.75) is readily extended to twist angles other than $\theta = 0°$ and 180°. Starting from the planar density of CSL sites for a given twist angle, $\Gamma(\theta)$, eq. (1.62) yields

$$A(\theta, h, k, l) = \Gamma(\theta) A(h, k, l)$$
$$= \Gamma(\theta)(\Omega/a)\varepsilon^{-1}(h^2 + k^2 + l^2)^{-\frac{1}{2}},$$
$$(\varepsilon = 0.5 \text{ or } 1) \quad (1.76)$$

We conclude by summarizing the following properties of symmetrical grain boundaries in cubic crystals.

1. Without loss of generality, *all* symmetrical boundaries in cubic Bravais lattices may be characterized as follows:

$$\text{DOFs} = \left\{ \hat{n}_1 = (h^2 + k^2 + l^2)^{-\frac{1}{2}} \begin{pmatrix} h \\ k \\ l \end{pmatrix}, \right.$$
$$\left. n_2 = (h^2 + k^2 + l^2)^{-\frac{1}{2}} \begin{pmatrix} h \\ k \\ \pm l \end{pmatrix}, \theta \right\} \quad (1.77)$$

   Here the + sign defines the set of symmetrical-twist boundaries in which the symmetrical-tilt boundaries are included for $\theta = 180°$. The − sign is useful only if one wishes to formally assign a tilt component to the interfaces.
2. In the related three-parameter phase space, the STGBs are geometrically unique in that (a) they represent a special subset of twist boundaries, and (b) they represent the GBs with the smallest planar unit-cell dimensions (identical to those of the perfect crystal). This unique geometry of the pure tilt configuration on a given plane gives rise to a deep energy cusp at $\theta = 180°$, and hence to 'special' properties of STBGs [33]. Most twist boundaries may therefore be viewed as 'vicinal' to either the STGB configuration on a given plane or to the perfect crystal.
3. Similar to free surfaces, the geometry of the tilt boundaries may be expressed entirely in terms of the two DOFs associated with the Miller indices of the GB plane. The three geometrical parameters in the tilt axis and angle are therefore not unique.
4. The value of Σ, the inverse volume density of CSL sites, is governed by the number of planes in the repeat stacking sequence, $P(hkl)$, which in turn is given by the Miller indices of the GB plane.
5. At least three planes are required in the repeat stacking sequence, $P(hkl)$, for a plane to accommodate a non-trivial STGB configuration. The 'STGB' on a set of lattice planes with $P(hkl) = 2$ or 1 is identical to the ideal crystal.

1.9 CHARACTERIZATION OF THE ATOMIC STRUCTURE OF INTERFACES

Throughout this chapter we have been concerned with the (macroscopic and atomic-level) **geometry** of solid interfaces, which we distinguish fundamentally from their **atomic structure**. The investigation of 'structure'–property correlations for interface materials usually involves both of these aspects of the interface structure, geometrical and physical, although the ultimate goal remains to correlate physical properties with the five macroscopic DOFs. To illustrate this distinction between the (crystallography-based) geometry and (physics-based) atomic structure of interfaces, in this final section we briefly review a few concepts that have evolved for the characterization of the atomic structure of solid interfaces.

The usefulness of any model for the atomic structure of solid interfaces should be assessed in terms of its ability to predict physical properties

of the interface, in addition to providing a good description of its crystallography and/or atomic structure. The dislocation model of Read and Shockley [40], which predicts the structure, energy, mobility, and other properties of low-angle GBs in terms of a quantitative characterization of the atomic structure (via Frank's formula (1.61), is an excellent example for such a model.

The most pronounced structural feature of solid interfaces is the atomic-level disorder near the interface. This type of disorder is well characterized in terms of the radial distribution function, $G(r)$, or its Fourier transform, $S(k)$. As is well known, thermal disorder in an otherwise perfect crystal gives rise to two effects in $G(r)$: First, the δ-function-like zero-temperature peaks associated with the shells of nearest, second-nearest and more distant neighbors are broadened; second, because of the volume expansion, the peak centers are shifted towards larger distances.

Owing to the presence of planar defects, interface materials are structurally disordered even at zero temperature. However, because of its localization near the interface, this type of disorder is **inhomogeneous** – in contrast with thermal disorder [42]. To illustrate this inhomogeneity in the direction of the interface normal, it is useful to consider the radial distribution function for each of the atom planes near the interface (or, conversely, the planar structure factor). As seen from Fig. 1.44 for the case of a symmetrical (100) twist boundary in the fcc lattice, the amount of structural disorder decreases very rapidly from one (100) plane to another, indicating the existence of large gradients in many properties. Interestingly, the **structural** disorder at the interface gives rise to the same two effects even at zero temperature, as does **thermal** disorder in an otherwise perfect crystal, namely, a broadening of the peaks combined with a shift towards larger distances [42]. This shift, originating from the volume expansion near the interface, is seen from the shift of the arrows in Figs. 1.44(a)–(c), with the open arrows marking the average peak position in the bicrystal while the solid ones mark the corresponding perfect-crystal peaks.

The type of detailed atomic-level information contained in Fig. 1.44 is difficult to obtain experimentally. Various models have therefore been proposed to describe the atomic structure at the interface without having to know the atom positions too precisely. In one such group of models, summarily known as **polyhedral-** or **structural-unit** models and primarily applied to GBs [41, 43–46], the atomic structure is described in terms of the stacking of polyhedra along the interface (Fig. 1.45; [47]). The requirements of space filling at the interface, and of the compatibility of the structural units with the adjoining grains, generally cannot be satisfied simultaneously, however, unless the polyhedra are elastically distorted. Hence, while the idea to describe the structure of GBs in terms of a few basic polyhedra is interesting, the systematic distortions of the polyhedra from one GB to another make it difficult to quantify the structure.

In a second group of models, known as **hard-sphere** models, the optimum translation parallel to the interface plane is assumed to be the one which minimizes the volume expansion at the GB [41, 48–50]. Although based on **unrelaxed** atomic structures, via the volume expansion these models provide at least a rough quantitative measure of the degree of structural disorder at the interface.

As discussed in detail elsewhere [29], both groups of models may be combined via the characterization of the atomic-level disorder in terms of the number of broken nearest, second-nearest and higher-order neighboring bonds. Such a quantified formulation of these models makes them now available for a systematic investigation of atomic-level structure–property correlations [29]. While such broken-bond models have been very successful for over 50 years in predicting physical properties of free surfaces from their relaxed or unrelaxed atomic structure [28], their application to solid interfaces is not yet very widespread.

In a broken-bond model the atomic structure is characterized quantitatively, for example, via the number of broken ν-th nearest-neighbor (nn) bonds per unit interface area, given by [29]

$$C(\nu) = \Sigma_n |K_{id}(\nu) - K_n(\nu)|/A \qquad (1.78)$$

where A is the planar unit-cell area. $K_n(\nu)$ denotes the number of ν-th nearest neighbors of atom n, while $K_{id}(\nu)$ is the related perfect-crystal value.

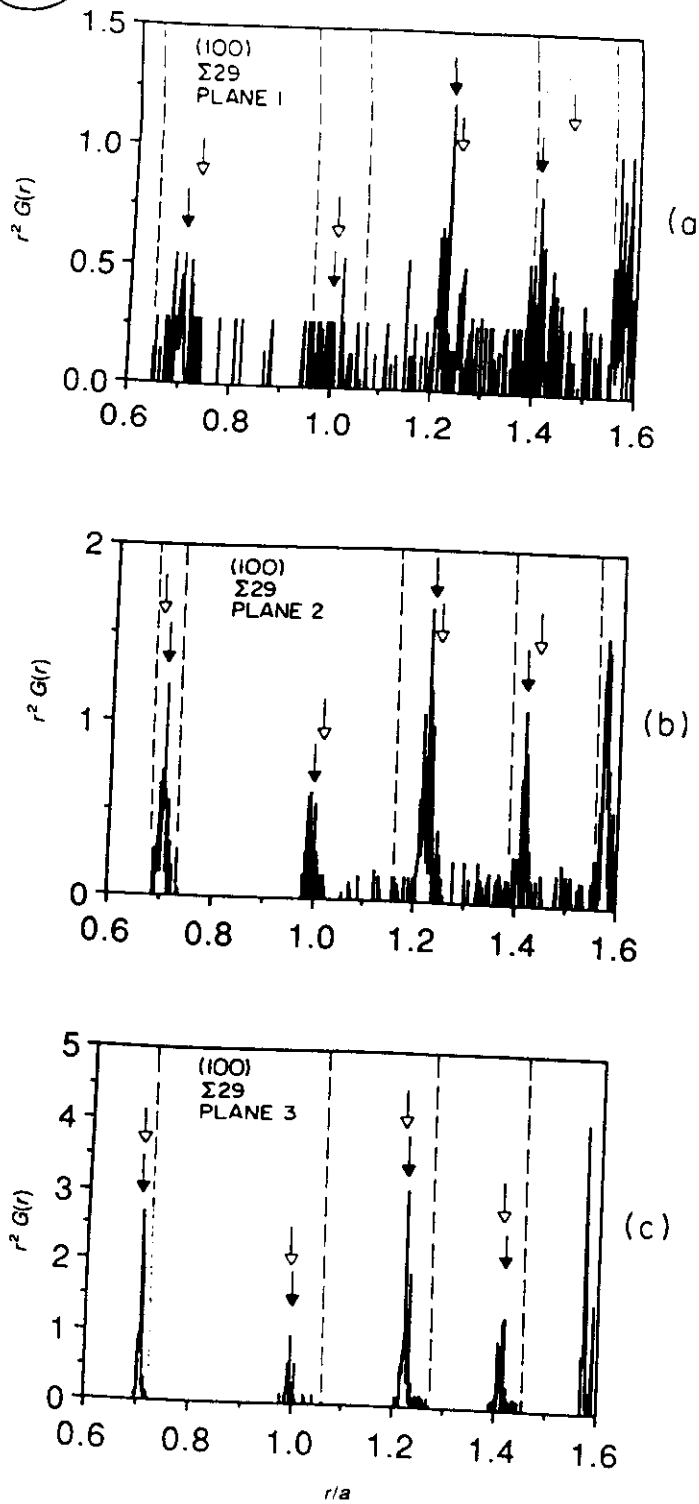

Fig. 1.44 Radial distribution function, $r^2G(r)$, for the three lattice planes nearest to the symmetrical (100) $\theta = 43.60°$ ($\Sigma = 29$) twist boundary in the fcc lattice. Solid arrows indicate the corresponding perfect-crystal peak positions; open arrows show the average value of r in a given atomic shell. The widths of these shells are indicated by dashed lines [51].

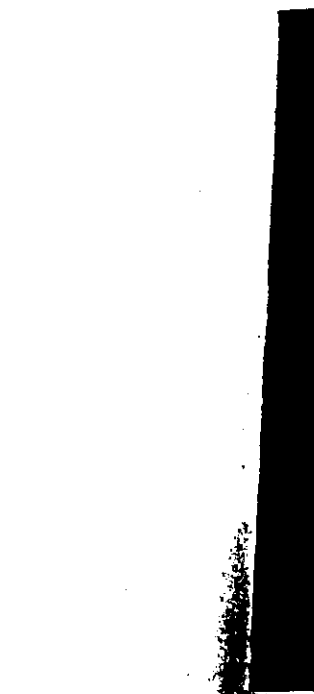

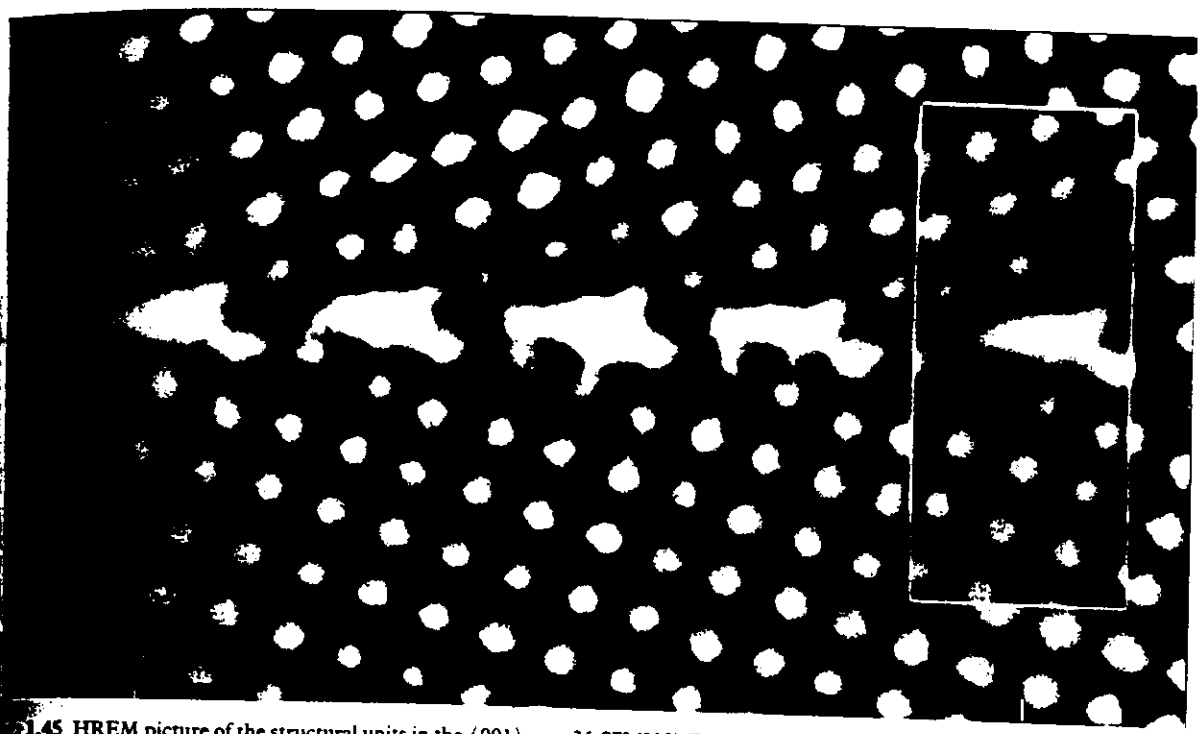

1.45 HREM picture of the structural units in the ⟨001⟩ $\psi = 36.87°$ (310) ($\Sigma = 5$) STGB in NiO [47]. (In the interface-plane ...e, this GB would be referred to as the STGB on the (310) plane, (310) (3$\bar{1}$0) 0°; eq. (1.60)b.) The inset shows the image averaged ...many structural units [47]. (Courtesy of K. L. Merkle).

...ewhat arbitrarily, the nearest neighbors are ...ned to include all those atoms situated between ... distance and the half-way point, $R_{12} = (R_1^{id} +$ ...)/2, between the nearest and 2nd-nearest neigh- ... in the perfect crystal. $C(\nu = 1)$ is thus closely ...nected with the area under the nn peak in the ...al distribution function. The 'miscoordination ...efficient' $C(1)$ thus provides a convenient quan- ...tive measure of how well the atoms are, on ...rage, coordinated in the fully relaxed structure. ...(1) is usually given in units of a^2 [29].

This definition of broken nn bonds corresponds ... the replacement of the overall plane-by-plane ...dial distribution functions near the GB, for ...mple, in Figs. 1.44(a)–(c) by the integral under ... nearest-neighbor peak in $G(r)$, with a sub- ...quent summation over all the lattice planes near ... interface. Because all the information contained ... the detailed shape of the nn peak is thus lost, ...tic strain-field effects associated with inter- ...ce dislocations or surface steps are therefore not included in $C(1)$, as is also the case for the polyhedral-unit and hard-sphere models. While in the case of the free surfaces this may not be a very severe limitation, in low-angle GBs the strain-fields associated with interface dislocations may dominate the behavior near the interface, thus severely limiting the use of these models. (For further details see [27] and [29].)

ACKNOWLEDGMENTS

I have benefited from many stimulating discussions with J. A. Jaszczak, K. L. Merkle, S. R. Phillpot, C. L. Wiley and S. Yip. I am particularly grateful to K. L. Merkle for making available copies of Figs. 1.7, 1.34 and 1.45, and to C. B. Carter for kindly providing Fig. 1.8. This work was supported by the US Department of Energy, BES Materials Sciences, under Contract No. W-31-109-Eng-38.

REFERENCES

1. See also D. Wolf and S. Yip, Interfaces. *MRS Bulletin*, XV(9) (Sept. 1990), 21.
2. D. N. Seidman, *Experimental Investigation of Solid Interfaces*, Chapter 2 in this volume.
3. W. Bailey, V. A. Frank-Kamenetskii, S. Goldsztaub, A. Kato, A. Pabst, H. Schulz, H. F. W. Taylor, M. Fleischer, and A. J. C. Wilson, *Acta Cryst.* **A33** (1977), 681.
4. See, for example, R. J. Needs, *Phys. Rev. Lett.*, **58** (1987) 53, and references therein.
5. See, for example, D. Wolf, *Surf. Sci.*, **225** (1990) 117, and references therein.
6. A. I. Jankowski and T. Tsakalakos, *J. Phys.*, **F15** (1985), 1279.
7. D. Wolf and J. F. Lutsko, *Phys. Rev. Lett.*, **60** (1988), 1170.
8. D. Wolf, *Appl. Phys. Lett.*, **58** (1991), 2081.
9. See also D. Wolf and J. Jaszczak, *Computer Simulation of the Elastic Behavior of Thin Films and Superlattices*, Chapter 14 in this volume, and references therein.
10. J. W. Christian, *Transformations in Metals and Alloys – Part I. Equilibrium and General Kinetic Theory*, Pergamon Press, Oxford (1975).
11. Y. Gao, K. L. Merkle, H. L. M. Chang, T. J. Zhang, and D. J. Lam, *Mat. Res. Soc. Symp. Proc.*, **221** (1991), 59, and *Phil. Mag. A*, (1992), in press.
12. C. B. Carter and H. Schmalzried, *Phil. Mag.* **A52** (1985), 207; C. B. Carter, E. G. Colgan, S. McKernan, Y. K. Simpson, S. R. Summerfelt, D. W. Susnitzky, and L. A. Tietz, *J. Phys. Colloque* **C5**(49) (1988), C5–239.
13. W. A. Jesser and J. H. van der Merwe, in *Dislocations in Solids*, Vol. 8 (ed F. R. N. Nabarro), North-Holland (1989), p. 421.
14. J. H. van der Merwe and W. A. Jesser, *J. Appl. Phys.*, **63** (1988) 1509; W. A. Jesser and J. H. van der Merwe, ibid., p. 1928.
15. G. B. Olson and Morris Cohen, *Acta Metall.*, **27** (1979) 1907.
16. D. G. Brandon, B. Ralph, S. Ranganathan, and M. S. Wald, *Acta Metall.*, **12** (1964), 813.
17. B. Chalmers and H. Gleiter, *Phil. Mag.*, **23** (1971), 1541.
18. See, for example, C. Goux, *Can. Metal. Quarterly*, **13** (1974), 9.
19. W. Bollmann, *Crystal Defects and Crystalline Interfaces*, Springer-Verlag, New York (1970).
20. D. Wolf, *J. Phys. Colloque*, **C4**(46) (1984), C4–197.
21. D. Wolf and J. F. Lutsko, *Z. Kristallographie*, **189** (1989), 239.
22. See, for example, B. D. Cullity, *Elements of X-Ray Diffraction*, Addison-Wesley, Reading, MA (1967).
23. See, for example, W. D. Kingery, H. K. Bowen, and D. R. Uhlmann, *Introduction to Ceramics*, 2nd edn, Wiley, New York (1976), p. 107.
24. See, for example, H. B. Aaron and G. F. Bolling, in *Grain Boundary Structure and Properties* (eds G. A. Chadwick and D. A. Smith), Academic Press, New York (1976), p. 107.
25. D. A. Smith, C. M. F. Rae and C. R. M. Grovenor, in *Grain-Boundary Structure and Kinetics*, ASM, Metals Park (1980), p. 337.
26. G. H. Bishop, R. J. Harrison, T. Kwok and S. Yip, *J. Appl. Phys.*, **53** (1982), 5596.
27. D. Wolf and J. Jaszczak, *Role of Interfacial Dislocations and Surface Steps in the Work of Adhesion*, Chapter 26 in this volume.
28. See, for example, C. Herring, in *Structure and Properties of Solid Surfaces* (eds R. Gomer and C. S. Smith), University of Chicago Press (1953), p. 4, and references therein.
29. D. Wolf, *J. Appl. Phys.*, **68** (1990), 3221.
30. See, for example, P. G. Shewman and W. M. Robertson, in *Structure and Properties of Solid Surfaces* (eds R. Gomer and C. S. Smith), University of Chicago Press (1953), p. 67.
31. D. Wolf, *Surf. Sci.*, **226** (1990), 389.
32. D. Wolf and K. L. Merkle, *Correlation between the Structure and Energy of Grain Boundaries in Metals*, Chapter 3 in this volume.
33. D. Wolf, *J. Mater. Res.*, **5** (1990), 1708.
34. See, for example, V. Randle, B. Ralph, and D. Dingley, *Acta Metall.*, **36** (1988), 2753; V. Randle and D. Dingley, *Scripta Metall.*, **23** (1989), 1565.
35. H. Ichinose and Y. Ishida, *J. Physique Colloque*, **C4**(46) (1985), C4–39.
36. K. L. Merkle, Proc. 46th Ann. Meeting of the Electron Microscopy Soc. of America, (1988), p. 588; *MRS Symp. Proc.*, **153**(83) (1989); *Colloque de Phys.*, **51** (1990), C1–251.
37. K. L. Merkle and D. Wolf, *Phil. Mag. A*, **65** (1992), 513.
38. K. L. Merkle and D. J. Smith, *Phys. Rev. Lett.*, **39** (1987), 2887, and *Ultramicroscopy*, **22** (1987), 57.
39. C. B. Carter, *Acta Metall.*, **36** (1988), 2753.
40. W. T. Read and W. Shockley, *Phys. Rev.*, **78** (1950), 275; see also W. T. Read and W. Shockley in *Imperfections in Nearly Perfect Crystals* (eds W. Shockley, J. H. Hollomon, R. Maurer and F. Seitz), Wiley, New York (1952), p. 352.
41. See, for example, H. J. Frost, M. F. Ashby and F. Spaepen, *A Catalogue of [100], [110], and [111] Symmetric Tilt Boundaries in Face-Centered Cubic Hard-Sphere Crystals*, Harvard University Press (1982).
42. S. R. Phillpot, D. Wolf and S. Yip, *MRS Bulletin*, **XV** 10 (Oct. 1990), 38.
43. M. Weins, B. Chalmers, H. Gleiter, and M. F. Ashby, *Scripta Metall.*, **3** (1969), 601.

44. M. Weins, H. Gleiter, and B. Chalmers, *Scripta Metall.*, **4** (1970), 732, and *J. Appl. Phys.*, **42** (1971), 2639.
45. D. A. Smith, V. Vitek, and R. C. Pond, *Acta Metall.*, **25** (1977), 475 and ibid., **27** (1978), 235.
46. H. Gleiter, in *Atomistics of Fracture* (eds R. M. Latanision and J. R. Pickens), Plenum, New York (1983), p. 433.
47. K. L. Merkle, J. F. Reddy, C. L. Wiley and D. J. Smith, *J. Phys. Colloque*, **C5**(49) (1988), C5–251.
48. M. F. Ashby, F. Spaepen and S. Williams, *Acta Metall.*, **26** (1978), 1647.
49. H. J. Frost, M. F. Ashby and F. Spaepen, *Scripta Metall.*, **14** (1980), 1051.
50. M. Koiwa, H. Seyazaki and T. Ogura, *Acta Metall.*, **32** (1984), 171.
51. D. Wolf and J. F. Lutsko, *Phys. Rev. Letters*, **60** (1988), 1170.